INVESTIGATION OF SATELLITE MEASUREMENTS IN THE PRESENCE

OF CLOUDS, FORCING INFLUENCES ON CLOUDS AND FEEDBACK TO

THE LARGE SCALE FOLLOWING CONVECTION.

FINAL TECHNICAL REPORT

Charles Warner

CHARLES WARNER, PRINCIPAL INVESTIGATOR

2/15/83 TO 8/14/84

DEPARTMENT OF ENVIRONMENTAL SCIENCES,
CLARK HALL,
UNIVERSITY OF VIRGINIA,
CHARLOTTESVILLE   VA 22903

SATELLITE OBSERVATIONS OF A MONSOON DEPRESSION

Charles Warner
Department of Environmental Sciences
Clark Hall
University of Virginia
Charlottesville, VA 22903

ABSTRACT

This study continues the exploration of a monsoon depression, observed during the Summer Monsoon Experiment of the Global Atmospheric Research Program. Building on published results obtained from research aircraft, satellite data are examined, with emphasis on the Microwave Sounding Unit (MSU) aboard TIROS-N, and the Scanning Multichannel Microwave Radiometer (SMMR) aboard Nimbus-7.

In agreement with the previous results, the structure of the monsoon depression was found to be dominated by cumulus convection. Generally, deep convection was organized along mesoscale lines. The satellite maps reflected this property, and did not show circular patterns as often obtained by analysis of streamlines. Events in the upper troposphere did not appear to play a dominant role in formation or maintenance of the storm. The only systematic large-scale behavior discerned was a propagation of the depression westward, and diurnal migration of contours of brightness temperature drawn from MSU. These contours in the middle troposphere showed a gradient toward the north, the patterns migrating northward at night.

In the satellite data, organized thermal structure in the depression was masked by effects due to hydrometeors. It was found principally from SMMR and dropwindsondes that water vapor contents were near 65 mm, increasing to more than 70 mm in the northeast Bay of Bengal. Cloud water contents reached about 3 mm. Rainfall rates exceeding 5.7 mm/h occurred over a few percent of the storm area (from SMMR and from airborne radar data). Mean rainfall rates in areas of order 20000 km^2 reached ~ 0.5 mm/h.

Measured MSU brightness temperatures could be reconciled very well with dropwindsonde data and with airborne in situ observations of clouds (by photography) and hydrometeors (by radar). In computations of brightness temperature, it was found important to allow for diffuse scattering from the sea surface of downwelling radiation, and to allow for both primary and secondary scattering by hydrometeors. It was found in this work that often, large amounts of low cloud were implied by the MSU measurements - up to ~ 30% area coverage at several millimeters of water. There was apparently an absence of large area coverage by radar bright band due to melting snow.

1. Introduction

This study continues the exploration of a monsoon depression begun by Warner (1984a) and Warner and Grumm (1984). Observed during the Summer Monsoon Experiment (SMONEX), this storm in the Bay of Bengal during July 1979 has been treated by Nitta and Masuda (1981) and Sanders (1984). The latter authors analyzed rawinsonde and dropwindsonde data, and obtained smoothly varying patterns easy to comprehend. The aircraft data indicated the prevalence of discontinuities at mesoscale lines of cumulus clouds, and it was inferred that all significant ascent in the lower troposphere in the depression occurred in cumulus clouds. The work by Warner and Grumm implies that one needs continuous coverage in the horizontal of a storm such as the SMONEX depression, in order to keep account of all the formations of cumulus clouds. Measurements such as those using rawinsondes, which do not always tell whether or not substantial ascent (in cumulus) is taking place in the vicinity, are inherently inadequate as a basis for monitoring such storms. Horizontal continuity of coverage is an inherent property of satellite radiometers. We therefore turn to satellite data to learn more about the monsoon depression.

Relevant to tropical storms, in what directions is satellite meteorology progressing? A few of the recent developments may be mentioned. For a hurricane or typhoon, key questions involve its future track, and whether or not it will intensify. The track appears to follow closely the deep layer mean wind (Velden and Smith, 1984). Wind fields are analyzed from cloud drift winds, gradient winds from VAS retrievals, water vapor motion winds at mid-levels, and TOVS microwave retrievals. VAS refers to the VISSR (Visible and Infrared Spin Scan Radiometer) Atmospheric Sounder, and TOVS is the TIROS Operational Vertical Sounder. Emphasis is placed on VAS because

the instrument is geostationary. TOVS covers a given area on only two passes per satellite per day. It is difficult to put a microwave instrument on a geostationary satellite because of the great antenna size required for acceptable resolution. Le Marshall et al. (1984) report improvements due to VAS. The value of the instrument would be enhanced were it possible to map surface pressure, to translate atmospheric thicknesses into heights (Pike, 1984).

We find short wave lengths being used to compile profiles of temperature and water vapor in hurricanes, because they can be monitored from geostationary orbit and thus used as often as every 20 min; this advantage is pursued despite the fact that mid-level fragmentary stratus (or some other cloud) generally prevails in a tropical storm (Warner and Grumm, 1984) so that views are generally not clear. Use of longer wavelengths avoids this problem.

Microwave studies have been made of tropical storms. Warm cores were found by Grody et al. (1979), Grody and Shen (1982) and Velden and Smith (1983). Assessments were made of storm intensity. The SMONEX depression was less intense than these systems, and the axis of circulation was tilted from the vertical, making the warm core more difficult to perceive when viewing from above. Some of the approaches used for the tropical storms could not be used for the SMONEX depression.

Two difficulties are found. If one uses short wavelengths there is no penetration of upwelling radiation from the low troposphere in the presence of dense precipitation or cloud. If one uses long wavelengths one has only two views per day (from a polar orbiting satellite), and horizontal resolution is relatively poor. For this study it has been found that the best data available were from GOES-1 with coverage in the visible every $\frac{1}{2}$ h during the day,

from the Microwave Sounding Unit (MSU) aboard TIROS-N, and from occasional passes by Nimbus-7. In this exploration, most of the results have come from MSU.

In Section 2 is provided a conventional depiction of the depression on 5 and 7 July, drawn chiefly from aircraft data (Warner, 1984a; Warner and Grumm, 1984). Maps derived from MSU are presented in Section 3.

Airborne dropwindsonde data are examined in Section 4, and related to measured MSU brightness temperatures, with some progress made in reconciling the two different sets of data.

At this stage it seemed appropriate to learn as much as possible from Nimbus-7 concerning the water vapor, cloud water and rainfall in the depression (Section 5). There follows in Section 6 a brief examination of infrared and water vapor channel imagery derived from Nimbus-7, which emphasizes the dominance of convection in the depression, and the presence of water vapor at high levels over it.

After finding that the imagery from MSU and Nimbus-7 is dominated by effects due to convection, a systematic study of the precipitation is begun with a statistical analysis of airborne radar data in Section 7. This is followed in Section 8 by a detailed study of behavior and structure on 5 July, yielding a description of a propagating line of intense convective cells.

In Section 9, it is found that anomalies of MSU brightness temperatures can be explained in terms of a variety of vertical distributions of hydrometeors. This long section contains much modeling. In Section 10, results across the microwave frequency spectrum of MSU are presented, to indicate potentialities of microwave sounders.

Returning to the observed maps from MSU in Section 11, diurnal variations are displayed.

3

Results are summarized in Section 12, and conclusions drawn in Section 13.

2. Conventional depiction of the depression: 5 and 7 July

Flow in the depression during the daytime of 5 July is shown in Fig. 1. The top panel shows streamlines and isotachs at 700 hPa; the bottom panel shows streamlines and one isotach at the surface over the Bay. The observations come from the WP-3D daytime flight, plus land data gathered at Calcutta airport during SMONEX; the patterns are drawn to be consistent with the atlas of Krishnamurti et al. (1980). Data over land were very sparse. A cyclone symbol in the top panel shows the center of circulation at 700 hPa. This position is tentatively drawn over the ridge line of the Arakan mountains of Burma: there were few data to the east. Previous analyses (Nitta and Masuda, 1981; Warner, 1984a; Sanders, 1984) have the depression already over the Bay on 5 July, moving slowly westward at 2.3 m/s (Nitta and Masuda). It appears now that it remained stationary and ill-defined until 5 July, and then traversed the Bay at about 3.5 m/s. The surface flow (Fig. 1, bottom) is obtained chiefly from dropwindsonde data extrapolated subjectively downward from the lowest level of measurement (~ 935 hPa). These measurements were augmented by the author's visual estimates of surface winds made from the WP-3D, by looking down at the sea surface. It is possible to state that winds were consistently strong in the southeast part of the Bay, and light and variable in the north. Strong surface flow was toward masses of cloud appearing bright in the DMSP satellite visible image, Fig. 2. Brightest cloud masses are sketched in Fig. 1 (bottom). The visible image does not suggest the presence of an axis of cyclonic circulation. Mountain features to the northeast are picked out in white, shown very probably by small cumulus and stratocumulus.

The circulation during the daytime of 7 July was defined by dropwind-sondes and flight level data from the Electra and WP-3D aircraft. Streamlines and isotachs at 700 hPa are shown in Fig. 3 (top). Clouds from the DMSP visible image are shown in Fig. 3 (bottom). The surface flow is omitted: only the center of circulation is shown by the cyclone symbol. The depression was fully developed on 7 July (Warner, 1984a; Warner and Grumm, 1984). It subsequently moved over India and dissipated.

3. A series of maps from the Microwave Sounding Unit

Twice-daily passes by the polar orbiter TIROS-N have been exploited to yield a series of maps of brightness temperatures measured using the Micro-wave Sounding Unit (MSU), which has four channels with frequencies in the 60 GHz band of absorption by oxygen. One may refer to Grody (1983) for a description of the characteristics of MSU. He shows the 11 scan spots ar-ranged across the track of the satellite. First it is necessary to find appro-priate limb corrections (ΔT_B) to brightness temperatures (T_B) measured in scan spots away from no. 6, at nadir. This was done graphically, by plot-ting T_B against scan line number for several passes on different orbits over the equatorial Indian Ocean, and joining up consecutive points of the same scan spot number; the line for spot 1 was superimposed over that for spot 6 and a limb correction for spot 1 was obtained visually. This subjective procedure was repeated for all the scan spots, and yielded the limb cor-rections shown in Figs. 4 and 5 as plotted dots and crosses. The dots refer to scan spots 1 to 5, to the left side of the sub-orbital track of TIROS-N. The crosses refer to scan spots 7 to 11, to the right. The results show asymmetry between left and right sides. They vary smoothly with $\sqrt{(\cos\theta)}$, where θ is the zenith angle of observation. Smooth lines were drawn by eye through the points shown in Figs. 4 and 5; these yielded the limb corrections

5

given in Table 1. The greatest variability occurred in Channel 1, and the same limb corrections were applied on both sides of the track. These limb corrections are compatible with findings by Grody (personal communication, 1983). The values in Table 1 were inserted into a computer program for reading and calibrating MSU radiances stored on magnetic tape, written following Lauritson et al. (1979, with amendments dated 19 October 1981).

Maps of brightness temperatures from MSU channels 1 to 3 are shown in time series in Figs. 6 to 9. Channel 4 (57.95 GHz) is not included. At this frequency absorption by oxygen is relatively strong; the brightness temperature weighting function (see Grody, 1983) peaks near 90 hPa; thermal structure at lower levels is not discernible. Channel 4 brightness temperatures remained near 206.5 K over the depression, with a weak increase with latitude.

The top panels of Figs. 6 to 9 show the locations of the scan spots as small circles. The areas increase with distance sideways from the suborbital track, as illustrated by Grody (1983) and documented in Table 1. This and the variation of viewing angle (θ) accounts for the need to consider limb corrections. The brightness temperatures were corrected to equivalent nadir values, using Table 1. At nadir, measurements in spot 6 required no correction.

MSU channel 3 (at 54.96 GHz) is sensitive to oxygen near the 300 hPa level. The brightness temperature patterns from MSU 3 are shown in the top panels of Figs. 6 to 9. They feature a weak south-north gradient. Systematic evolution of the patterns has not been identified. The most obvious regularity is a diurnal north-south migration, discussed in Section 11.

It has been suggested that development of a monsoon depression may be triggered by passage from the east over the northern Bay of a wave in the upper troposphere. MSU has footprints of area ~ 50000 km² (Table 1); this area seems very suitable in respect of horizontal averaging for the purpose of detection of variations of temperatures which might be associated with such an upper-level wave. The time series of MSU 3 maps for 300 hPa show no obvious suggestions of passage of a wave at the time of development of the depression, 3 to 6 July.

MSU 2 (at 53.73 GHz) is sensitive to air temperatures near 700 hPa; also ty hydrometeors at air pressures near or below 700 hPa. Isolated patches of low brightness temperatures seen in the middle panels of Figs. 6-9 can mean either low air temperatures near 700 hPa, or hydrometeors in the middle to upper troposphere, or both. As will be shown below, the most likely explanations of most of the cold patches involve precipitation. Around the centers of air circulation (see the cyclone symbols in later maps) no signs of a warm core are found. Grody and Shen (1982) displayed the warm core of Hurricane David (1979) using MSU. A warm core is not readily perceived in MSU brightness temperatures in this monsoon depression. Aircraft data (Warner, 1984a) showed that the depression did feature a warm column along the northeast side of the axis of circulation on 7 July. This axis was tilted at 1:30 upward toward 210°. A suggestion of its presence is discernible as south-westward protrusions in the contours of 230 K in MSU 3 and 261 K in MSU 2 in Fig. 9 (7 July), near 90°E, 21°N.

The patchiness of patterns from MSU 2 turns out to be due largely to the showery character of the storm.

MSU 1 (at 50.30 GHz) is sensitive to air temperatures near the surface, and to εT_s, the product of surface emissivity (ε) and temperature (T_s).

7

This quantity is large over land, and data from MSU 1 are presented only over the Bay of Bengal. Warm anomalies in MSU 1 occur if the atmosphere contains absorbing hydrometeors in the low troposphere. In Figs. 6 to 9 it may be seen that several matching patterns of anomaly occur in the maps from MSU 2 and MSU 1. The most likely explanations are in terms of hydrometeors. These are explored in Section 9. Further analysis follows in Section 11.

4.   Dropwindsonde data

From the Electra and WP-3D aircraft, many dropwindsondes were released from the middle troposphere. Those which were released at latitudes > 10°N, and which yielded good temperature and moisture data, are listed in Table 2. For each day they are listed in order of latitude (in column 1). Columns 1-4 indicate the position, time of release and aircraft (WP-3D, P; or Electra, E). The greatest pressure at which a measurement was recorded is shown in column 5. The surface wind speed (extrapolated subjectively downward) is given in column 6. The surface pressure (approximate) and temperature (by extrapolation) appear in columns 7 and 8. After sketching in upper tropospheric profiles according to Table 3, column 9 indicates the vapor in the atmospheric column. (Only 1.6 mm is contributed by the upper sketched part of the sounding.) Columns 10, 11 and 12 show measured and calculated MSU 1 brightness temperatures and their difference. Columns 13, 14 and 15 show the same parameters for MSU 2. Column 16 shows the air temperature at 700 hPa measured by the dropwindsonde.

The measured MSU temperatures were obtained from maps as in Figs. 6 to 9. The calculated brightness temperatures were obtained from a computer program of radiative transfer, initially provided by T. T. Wilheit of Goddard Space Flight Center (GSFC). This program was rewritten and refined in the

course of gaining familiarity with its' workings. The work of Wentz (1983) was used to treat radiation diffusely scattered by the sea surface. After assuming sea water salinity of 34 parts per thousand in the Bay, and that sea surface temperature equaled air temperature, the dielectric constant of the water was obtained from the work of Klein and Swift (1977). Then the specular emissivity (ε_o) at zenith was calculated (after Wentz). The emissivity ε was found from

$$\varepsilon = (1-f)\varepsilon_o + f \tag{1}$$

where the foam coverage (f) was proportional to surface wind speed w (m/s)

$$f = 0.006w - 0.042 \qquad (w > 7 \text{ m/s}) \tag{2}$$

This equation for f communicated by T. T. Wilheit is broadly compatible with Wentz's effective foam coverages (his Fig. 6).

Minor refinements after Liebe et al. (1977) of the treatment by Rosenkranz (1975) of absorption by oxygen were employed. The equations given by Waters (1976) were used for absorption by water vapor.

Measured and calculated brightness temperatures from Table 2 are plotted in Fig. 10. One point on each of the plots for MSU 2 and MSU 1 is separated from the others. It refers to the location 16.98°E, 92.24°N on 5 July. Reference to Figs. 1 and 2 shows that this location featured cloud. As will be described, there was also precipitation.

The points for MSU 2 are clustered near the 45° line of equality of measurement and calculation. This excellent agreement, generally within 1 K, was distinctly better than before inclusion of Wentz's treatment of diffuse scattering at the sea surface, when calculated brightness temperatures were ~ 0.7 K smaller.

Measured brightness temperatures in MSU 1 generally exceed calculated values, by ~ 4 K. This is expected, due to the presence of cloud and haze

at low levels. The more moist soundings (labeled M in Fig. 10 if the total water vapor ≥ 68 mm) show greater temperatures than the dry soundings. The comparisons in Fig. 10 serve to confirm the correctness of both measurements and calculations.

How do the brightness temperatures compare with air temperatures? At 300 hPa we do not have air temperature measurements to compare with MSU 3, but we do have air temperatures at 700 hPa (T_{700}, K) to compare with brightness temperatures (T_2, K) from MSU 2. These comparisons are plotted in Fig. 11. It is found that

$$T_2 \sim 0.49 \ T_{700} + 121 \tag{3}$$

There is considerable scatter among the points, due to variations for instance in surface conditions and water vapor.

5. SMMR maps of water vapor, cloud water and rainfall

Grody et al. (1980) describe a technique for estimating water vapor and cloud water in an atmospheric column from radiances measured aboard Nimbus-6 in and near the absorption band of water vapor, at 22.23 and 31.65 GHz respectively. This technique was employed on radiances with horizontal polarization at 18 and 21 GHz measured using the Scanning Multichannel Microwave Radiometer (SMMR) aboard Nimbus-7, and available on "CELL-ALL" magnetic tapes from GSFC (Madrid, 1978). For extraction of vapor and cloud contents, use of just the two SMMR channels at 18 and 21 GHz with horizontal polarization was considered satisfactory. A more elaborate multiple regression procedure (after Wilheit and Chang, 1980) is often favored. In this technique, radiances at 6.6 and 10.69 GHz are taken into consideration, to allow for variations of surface wind speed and surface temperature. Close to shore

as in this study, effects of antenna sidelobes can mar measurements at the lower frequencies.

After preliminary runs of the radiative transfer program previously described, adapted to SMMR and applied to the dropwindsondes, it was found that the "weighted mean atmospheric temperature" (Grody et al., 1980, p. 995) was close to 288 K at 18 GHz and 286 K at 21 GHz. Where T_{18H} and T_{21H} are the brightness temperatures calculated at 18 and 21 GHz with horizontal polarization, the quantities $\ln(288 - T_{18H})$ and $\ln(286 - T_{21H})$ were plotted against the water vapor W (mm), following Grody et al. The results are shown in Fig. 12. Grody et al. obtained obvious straight lines. In Fig. 12 the results are not so good; they are stratified by surface wind speed. Estimating a wind speed near 10 m/s in the areas viewed by Nimbus-7, straight lines were drawn by eye through the points in Fig. 12. These yielded the following equations

$$(W/953) + (Q/Q_{18}) \sim 1.623 - 0.318 \ln(288 - T_{18H}) \qquad (4)$$

$$(W/194.5) + (Q/Q_{21}) \sim 1.650 - 0.318 \ln(286 - T_{21H}) \qquad (5)$$

Here W (mm) is the water vapor in the column and Q (mm) the cloud water (zero in the calculations but not in the cases of measurement); T_{18H} and T_{21H} are the two measured brightness temperatures (K). The quantities Q_{18} and 953 mm are absorption parameters for cloud and vapor respectively at 18 GHz, and Q_{21} and 194.5 mm are the same parameters at 21 GHz. The constant terms refer to oxygen; the factor 0.318 is equal to $1/(2 \sec\theta)$, where the zenith angle (θ) of SMMR observation was 50.5°. The parameters Q_{18} and Q_{21} vary approximately as the square of the frequency:

$$(Q_{18}/Q_{21}) = (21/18)^2 = 1.36 \qquad (6)$$

Grody et al. give $Q_{22} = 9.78$ mm. Therefore

$$Q_{21} \sim 10.7 \text{ mm} \tag{7}$$

After measurements of T_{18H} and T_{21H}, Eqns. (4) to (7) may be solved for W and Q. The results of this process yielded negative anomalies of W in places rich in Q, dry air with the cloud. The same obviously incorrect tendency was manifest after plotting finished products tabulated on Nimbus 7 PARM-LO magnetic tapes from GSFC. It was decided to modify Eq. (6):

$$q = (Q_{18}/Q_{21}) = 1.36 - 0.0576 \ Q^2 \quad (Q \geq 0; \ 1.36 \geq q \geq 1) \tag{6a}$$

With increasing cloud water Q, it is here supposed that larger and larger drops are present, bringing the parameters Q_{18} and Q_{21} closer and closer together, to 1.0 if $Q \geq 2.5$ mm. For maps of W and Q shown below, the system (4), (5), (6a) and (7) was solved iteratively in the program for reading CELL-ALL data tapes, processing brightness temperatures given on grids of dimension 60 km.

For rainfall (R, mm/h), brightness temperatures measured at 37 GHz with horizontal polarization, (T_{37H}, K) were processed using an algorithm given in Lipes (1981)

$$R = 8.3 \times 10^{-7} \ \exp(0.065 \ T_{37H}) - 0.1$$

$$(T_{37H} > 180K; \ 0 \leq R \leq 18 \text{ mm/h}) \tag{8}$$

This curve flattens out at large values of T_{37H}; any estimates exceeding 18 mm/h would not be of quantitative value. The greatest rainfall from the 30 km grid values of T_{37H} encountered here was 13 mm/h.

Maps of water vapor W (mm), cloud water Q (mm) and rainfall rate R (mm/h) are shown in Figs. 13 to 15 at left, center and right, respectively, in each figure. Fig. 13 refers to 3 July, 0552 GMT; Fig. 14 refers to 7 July, 0523 and Fig. 15 to 7 July, 1813 GMT. The swaths covered by SMMR aboard Nimbus 7 near the equator were only about 7° of longitude wide, while adjacent orbits were 26° apart in longitude. Data from even dates in early July

1979 are not available. Data over land are excluded from this study. We have only occasiónal coverage of the depression by SMMR.

The left panels of Figs. 13 to 15 show magnitudes of water vapor increasing toward the northeast corner of the Bay, from values near 60 mm upwind to the southwest. The broad similarity of values shown in the maps to values from the dropwindsondes in Table 2 indicate compatibility between the brightness temperature data on the CELL-ALL tapes, the dropwindsonde data and the computer program of radiative transfer designed to discern the effects of vapor and droplets on the radiation. No major problems are apparent. The various data and calculations are consistent with one another.

The right panels of Figs. 13 to 15 show the showery character of the rainfall, with rates often reaching a few millimeters per hour.

Comparing right and left panels, minima of vapor are noted in places of great rainfall. This is an artifact, previously discussed. It would no doubt be possible to invent a version of Eq. (6a) which would smooth over the minima, but uncertainty would remain; it is preferred to leave the products as they are and to be cautious in interpretation.

The middle panels in Figs. 13 to 15 show the cloud water (Q, mm). Little new information is added here. Photographs over the Bay (Warner and Grumm, 1984; Warner, 1984b) show that cloud was usually present. Values near 3 (0.03 mm), or more, are expected all over the Bay. The analysis cannot yield results of such precision, because of effects of varying surface wind speed, and occasionally large hydrometeors. With the multichannel approach of Wilheit and Chang (1980), over the open ocean remote from land, this problem can be treated. The present maps of Q give only crude estimates, only where amounts were relatively large. The calculations show

maximum amounts near 2 mm. Using Eq. (6) instead of (6a) yielded maxima ~ 30% larger.

The magnitudes of water vapor in the left panels in Figs. 13 to 15 appear to be correct to ± ~ 5 mm. The center panels indicate cloud water amounts often reaching 1 mm. The rainfall rates (R) from T_{37H} often reach 5.7 mm/h; this is equivalent to a radar reflectivity (Z) of 35 dBZ, if

$$Z \sim 300 \ R^{1.35} \tag{9}$$

(Jorgensen and Willis, 1982). Small patches of this intensity are found. Similar small patches from the depression are shown in Fig. 2 of Warner (1984a), from airborne radar. Details are given in Table 4 of the area of the SMMR swath covered by rainfall of various rates. These percentages of area coverage are similar to values from airborne radar presented in the next section. They match well the results of Ruprecht and Gray (1976, Fig. 7) for a typical Western Pacific cloud cluster.

If $186.2 \leq T_{37H} \leq 194.1$ K, the rainfall is calculated from Eq. (8) as 0.1 mm/h. It seems that the areas of such rain shown in the northern Bay in Figs. 13 to 15 may be too extensive, because photographs do not generally show showers in contiguous 30 km by 30 km bins.

6. THIR imagery

Photographic images were obtained from the Temperature Humidity Infrared Radiometer (THIR) aboard Nimbus-7 (Hwang, 1982). In Figs. 16-20 referring to the period 4-6 July as indicated, an image recorded in the infrared window at 10.5-12.5 μm is shown at left. This yields temperatures of cloud tops where present, or of land or ocean surfaces, with resolution 6.7 km at nadir. An image recorded in the water vapor channel at 6.5-7 μm is

14

shown at right. This shows the moisture and cirrus cloud content at high·
levels, with resolution 20 km at nadir.

On 4 July at 0613 GMT (Fig. 16) cloudiness of the depression is evident
at 90°E, 20°N. At 90°E, 28°N, note the front range of the Himalayas in the
11.5 μm image; note its non-appearance at 6.7 μm. At 6.7 μm, note the
discontinuity oriented NE-SW, with moist air to the SE. This remarkable
feature corresponds with the flow at 200 hPa shown in the atlas by
Krishnamurti et al. (1980). It does not correspond with patterns at lower
levels. Evidently we see in the 6.7 μm channel only the upper-level mois-
ture.

On 4 July at 1719 GMT (Fig. 17) one may note convection at 90°E well
north of 20°, and convection over the Himalayas. Evident linear discontinu-
ities have not been related to any other meteorological elements or topog-
raphy; probably they relate to mesoscale patterns of flow at upper levels.

On 5 July at 0447 GMT (Fig. 18) the 6.7 μm channel (right) clearly
shows discontinuities in moisture trending NE-SW. At lower left, the de-
pression is seen as a series of line features of convection; there is an ab-
sence of circular symmetry. A circular area of cloud predominated near
110°E, 20°N - the Gulf of Tonkin area.

On 5 July at 1737 GMT (Fig. 19) the valleys of the Ya'lung, Mekong and
Salween Rivers near 99°E 28°N are visible at 11.5 μm. Trending north-south,
these features separate India and China. Cloudiness over them was absent as
the depression lay further west. Cloud covered southern China.

On 6 July at 0506 GMT (Fig. 20) further clearing is apparent over the
mountains north of India. The system from southern China had moved west-
ward. The moisture pattern seen at 6.7 μm (right) showed NE-SW trends as
before.

This sequence of IR window and water vapor images implies the following. The depression showed no circular structure in cloudiness or water vapor to match the circles one gets from streamline analysis of occasional wind data, as presented by Sanders (1984).

The convective cloudiness over the Bay in the depression was composed of features aligned east-west; it showed no mesoscale continuity over a half day.

Abrupt discontinuities were recorded at 6.7 μm, trending NE-SW. These were related to features at upper levels. Continuity with systems in the mid-latitude westerlies can be traced by referring to the atlas by Krishnamurti et al. (1980).

7. Statistics from airborne radar data

The WP-3D aircraft carried a lower fuselage radar of wavelength 5.6 cm, horizontal beamwidth 1.1° and vertical beamwidth 4.1° (Houze et al., 1981a; Jorgensen, 1984; Marks, 1984). Composite maps from this radar have been presented by Warner (1984a), for 7 July at three levels in the depression. Area coverages by radar echoes were presented by Warner (1984a, Table 1); these followed manual analyses of color slides received from D. D. Churchill at the University of Washington, which were enlarged by projection. D. D. Churchill has since provided digital radar maps, which have made possible more accurate compilations of area coverages. For observations on 5 and 7 July, these are presented in Table 5, in order of ambient pressure at flight level. Attention is concentrated here on 5 July because the WP-3D passed close to intense convection on this day, and comparisons between different sets of data may be made.

The data in Table 5 for 7 July are in broad agreement with those in Table 1 of Warner (1984a), but more details are given for high reflectivities.

These data are from composites from numerous radar scans over intervals of time; the data for 5 July are from individual scans. Marks (1984) has discussed differences between composites and individual scans: the composites show the maximum reflectivity seen in any one geographical location, which generally is found when the aircraft is closest to that point; an individual scan can yield underestimates at great range from the aircraft. It seems that on 5 July at 0425:38 GMT, for instance, the area coverage 2.7% for reflectivities of 27 ± 2 dBZ may be an underestimate. Assignment of height or pressure to the area coverages in Table 5 is very uncertain, because of the great vertical beamwidth of the radar, 4.1°. It seems that substantial contributions to the measured reflectivities at 483 hPa on 5 July probably came from melting hydrometeors at 550-600 hPa, at about 1200 m below flight level.

The radar echo coverages in Table 5 may be compared with the area coverage by rain estimated using SMMR in Table 4. Only the lowest two levels in Table 5 appear to be appropriate for comparison; at 483 hPa on 5 July area coverage was a maximum in the interval of reflectivity centered at 32 dBZ. At the lowest levels and in the SMMR data, area coverage increased at lower reflectivities/rainfall rates. The composite radar maps at 694 and 945 hPa on 7 July indicated rather more rain at low rates (with averages of 17.3 and 19.4%) than SMMR (1.2 to 7.6%). In general, agreement between the data in Tables 4 and 5 appears to be as good as can be expected.

The reasons for generally greater coverage at great reflectivity on 5 July as compared with 7 July are not known. Differences in measurement are possible. On 5 July, intense convection was organized along an east-west line, whereas cells were fewer and further apart on 7 July. For comparison

17

with the satellite measurements, data for 5 July will now be examined in detail.

8.   Radar maps and photographs on 5 July

The radar map for 0357 GMT on 5 July is shown in Fig. 21. At the time the position of the aircraft (marked by a cross) was near the southern limit of a large area of echoes. To the south lay a line of intense echoes. To the east, echoes came from land. In particular, Cheduba Island is readily recognizable.

As the aircraft turned on to a southward heading within the echo shown in Fig. 21, turbulent convective draft cores were encountered. Details are given in Table 6 (after Warner and McNamara, 1984). They occurred only in the southeast part of the echo area. The shape of the overall echo, and these measurements, imply ascent on the southeast (leading) edge, with a plume extending northwestward.

As the aircraft emerged from cloud, I took a 35-mm color slide of the clouds looking upward above flight level, at location A in Fig. 21. This photograph is shown in Fig. 22. The tuft of high cloud was several kilometers above flight level. An ice haze was present near the aircraft.

Passing near the cloud line, a panorama of two color slides was taken at location B in Fig. 21. This view (Fig. 23) shows new cumulus towers building above flight level on the east end of the line of radar echoes.

Following 29 min after that in Fig. 21, the map of reflectivities made at 0426 GMT is shown in Fig. 23. From the original of this map, a large area of reflectivities around 35 dBZ, west of the aircraft and having a symmetrical crescent-shaped pattern, has been omitted; it is attributed to sea clutter, due to ocean waves facing the radar.

Marked along the track of the aircraft in Fig. 23, the location B of the photograph Fig. 22 is seen to have been surrounded by echo at 0426 GMT, 16 min later. Eastward propagation of the echoes is discerned.

Just before reaching the line of echoes, a dropwindsonde was released at the location marked D/S in Fig. 24. A tephigram from this is shown in Fig. 25. The stratification was of density nearly neutral to moist adiabat ascent, as in the sounding shown in Fig. 14 of Warner (1984a), except for a dry stable layer at 70 kPa. Cold air near the surface may have been due to downdraft outflow from a convective cell.

Looking east-northeastward from location C, that of the aircraft at the time of the radar scan presented in Fig. 24, the photograph shown in Fig. 26 was taken. This shows slender cumulus humilis and mediocris clouds arranged in bands along direction 145°. These bands are not aligned at a small angle to the winds like "cloud streets" in conditions of subsidence, as described for instance in Warner (1982). These bands are arranged across the flow. From Fig. 1, the flow at the surface and at 700 hPa is found, and plotted in the hodograph Fig. 27. The band orientation estimated from the photograph, 145°, matches the shear between the flows at the surface and 700 hPa. The cloud bands are arranged across the flow. Their "castellanus" appearance (Scorer and Wexler, 1963; Warner and Grumm, 1984, p. 160) implies unstable stratification. Their disposition as bands of ascent out of the surface layers implies convergence. The strong surface flow depicted in Fig. 1 toward the mountainous Burmese coast implies convergence. The line of radar echoes in Fig. 24 of orientation similar to the cloud bands implies low level convergence.

Further from the Burmese coast by 250 km, the WP-3D again crossed the line of convection on return northbound late on 5 July. A strong updraft

core reaching 15.7 m/s was encountered (see Table 6). The corresponding radar map is shown in Fig. 28. It appears that just high convective cores were recorded. Reflectivities (Z) of ~ 32 dBZ correspond to ice contents (I) of 0.7 g/m³ (Table 5, if

$$I(g/m^3) \sim 0.008 \ (Z, \ mm^6 m^3)^{0.605} \qquad , \qquad (10)$$

after Herzegh and Hobbs, 1980). This value seems high; Churchill and Houze (1984) indicate values nearer 0.2 g/m³ (23 dBZ). The echoes in Fig. 28 may have come partly from large hail particles, or partly from melting hydrometeors at altitudes 4 km below flight level.

Taken approaching the line from the south, at location D marked in Fig. 28, the photograph in Fig. 29 shows slender cumulus indicating unstable stratification south of the line. An overcast is based just above flight level at 329 hPa. Similar features are seen in the view westward from location E, shown in Fig. 30.

As the aircraft passed through the line, strong updraft cores document- ed in Table 6 were recorded. Their locations are marked in Fig. 28.

A schematic representation of the echo line position at 1001 GMT (Fig. 28) is superimposed on Fig. 24. Over an interval of 5.6 h the line position moved 188 km south - a propagation velocity of 9.3 m/s southward. There was no wind velocity like this in the area. The line persisted by regeneration in the unstable lower troposphere on its south side. Propagation apparently of similar nature on 7 July was described by Warner and Grumm (1984).

North of the line the stratification was stable in the lower troposphere, with stratus layers (Warner 1984b, Fig. 6). The difference in soundings south and north of the line is emphasized in the two tephigrams shown in

Fig. 31. South of the line (solid lines in Fig. 31) the stratification was unstable, with subsidence in the upper troposphere shown by low humidity above an inversion. North of the line, the sounding shown as dashed lines in Fig. 31 indicates dry layers and stable layers near the surface, and much moisture aloft.

On 5 July the Electra aircraft flew a track to the west of that of the WP-3D. Its side cameras were used for cloud photogrammetry (Warner, 1981). A height-time section of cloud measurements from the left side camera as the aircraft flew southward is shown in Fig. 32. The active part of the cloud line is indicated by the presence of strong cumulus draft cores encountered around 0600 GMT (see Table 6). To the south, cumulus of great number density were found in stratification generally unstable, with haze (as in Warner 1984b, Fig. 5), here reaching 600 hPa. Fragmentary stratocumulus was found at 700 hPa; it sloped downward toward the south, for reasons unknown. Aloft, cirrus was measured at altitudes as great as 15 km. Dense high overcast was measured at altitudes ≤ 12 km. North of the region of intense rising motion, the sky was clear aloft (see 0530 GMT in Fig. 32, corresponding to latitude 20°N); stratus layers were found at levels near and below flight level. Often the air was clear near the surface.

The data presented in this section have shown how on 5 July cloud lines propagated southward into a region of unstable stratification leaving a stable area with many fragmentary layers of stratus to the north. Comparison of the radar maps Figs. 22 and 24 with the MSU portrayal in Fig. 8 (left) shows how MSU was affected by the deep convection. The area of low temperatures in MSU 2 at 0849 GMT on 5 July was along latitude 17°N. From the radar maps Figs. 24 and 28, it is seen that the cloud line propagated through this latitude at this time.

9. Exploration of possible causes of MSU brightness temperature variations

In the maps of MSU brightness temperatures in Figs. 6-9, anomalously great temperatures (T_1) in MSU 1, and low temperatures (T_2) in MSU 2, have already been noted. For three of the maps from 4 and 5 July, these are highlighted along curved lines around the Bay in Figs. 33-35. The lines start at points A in the western part of the Bay, proceed to a northernmost point N, and curve southeastward to points B. These lines are superimposed in the relevant panels in Figs. 7 and 8. Following Hubert et al. (1981), can we explain the various combinations of T_1 and T_2 that were measured using TIROS-N? Values of T_1 and T_2 calculated from dropwindsondes assuming an absence of hydrometeors have already been presented. Several of these apply to the case of 5 July, 0849 GMT, treated in Fig. 34. In this figure, calculated values of T_1 and T_2 have been plotted as crosses at points along the line ANB close to the locations of dropwindsonde release. Guided by these values, dashed lines have been drawn in Figs. 33-35 to approximate the values of T_1 and T_2 that would have been recorded had there been no hydro-meteors. Enhancement of T_1 due to haze and small clouds near the surface is generally to be expected; occasional reduction in T_2 due to hydrometeors is expected; the dashed lines in Figs. 33-35 are drawn with these expectations in mind. There result various combinations of effects ΔT_1 and ΔT_2 which were probably due to hydrometeors. These anomalies are highlighted by shading. By use of a computer program of radiative transfer which includes treatment of hydrometeors, is it possible to reproduce the various combina-tions of ΔT_1 and ΔT_2 suggested in Figs. 33-35?

It is supposed that the field of view of a radiometer contains various fractions σ_i of area coverage by vertical distributions (i) of hydrometeors,

which individually yield brightness temperature anomalies ΔT_i. The overall anomaly is taken as

$$\Delta T = \sum_i \sigma_i \Delta T_i \quad (\sum_i \sigma_i = 1) \tag{11}$$

A typical moist sounding (5 July, 0416:36 GMT, see Table 2) was used as the basic sounding upon which various vertical distributions (i) of hydrometeors were superimposed, as described below. A summary of these distributions is given in Table 7.

9.1 Haze and shallow cumulus

From 1000 to 840 hPa, small droplets of cloud water were assumed, in amounts equal to 0.004 of the water vapor density (type 1a in Table 7). The absorption (γcloud) due to these droplets was calculated using Eq. (15) of Chang and Wilheit (1979)

$$\gamma\text{cloud (km}^{-1}) = 0.1886 \, M \, \nu\varepsilon''/[(\varepsilon' + 2)^2 + \varepsilon''^2] \tag{12}$$

where M (g/m³) is the cloud water content, ν(GHz) is the frequency, and (ε' - jε'') is the permittivity (calculated from results given by Ray, 1972). Scattering due to the droplets was assumed to be negligible. The amount of liquid water (Q) in the column was 0.12 mm, leading to ΔT_1 = 3.6 K and ΔT_2 = 0.1 K. A variant on this is type 1b included in Table 7, which yielded similar effects.

9.2 Updraft in a cumulus cloud

To simulate the large quantities of small droplets in a cumulus updraft, a one-dimensional cumulus model like that of Simpson and Wiggert (1971) has been run. Based on these studies, it seems that cloud water (M) in a cumulus updraft may be modeled as follows:

$$M = 0.5M_{max} \{1 + \cos\pi [p - 1000 + a(1000 - p_{top})]$$

$$/[p_{top} - 1000 + a(1000 - p_{top})]\} \qquad (13)$$

Here M follows a sine curve which tails off at pressure p_{top}, after reaching M_{max} at a fraction a of the pressure interval between 1000 hPa and p_{top}. The upper limit p_{top} was taken as 476 hPa, a was taken as 0.4 and M_{max} was taken as 2 g/m³. The absorption γ_{cloud} was calculated using Eq. (12), but was set to zero at temperatures < -5°C: the cloud was assumed to be frozen at lower temperatures with negligible absorption. Again scattering was assumed to be negligible. This model (type 2a) yielded Q = 6.77 mm, ΔT_1 = 45.6 K and ΔT_2 = -1.7 K. Variants on this theme are set out in Table 7. It is found that $\Delta T_1 \sim 44$ K is a "saturation" value at large Q; ΔT_1 only starts coming down as Q is reduced below 3 mm.

9.3   Light rain

Raindrops cause appreciable scattering of microwaves. In this case we modify the usual equation of radiative transfer. Instead of writing

$$dT_B/dx = - \gamma_a(T_B - T_o) \qquad (14)$$

as in Chang and Wilheit [1979, Eq. (1)], where T_B is brightness temperature, T_o is the temperature of the medium, γ_a is the absorption coefficient and x is distance along the path of propagation, we write

$$dT_B/dx = - \gamma_e T_B + \gamma_a T_o \qquad (15)$$

where extinction (subscript e) is due to the sum of absorption (subscript a) and scattering. Integrating this over a slab of thickness x

$$T_{B_{out}} = T_{B_{in}} e^{-\gamma_e x} + (1 - e^{-\gamma_e x})T_o \, \gamma a/\gamma e \qquad (16)$$

where $T_{B_{in}}$ is the incident and $T_{B_{out}}$ the emerging brightness temperature.

24

This is identical to Eq. (2) of Chang and Wilheit (1979), except that the factor $\gamma a/\gamma e$ is associated with the temperature of the medium. This factor is equal to one minus the single scattering albedo, and Eq. (15) is called the single scattering approximation. Inclusion of effects of scattering both into and out of the beam (Weinman and Davis, 1978), rather than just out of it (as here), indicates that the single scattering approximation overestimates the effects of scattering. To compensate for this, the single scattering albedo (SSA) was replaced by SSA(2/3): the ratio $\gamma a/\gamma e$ was replaced by $(2(\gamma a/\gamma e) + 1)/3$. This step is arbitrary, but seems no less good than having to estimate an asymmetry factor, as do Weinman and Davis (1978); there are uncertainties in the various spectra of constitution, size and radiative properties of hydrometeors which make precision impossible at present. (Results obtained with the unmodified single scattering approximation are given in parentheses in Table 7.)

When applying Eq. (15) in the present calculations, γe is taken as the sum of components due to absorption of oxygen, water vapor and cloud droplets, plus extinction (called attenuation) due to larger hydrometeors; γa is the same, except that the attenuation due to the larger hydrometeors is multiplied by that value of the ratio ($\gamma a/\gamma e$) which applies to the hydrometeors under consideration. To model the effects of rain, attenuation coefficients are needed, and values of $\gamma a/\gamma e$ for rain.

To model a column of light rain, rates (R, mm/h) as follows were assumed

$$R = 1.23 \ (p - 610)/(990-610) + 0.27 \qquad\qquad (17)$$

for pressures $p \geq 610$ hPa. At lower pressures R = 0. This is a rain column of radar reflectivity 27 dBZ at 990 hPa decreasing to 17 dBZ at 610 hPa (compare Table 5). Water contents (M, g/m^3) are assumed to be given by

$$M(g/m^3) = 0.060 \ (R, \ mm/h)^{1.03} \qquad\qquad (18)$$

after Austin and Geotis (1979). Attenuation (γe, Nepers/km) is modeled after Olsen et al. (1978)

$$\gamma e = A \ R^b \qquad\qquad (19)$$

where A and b are as given in Table 8. The ratio

$$\gamma a/\gamma e \sim 0.64 - 0.12 \ \log_{10} \ [R(mm/h)], \qquad\qquad (20)$$

following the results for 60 GHz given in Table 1 of Ishimaru and Cheung (1980).

This model yielded Q = 0.22 mm, ΔT_1 = 9.5 K and ΔT_2 = -5.3 K. (With the unmodified single scattering approximation, ΔT_1 = -2.0 K and ΔT_2 = -8.1 K.) As may be seen from Table 7, scattering is an important feature of large hydrometeors, and results are sensitive to its treatment.

9.4 Heavy rain

To model a column of heavy rain, rates (R, mm/h) as follows were assumed

$$R = 1.9 \ (p - 610)/(990 - 610) + 1.5 \qquad\qquad (21)$$

for pressures p ≥ 610 hPa. At lower pressures R = 0. This is a rain column of radar reflectivity 32 dBZ at 990 hPa decreasing to 27 dBZ at 610 hPa (compare Table 5). With a treatment like the above, Q = 0.64 mm, ΔT_1 = 0.9 K and ΔT_2 = -13.1 K. (Note in Table 7 the sensitivity of ΔT_1 to the handling of scattering.)

9.5 Ice anvil cloud

To model an ice anvil, ice contents (I, g/m³) as follows were assumed

$$I = 0.067 \ (p - 410)/(530-410) + 0.05 \qquad\qquad (22)$$

for $530 \geq p \geq 410$ hPa, with $I = 0$ elsewhere. Reflectivities decrease upward with height from roughly 20 dBZ at the anvil base at 530 hPa (temperature $-0.2°C$).

Attenuation was modeled by the equation

$$\gamma e = CI \tag{23}$$

where C is given in Table 8. Ratios $\gamma a / \gamma e$ applying to ice are given in Table 8. These results were derived as follows. The ice particles were treated as spheres of diameter D. Then their extinction and absorption cross-sections are given by Battan et al. (1970), in terms of optical perimeter. One assumes that the number density of ice particles varies with D^{-3} (Bennetts and Ouldridge, 1984). In this case it is assured that the number density of particles, and the attenuation γe at any frequency, are proportional to the ice content I (g/m³). The constants of proportionality depend on the range of D assumed to be present. Here it was assumed that $0.05 \leq D \leq 1.0$ mm, yielding a number density of 380 particles per liter for every gram/m³ of ice; summations over this range of particle diameters led to the values of C and $\gamma a / \gamma e$ given in Table 8. The procedure is crude because ice particles have complex structures. This model (5a) yielded Q = 0.19 mm, $\Delta T_1 = -0.5$ K and $\Delta T_2 = -0.6$ K.

An ice anvil slightly different from the above was also constructed. John Gamache at the Center for the Environment and Man has supplied (April 1984) ice particle data gathered using the WP-3D aircraft during SMONEX (on 17, 23 and 25 June and 5, 7 and 8 July 1979). His overall particle size distribution is shown in Fig. 36. Assigning all particles to the equivalent spherical diameter at the center of the respective size class, integrations were performed from the smallest class upward in succession. Taking the particle

density as 0.1 g/cm³, the accumulating water content (I, g/m³) was calculated. The particles were then reduced in diameter by 0.464: these were spheres of the same mass but density 1 g/cm³. Their extinction and absorption cross-sections were calculated using the work of Battan et al. (1970) as before. Summing over the particles in each size class yielded contributions to γe and γa. Accumulating totals of I, γe and γa were compiled. After each step $\gamma e/I$ and $\gamma a/\gamma e$ were calculated. The purpose was to find representative values of $\gamma e/I$ and $\gamma a/\gamma e$ for each microwave channel.

Results of this exercise are shown in Table 9. (For general knowledge, SMMR channels are included, though not used here.) It was hoped that $\gamma e/I$ and $\gamma a/\gamma e$ would be nearly constant. This is true for the low frequencies of SMMR (bottom of Table 9). For MSU it is not a very good approximation, but will be pursued anyway. How do the previous results match these? From Table 8, values are added on the right in Table 9. General agreement is good. Plotting results on graph paper (not shown) yielded the following general equations for all four MSU frequencies (ν, GHz):

$$\gamma e/I(km^{-1}/(g\ m^{-3})) \sim exp\ (0.0712\ \nu - 7.094) \qquad (24)$$

$$\gamma a/\gamma e \sim 0.4515 - 0.0058\ \nu \qquad (25)$$

These equations yielded the adopted values appearing finally on the right in Table 9. They correspond to largest particles near diameter 2.5 mm (or 1 mm in the previous model). The model may not be very good; but the major weakness in this effort probably lies not here, but in treating the ice particles as spheres.

The ice anvil was assigned the distribution

$$I = 0.1\ (p - 330)/(470 - 330) + 0.05 \qquad (26)$$

for $470 \geq p \geq 330$ hPa, with $I = 0$ elsewhere, a distribution very similar to Eq. (22) but at a slightly higher level and yielding Q = 0.30 mm rather than

Q = 0.19 mm. This alternative anvil (type 5b in Table 7) yielded ΔT_1 = -0.8 K and ΔT_2 = -1.1 K.

9.6 Ice anvil cloud plus shallow cumulus

Combination of the ice anvil (type 5a) with the shallow cumulus (type 1a) yielded Q = 0.31 mm, ΔT_1 = 3.1 K and ΔT_2 = -0.5 K.

9.7 Ice anvil plus low cloud

It seemed desirable to attempt to simulate the cloudiness shown in Figs. 26, 29 and 30 above, involving a dense overcast over much cloud in the lower troposphere, composed of cumulus updrafts and their remnants. It was assumed that all the low cloud was of negligible scattering cross-section, and fitted a sinusoidal profile as described in Section 9.2, with p_{top} = 400 hPa, a = 0.3 and M_{max} = 0.25 g/m³. This yielded Q = 1.01 mm, ΔT_1 = 25.1 K and ΔT_2 = -0.2 K, and is type 2d in Table 7.

Combining the ice anvil type 5b with type 2d yielded Q = 1.31 mm, ΔT_1 = 15.9 K and ΔT_2 = -4.7 K.

9.8 Ice anvil plus bright band plus light rain

To the combination of the ice anvil (type 5a) with light rain (type 3), a bright band of melting snow was added. The bright band was modeled as rain of R = 1.5 mm/h in the interval 590 ≥ p ≥ 550 hPa (3.9°C ≥ temperature ≥ 0.7°C). The attenuation was taken from Eq. (19), but the ratio $\gamma a/\gamma e$ was taken as being that for ice from Table 8. This model means that for MSU 2 for instance, the bright band yields extinction like that of light rain (of R = 1.5 mm/h and Z = 27 dBZ from Table 5), while radar reflectivities are probably nearer 32 dBZ (see the measurements in Table 5). Scattering seems likely to be relatively important, so it was assumed that $\gamma a/\gamma e$ = 0.15 rather

than 0.62 from Eq. (20). As in the case of the ice anvil, this treatment of melting hydrometeors is a crude first attempt.

This model yielded $Q = 0.49$ mm, $\Delta T_1 = -4.9$ K and $\Delta T_2 = -15.6$ K.

9.9 Comparison of measurements (Figs. 33-35) with calculations (Sections 9.1-9.8)

Measured anomalies of brightness temperature due to hydrometeors have been identified in Figs. 33-35, and effects of hydrometeors have been calculated in Sections 9.1-9.8 and presented in Table 7. These are compared in Fig. 37, where crosses represent measured anomalies and dots refer to calculations. The crosses represent values of ΔT on the left hand side of Eq. (11)

$$\Delta T = \sum_i \sigma_i \, \Delta T_i \quad (\sum \sigma_i = 1), \tag{11}$$

while the dots refer to values ΔT_i on the right hand side and carry a label i for reference to Table 7. Explanation of the cross points A to G is sought in terms of combinations of dots, by invoking various combinations σ_i, and/or altering quantities Q_i in Table 7 to yield variations of ΔT_i. From study of the SMMR data in Section 5, it is expected that

$$Q = \sum_i \sigma_i \, Q_i \leq 3 \text{ mm} \tag{27}$$

From Fig. 37 it is immediately clear that the measurements A to G require substantial amounts $\sigma_i Q_i$ of the types $i = 2$ or $i = 1$ of hydrometeors. These types involve cloud droplets in tall cumulus updrafts (or their strati-form remnants), and cloud droplets in shallow cumulus respectively. It is expected that σ_2 is not likely to be more than a few percent (Warner and Grumm, 1984); it seems that Q_2 is likely to be relatively large. The content Q_1 is likely to be small, and σ_1 large.

Type $i = 6$ (shallow cumulus plus an ice anvil) has the same ratio $\Delta T_1/\Delta T_2$ as many of the measurements. Most of ΔT_1 due to type $i = 6$ comes from the shallow cumulus. The ice anvil alone ($i=5$) has only a small effect.

To produce negative values of ΔT_2, it seems that types $i = 3, 4, 7$ or 8 are to be invoked, involving respectively light rain, heavy rain, an ice anvil plus low cloud or the combination of an ice anvil, a bright band and light rain. It is noteworthy that the bracketed points for $i = 3, 4$ and 8 involve large negative values of ΔT_1 and probably are inappropriate: the single scattering approximation appears to be very crude. It does seem to be appropriate to modify the single scattering albedo (SSA) to (SSA)2/3, to get the points without parentheses. Light rain ($i=3$) then yields a ratio $\Delta T_1/\Delta T_2$ relatively close to the observed values.

With these considerations in mind, one may try to explain each of the points A to G by specific choices of parameters in Eq. (11), and evaluate Q from (27). Some results of these trials are presented in Table 10. Preliminary choices of representatives values of $\Delta T_1/Q$ and $\Delta T_2/Q$ for each type (i) were made, using the results in Table 7.

For large values of ΔT_1 and $-\Delta T_2$ as at points A and B, it is found that a great quantity of hydrometeors yielding large values of $\Delta T_{1i}/Q_i$, but small values $\Delta T_{2i}/Q_i$, must be invoked. This means type $i = 2$; type $i = 1$ is likely, but amounts Q_1 are relatively small. The large values ΔT_1 require the presence of several millimeters of hydrometeors in the atmospheric column, small enough not to scatter the radiation significantly. The large values of σ_2 needed in Table 10 testify to the importance of the inert cloud in the low troposphere documented by Warner and Grumm (1984; p. 157, Fig. 6 and Fig. A1). The photographs in Figs. 26, 29 and 30 show such cloud. The values σ_2 are larger than the few percent expected for cumulus updrafts, so

probably the real atmosphere contained a cloud type of properties intermediate between types i=1 and 2.

In respect of observation points A and B, it is known that type 6, ice anvil plus shallow cumulus, is appropriate from the photographs previously introduced. The large amounts σ_6 in Table 10 have been inserted to match this evidence.

With large amounts σ_6, it is found that there cannot be very large amounts of other types of hydrometeors which enhance $-\Delta T_2$. If much rain (i = 4) is invoked, $-\Delta T_2$ becomes too great and it becomes impossible to explain a large ΔT_1. A similar conclusion applies to the bright band (i = 8). It is found that rain over the Bay probably corresponded best with type i = 3, among the distributions here considered. In Table 10 quite large liquid water contents (Q_3) of precipitation are invoked, which yield a ratio $\Delta T_1/\Delta T_2$ near -2. It is clear from Fig. 37 that only small quantities of types which yield small ratios $\Delta T_1/\Delta T_2$ can be expected.

Where $\Delta T_2 = 0$, as at points F and G, types 1 and 2 are necessary. (Of course, the upper dashed lines in Figs. 33-35 may not be drawn perfectly correctly, so ΔT_2 may not quite be zero at these points.)

How do the results arrived at in Table 10, applying to the sections in Figs. 33-35 (taken from the maps of MSU brightness temperatures in Figs. 7 and 8), compare with mapped results from SMMR? The MSU results indicate that if MSU 1 indicates positive anomalies while MSU 2 shows weak or negligible anomalies, then there are a few tenths to 1.5 mm of hydrometeors in the low troposphere. For times other than those of the MSU data, the SMMR maps of cloud water (Figs. 13b, 14b and 15b) show like features. The MSU study shows that great anomalies ΔT_1 and $-\Delta T_2$ involve hydrometeors in the upper troposphere, and rain. Type i = 3 with $Q_3 = 0.22$ mm involves rainfall

at 1.5 mm/h at the surface. In Table 10 values of $Q_3 > 1$ mm are invoked, indicating rainfall at considerably greater rates. Peak rainfall rates from SMMR often exceeded 5.7 mm/h (Figs. 13c, 14c and 15c). The size of typical rain patches from SMMR is consistent with the size of typical patches of low brightness temperature T_2 from MSU. The results from the two satellite instruments are consistent with one another.

Regarding the columns on the right in Table 10, peak values of Q reach about 3 mm, as in Eq. (27). Anomalies ΔT_3 reach -0.6 K; magnitudes not quite as great as this were expected, but it seems that any anomalies ΔT_3 are probably too small to be noticed. Inspecting $\Delta T_1/Q$ and $\Delta T_2/Q$ in the right hand columns, $\Delta T_1/Q \sim 10$ quite consistently, while ΔT_2 is not a good indicator of Q. As shown in Table 7 with type 2, MSU 1 saturates to yield $\Delta T_1 \sim 44$ K if an amount Q of cloud reaches about 3 mm. This can lead to variations in $\Delta T_1/Q$ as shown with measurement A in Table 10.

The results in this section appear to be a substantial advance on those of Hubert et al. (1981), who found it necessary to invoke water contents as high as 1-2 g/m^3 through considerable depths of the troposphere in order to explain observed microwave measurements using a simple treatment.

Summarizing inferences on the nature of distributions of water in the monsoon depression, dropwindsonde and SMMR data (Table 2, and Figs. 13a-15a, respectively) indicate water vapor amounts near 65 mm. SMMR clearly shows increases to more than 70 mm in the northeast Bay.

From MSU, Figs. 33-35 imply that fair weather cloudiness involves $\Delta T_1 \sim 1.5$ K, after tentative drawings of dashed lines. From studies of hydrometeor distribution types 1 and 2 in Tables 7 and 10, this cloudiness probably corresponds with $\Delta T_1/Q \sim 20$ K/mm. This implies $Q \sim 0.075$ mm. Unfortunately, variations of conditions at the surface preclude checking this

from SMMR. (The results in Figs. 13b-15b are too insensitive to indicate reliably such a small signal.) Using the SMMR aboard SEASAT, Njoku and Swanson (1983) get results very similar to this one, with cloud water increasing from 0.04 to 0.12 mm northeastward across the Bay, during the period 11 July - 10 August 1978. Their results are based on the Wilhiet and Chang (1980) algorithms for vapor and cloud water, with modifications documented in Lipes (1981). Why with Nimbus-7 has it not been possible to follow directly the methods of Njoku and Swanson with SEASAT? First, the data studied here involve only one particular storm rather than a whole month. Second, the instrument calibration (Lipes, 1981) is probably better in the case of SEASAT. Warned by T. T. Wilheit and N. C. Grody (personal communications) as to the dangers of using the 6.6 and 10.69 GHz SMMR channels near land (as required in Wilheit and Chang, 1980), because of antenna side-lobes, the compensations for surface conditions built into the Wilheit and Chang algorithms were not available. Njoku and Swanson (1983) did not express worry about this; it seems remarkable that their results and the present results agree so well.

In cloudy areas in the monsoon depression, typified by points A to D in Figs. 33-35 and Table 10, it is found that liquid water contents of lower tropospheric cloud near 6 mm are likely, covering several tenths of horizontal areas of order 10^4 km^2. Rain amounts near 1 mm covering ~ 10% of such areas are inferred. The rain appears to be such as to lead to values of $(\Delta T_1/\Delta T_2)$ nearer (43/-24) than (1.4/-20), to be closer to type 3 rather type 4 in Table 7. This implies concentration of water at relatively low levels in the troposphere, and relatively small effects of scattering (which in turn implies relatively small drop sizes).

It has not been found easy to reconcile observed combinations of ΔT_1 and ΔT_2 with appreciable amounts of melting snow - of area coverage by a radar bright band near the melting level.

10. Potentialities of microwave sounders

This research was conceived with the idea of discerning by satellite dense high overcast existing over clear areas below, as opposed to dense high overcast plus low level cumulus. For the frequency range covered by MSU, brightness temperatures (TB, K) are plotted against frequency in Fig. 38, for four different atmospheres A, B, C and D as indicated. Curve A is due to the moist sounding from 5 July, 0416:36 GMT used as the background for Table 7 (without hydrometeors). Curve B is due to A plus cumulus type 2d (A+2d). Curve C is due to (A+2d+5b). Curve D is due to (A+5b). Vertical lines indicate the four MSU frequencies. The problem is: With choices of a few more MSU channel frequencies, could one discriminate between the various possibilities, A, B, C or D? Relative to curve A, the effect of low absorbing cloud is to shift the curve upward, while the effect of high scattering hydrometeors is to shift it downward. It would be difficult to distinguish a small upward shift from the sum of a large upward plus a small downward shift, without use of several frequencies.

Suppose that a number of measurements were available between 50.30 GHz (MSU 1) and 53.73 GHz (MSU 2). Those at lower frequencies could be used to determine surface temperature and wind speed, and temperatures and the hydrometeor content at low levels. Higher frequency channels would be useful in discriminating between different possibilities at upper middle levels.

11. Diurnal variations shown by MSU

A series of maps from MSU has been shown in Figs. 6-9. Evolution of patterns of brightness temperature is documented further in Figs. 39 and 40. Particular temperature contours from MSU 3 and MSU 2 are overlaid in Fig. 39; daytime contours (left) have been separated from night-time contours (right). The contours shifted northward at night.

Brightness temperatures from MSU 3 show warm air over the northern Bay, but otherwise no very striking patterns. Signs of a westward-propagating upper tropospheric wave were sought, to investigate the possibility of triggering of monsoon depressions from the upper troposphere. None have been found.

Brightness temperatures from MSU 2 imply cold air intruding northward, with greatest penetration late on 4 July. By day, to the west, warm temperatures were found in lobes convex toward the south. Patterns suggesting a trough and a ridge may be discerned in Fig. 39 (bottom left), from 3-6 July. From Eq. (3), the magnitude of this thermal difference, between warm air to the west and cold air to the east, is found to be roughly 6 K. The 259 K contour shown in Fig. 39 (bottom) generally circumscribed colder areas implying rain.

Fig. 39 (left versus right) shows marked diurnal variations in the depression. To examine these further, time series are shown in Fig. 40. Before 5 July, before the depression affected the points chosen for examination, diurnal variations in MSU 3 temperatures may be seen clearly. Upon arrival of the depression, gradual slight cooling occurred. MSU 2 and MSU 1 give less obvious suggestions of diurnal variations, probably because of strong effects associated with liquid water.

The times of diurnal extremes in situations like this are expected to be near 0900 and 1900 local time (Houze et al., 1981b; Murakami, 1983). Therefore the MSU measurements, near 1500 and 0330 local time, are unlikely to show up the full amplitude of the diurnal variations.

Murakami (1983) found that convection was enhanced over ocean areas around 0900 local time and was relatively weak during the evening, while the opposite occurred over adjacent land areas. He shows (in his Fig. 10) a maximum in diurnal variation of deep convection over the Ganges valley near 87°E, 24°N during July 1979, diminishing gradually southward over the Bay. Examining Fig. 40 for MSU 2, it seems that this pattern may apply to the case of the monsoon depression. Marked variations are found here in temperatures from MSU 3 (Fig. 40 top): these may be connected with the Tibetan Plateau. Luo and Yanai (1983) demonstrate diurnal variations over the Plateau which extend through the whole troposphere.

12. Summary

This work was undertaken to explore the characteristics of a monsoon depression as revealed by satellites. Satellite views have been compared with diverse observations made during penetrations of the storm.

In Section 2 conventional analyses were presented for 5 and 7 July. These showed the early development over the Arakan Mountains of Burma, from strong low-level westerly winds over the Bay, and the mature stage of the storm in the central Bay.

Maps from the Microwave Sounding Unit on TIROS-N were presented in Section 3. MSU Channel 3 reveals thermal characteristics around 300 hPa. The patterns remained similar throughout the period of the storm, and implied that it was primarily a low-level phenomenon. MSU 2 (for 700 hPa) showed an irregular sequence of cold anomalies. These were linked to hydrometeors

in Section 9. Circular patterns as obtained by streamline analyses were not found. MSU 1, responsive to conditions near and at the surface, indicated gradients of brightness temperature along the direction of low-level flow, and positive anomalies linked to hydrometeors in Section 9. The MSU series was dominated by the effects of convective clouds.

Airborne dropwindsonde data were presented in Section 4, together with MSU brightness temperatures at corresponding locations. A program of radiative transfer was developed, using modern background data in matters of detail. When the treatment of diffuse scattering at the sea surface by Wentz (1983) was included, excellent agreement was obtained between measured and calculated brightness temperatures in MSU 2 and MSU 1. The latter showed an offset attributable to low-level clouds, at this stage not included in the calculation. Air temperatures at 700 hPa (T_{700}) were compared with MSU 2 brightness temperatures (T_2), with the result $\partial T_2 / \partial T_{700} \sim 0.49$. Great scatter was found in plots of T_2 against T_{700}, due to surface effects and to hydrometeors, so that it is evidently not possible to retrieve T_{700} in this storm from the TIROS-N configuration of MSU.

Maps from the Scanning Multichannel Microwave Radiometer (SMMR) aboard Nimbus-7 were explored in Section 5. For occasional periods of data collection (on 3 and 7 July) maps were made of water vapor, cloud water and rainfall rate. A technique from Grody et al. (1980) was adapted to the present case. Only the frequencies 18 and 21 GHz were used for vapor and cloud water over the Bay; the proximity of the coast made hazardous the use of lower frequencies (as in Chang and Wilheit, 1980, and Njoku and Swanson, 1983). For rainfall, the 37 GHz channel was used. The method yielded artificial minima of vapor in the presence of rain, until improved by allowance for relatively large hydrometeors. Results showed that water vapor increased

from values near 65 mm to values exceeding 70 mm along the direction of low level winds across the Bay. Cloud water amounts reached maxima near 2 mm. Rainfall rates exceeded 5.7 mm/h (radar reflectivity: 35 dBZ) over a few percent of the area of the Bay north of 10°N. Amounts of very light rain probably were overestimated.

Also from Nimbus-7, images were displayed from the Temperature Humidity Infrared Radiometer (THIR) in Section 6. This sequence of infrared window images (at 11.5 μm) and water vapor images (at 6.7 μm) showed no circular structures (as in streamline analyses). Clouds were aligned in bands oriented east-west, changing configuration over periods of 12 h. The 6.7 μm channel revealed discontinuities in moisture oriented NE-SW, with connections across the Himalayas to mid-latitude systems. These features evidently were related to flows in the upper troposphere; it seems that probably they were not of primary importance for the monsoon depression. Any singularities in moisture in the low troposphere over the Bay were not revealed by THIR.

To further explore precipitation in Section 7, statistics from the C-band weather radar aboard the WP-3D aircraft were compiled. There are problems with these due to the great vertical beamwidth of the radar, 4.1°, and due to wobble of the radar because its stabilization could not always keep up with wobbles of the aircraft. At high flight levels, substantial returns from melting hydrometeors seem likely, contributing to percentages greater than 10 for the interval 30-35 dBZ recorded at 483 hPa on 5 July. Peak reflectivities exceeded 50 dBZ (rainfall rate ~ 103 mm/h) in bins measuring 2 km x 2 km in convective clouds. Mean rainfall rates near 0.5 mm/h were recorded in the low troposphere on 7 July. Half of this fell at rates near 1.5 mm/h in areas covering 17-19% of the total. Corresponding numbers from SMMR were 1.2-7.6%; the areas of coverage and times were different. With known

deficiencies in the radar due to large vertical beamwidth, and due to oversimplification in the SMMR 37 GHz rain sensing method (poor at very small and very great rates), only a rough agreement between the two methods was found.

Excellent aircraft data were obtained through areas of heavy precipitation on 5 July, when great anomalies of brightness temperature were measured using MSU 1 and MSU 2. These were examined in Section 8, to see the cause of the anomalies. It was a line of very deep showers oriented east-west and propagating southward into a region of unstable stratification featuring numerous cumulus castellanus in the low troposphere. These clouds were oriented in lines along the shear and across the flow, in a manner quite different from cloud streets often found under conditions of subsidence. Updraft cores were intense, one reaching a peak of 15.7 m/s at 323 hPa. The stratification north of the line was stable. Photogrammetry from the Electra aircraft, flying in the western half of the Bay, showed that haze occurred at levels up to 600 hPa south of the line. Dense high overcast involved cloud layers between about 450 and 220 hPa. Highest measured cirrus elements were near 140 hPa. These findings from 5 July were similar in general character to results found by Warner and Grumm (1984) for 7 July.

With the foregoing background of knowledge, attempts were made in Section 9 to explain the various combinations of brightness temperatures measured in MSU 1 and MSU 2. Section lines were drawn around the Bay in three of the maps from the MSU sequence, and profiles of measured brightness temperatures T_1 and T_2 were drawn. Dropwindsonde results were used to determine approximately the magnitudes of anomalies ΔT_1 and ΔT_2 due to hydrometeors. Various vertical distributions (types $i = 1$ to 8) of

hydrometeors were compiled in a manner consistent with the observations. These were examined to find individually ΔT_{1i} and ΔT_{2i} (i = 1, 8). Combinations of different amounts and area coverages of types i were chosen to yield the measured anomalies found in different places in the storm.

In treating the individual types i, the handling of cloud particles was straightforward. For scatterers like raindrops one needs extinction coefficients, and single scattering albedos. If effects of scattering are not to be overestimated, one needs to treat secondary scattering into the beam, not just primary scattering out of it. This was dealt with arbitrarily by multiplying assessed albedos by 2/3. Radiative properties of ice anvils were calculated using spectra measured during MONEX, and provided by John Gamache at the Center for the Environment and Man. The particles were converted into equivalent spheres for this purpose - a crude business. The bright band of melting ice was treated by assuming characteristics like those of rain, but with an enhanced single scattering albedo. It was found that characteristics in respect of MSU were such that low clouds of fine particles enhanced ΔT_1 markedly while affecting ΔT_2 hardly at all. "Saturation" in ΔT_1 as column water increased occurred with a few millimeters of low cloud water. Rain, and ice, yielded negative ΔT_2; accompanying ΔT_1 was sensitive to the treatment of scattering.

The observed combinations ΔT_1, ΔT_2 could be explained satisfactorily by the modeling. Often, large amounts of low cloud were implied - up to 35% coverage at several millimeters of water. On the other hand, amounts of bright band, with hydrometeors above and below, most likely did not cover more than ~ 10% of any MSU footprint (of area ~ 5 x 10^4 km^2): calculated values of -ΔT_2 were relatively great for this type of hydrometeor distribution. It was found also that amounts of heavy rain were small, and that the

observations of ΔT_1 and ΔT_2 could not be explained plausibly unless single scattering albedos were reduced from nominal values (by the factor 2/3) to cater for secondary scattering. The results implied a prevalence of ~ 0.075 mm of low level cloud water over the Bay, in agreement with SEASAT results by Njoku and Swanson (1983). Total amounts of cloud water were always < ~ 3 mm, in agreement with results from SMMR on Nimbus-7. Anomalies in MSU 3 brightness temperature were always < ~ 0.6 to 0.4 K. The latter value appears to be the correct one, because anomalies attributable to hydrometeors were not obvious in MSU 3 patterns.

An ice anvil was found to have a relatively small effect on MSU brightness temperatures, unless shallow cumulus lay below. The anomaly due to the shallow cumulus then was substantially redressed by the anvil. In Section 10, calculations were performed for various types of hydrometeor distribution as a continuous function of frequency, to explore further the potential for elucidating atmospheric structure using microwave radiances. The different atmospheres showed different patterns of variation in the frequency range MSU 1 to MSU 2 (50.30 to 53.73 GHz), implying that use of several frequencies in this range could lead to useful descriptions of hydrometeors.

The MSU views of the monsoon depression constitute a very complete twice daily coverage, at about 1500 and 0330 local time. Diurnal variations were examined in Section 11. The meridional patterns of brightness temperatures, with T_3 in MSU 3 and T_2 in MSU 2 generally increasing northward, were found to migrate northward by night and southward by day. The presence of an effect at ~ 300 hPa (in MSU 3) implies that the Tibetan Plateau had an influence as far south as the Bay. Results were consistent with

diurnal variations found by Murakami (1983) in connection with cumulus convection.

13. Conclusions

This study yields conclusions in respect of the monsoon depression in particular, and in respect of satellite remote sensing in general.

A.   On the SMONEX monsoon depression

Outstanding in this research has been the finding of prevalence of convective showers in the monsoon depression, and the absence of patterns showing nearly circular symmetry. When one has rawinsonde wind data spaced at intervals of a degree or so, one analyses smoothly turning stream-lines (Nitta and Masuda, 1981; Sanders, 1984). Repeatedly one finds from aircraft and satellite data that discontinuities occur across lines of convection. New observational and theoretical approaches seem to be required to achieve satisfactory monitoring of such storms, and fuller understanding.

It appears that the depression started over the Arakan Mountains of Burma as a result of strong west-southwesterly low-level flow in the central Bay impinging on the mountains, and being sustained by forcing on a scale of several degrees of latitude (Warner and Grumm, 1984, after Krishnamurti and Ramanathan, 1982). It did not start propagating westward across the Bay until 5 July.

On 5 July, convergence and ascent was concentrated along a line of very deep and intense cumulonimbi oriented WNW-ENE at which the low-level flow converged, yielding ascent. The stratification was unstable in the incident flow, in which grew cumulus castellanus leading to haze at levels up to 600 hPa. North of the region of ascent, stratification was relatively stable and layers of stratus were found. The cloud line region of marked ascent propagated into the unstable air. Such cloud line features were documented

43

on 7 July (Warner and Grumm, 1984). Similar patterns have been found on 8 July also (not shown).

From dropwindsonde and Nimbus-7 SMMR data, water vapor amounts were near 65 mm in the depression over the Bay, increasing to more than 70 mm to the northeast. Cloud water amounts were generally near 0.075 mm over the Bay; peak values were near 2 mm. Rainfall rates exceeding 5.7 mm/h occurred over a few percent of the area of the Bay. Rates exceeding 1.5 mm/h covered areas approaching 15-20% (from airborne radar data on 7 July). Mean rainfall rates in areas of order 20,000 km² reached ~ 0.5 mm/h.

From exploration of brightness temperature anomalies in MSU 1 and MSU 2, it was inferred that over areas near 50,000 km² shallow cumulus updrafts and cumulus remnants contributed substantial amounts of liquid water, up to several millimeters over ~ 30% area coverage. Area coverage by heavy rain appeared to be relatively small (up to amounts such as 1 mm over 5% area coverage - or 0.5 mm over 20%). Calculated results implied the absence of large area coverage by radar bright band due to melting hydrometeors.

Patterns of MSU Channel 3, reflecting temperatures at levels near 300 hPa, changed little during the course of the depression. This implies that events in the upper troposphere played only a minor role in its evolution. Connections did occur across the Himalayas to mid-latitudes, as seen in 6.7 μm water vapor imagery from the Nimbus-7 THIR. Diurnal variations occurred in brightness temperatures of MSU 3, which implies that diurnal variations over the Tibetan Plateau (Luo and Yanai, 1983) were felt as far south as the Bay.

Diurnal variations in MSU patterns occurred prior to the depression, and became less distinct after 0000 GMT, 5 July. They were not discerned in MSU 1 over the Bay.

MSU 2 patterns showed warm brightness temperatures to the west of 88°E and cold brightness temperatures to the east, from 3-6 July by day. The night-time patterns featured propagation westward of a cold anomaly from 3-6 July. These features are consistent with the presence of convective clouds, with detailed configurations changing from day to day.

B.   On satellite remote sensing

In this work it was hoped to find quite a comprehensive description of the monsoon depression by satellite. This has not materialized. Only the Microwave Sounding Unit on TIROS-N, and measurements from GOES-1, have been available to yield data in appropriate quantities. TOVS product tapes were very poor in area coverage. Measurements from GOES-1 have been used by Warner and Grumm (1984) to follow a cloud line, but not exploited further because only conventional visible imagery was available.

This work points to a need to replace reliance on rawindsondes by reliance on satellites, the main point being the vital importance of continuous coverage in the horizontal, to cover convective cloud systems. The distribution of deep convection in a storm such as the SMONEX monsoon depression must be mapped, if it is to be properly monitored. The distributions of cloud lines, and the magnitudes of discontinuities in meteorological fields across them, should be known. Penetration of anvil cirrus should be possible, to distinguish the areas of upward motion (concentrated in cumulus) from areas of mesoscale downdrafts and inactive areas. In this respect of horizontal area coverage and cloud penetration, microwave sounders seem satisfactory; their

use seems to be essential. At present, MSU seems more promising than SMMR for the tropics, because SMMR yields swaths only 7° wide in longitude, spaced 26° apart. The low frequencies of SMMR at 6.6 and 10.69 GHz are suitable for obtaining sea surface temperatures and surface winds (Lipes, 1981), but one needs antenna patterns which match those at higher frequencies.

Turning to particulars of research findings using SMMR on Nimbus-7 and MSU on TIROS-N in the present study, it seems that water vapor contents were obtained satisfactorily from SMMR at 18 and 21 GHz, using the approach of Grody et al. (1980). This method seems not as good as that of Wilheit and Chang (1980) for areas remote from land where antenna side-lobe effects can be ignored, so that the 6.6 and 10.69 GHz channels can be used to determine surface conditions. To use the method of Wilheit and Chang (1980), good calibration of the radiometers is important (Lipes, 1981). This seems to mean that trial and error comparisons with independent data are necessary with any new satellite instrument. It was found in getting water vapor by the method of Grody et al. (1980) that an allowance for scattering by large hydrometeors was important [see Eq. (6a)]. Cloud water contents obtained by the method after Grody et al. (1980) gave only rough indications in this storm, and failed to properly reveal roughly uniform cloud water contents of magnitude ~ 0.075 mm inferred after many airborne cloud photographs plus results from MSU. In getting cloud water, noise due to variations in surface conditions was very obstructive.

Rainfall rates obtained from radiances with horizontal polarization at 37 GHz [Eq. (8)] were poor at low rates and would have been poor at rates exceeding 18 mm/h; the maximum rate found here was 13 mm/h.

Comparisons were made between dropwindsonde measurements yielding calculated brightness temperatures in MSU 1 and MSU 2, and corresponding measured brightness temperatures. Care was taken in use of modern background information (Klein and Swift, 1977; Liebe et al., 1977) for the calculations. Results became good after inclusion of Wentz's (1983) treatment of diffuse scattering at the sea surface.

Attempts were made to explain combinations of anomalies ΔT_1 and ΔT_2 in brightness temperatures from MSU 1 and MSU 2, attributable to hydrometeors. These were apparently quite successful. It was found necessary to consider scattering, and to cope with secondary scattering; this was done by multiplying single scattering albedos by 2/3. Methods for treating ice clouds which involve treating the particles as spheres seem unsatisfactory. Crude treatments of melting snow also might be improved. An ice anvil was found to have substantial effects on brightness temperatures T_1 when it overlaid shallow cumulus and cumulus remnants. Light rain was found to yield ratios $\Delta T_1/\Delta T_2$ of ~ -1.8, while heavy rain yielded ~ -0.07. It was impossible to reconcile the latter with the observed ratios near -7. This implies concentration of water at relatively low levels in the troposphere, and relatively small effects of scattering.

A study of brightness temperature as a continuous function of frequency in the range 50 to 58 GHz, for four different atmospheres varying in hydrometeor content, indicated different patterns of variation at the low frequencies between those of MSU 1 and MSU 2. Use of a multichannel microwave sounder would seem promising.

47

Acknowledgements

REFERENCES

Austin, P. M., and S. G. Geotis, 1979: Raindrop sizes and related parameters for GATE. J. Appl. Meteor., 18, 569-575.

Battan, L. J., S. R. Browning, and B. M. Herman, 1970: Tables of the radar cross sections of dry and wet ice spheres. Tech. Rep. No. 21, The Univ. of Arizona, Institute of Atmos. Phys., 11 pp.

Bennetts, D. A., and M. Ouldridge, 1984: An observational study of the anvil of a winter maritime cumulonimbus cloud. Quart. J. Roy. Meteor. Soc., 110, 85-103.

Chang, A. T. C., and T. T. Wilheit, 1979: Remote sensing of atmospheric water vapor, liquid water, and wind speed at the ocean surface by passive microwave techniques from the Nimbus 5 satellite. Radio Sci., 14, 793-802.

Churchill, D. D., and R. A. Houze, Jr., 1984: Mesoscale updraft magnitude and cloud-ice content deduced from the ice budget of the stratiform region of a tropical cloud cluster, J. Atmos. Sci., 41, to appear.

Grody, N. C., 1983: Severe storm observations using the Microwave Sounding Unit. J. Climate Appl. Meteor., 22, 609-625.

_____, and W. C. Shen, 1982: Observations of Hurricane David (1979) using the Microwave Sounding Unit. NOAA Tech. Rep. NESS 88, 52 pp.

_____, A. Gruber and W. C. Shen, 1980: Atmospheric water content over the tropical Pacific derived from the Nimbus-6 scanning microwave spectrometer. J. Appl. Meteor., 19, 986-996.

_____, C. M. Hayden, W. C. C. Shen, P. W. Rosenkranz and D. M. Staelin, 1979: Typhoon June winds estimated from scanning microwave spectrometer measurements at 55.45 GHz. J. Geophys. Res., 84, 3689-3695.

Herzegh, P. H., and P. V. Hobbs, 1980: The mesoscale and microscale struc-
ture and organization of clouds and precipitation in midlatitude cyclones.
II: Warm-frontal clouds. J. Atmos. Sci., 37, 597-611.

Houze, R. A., Jr., S. G. Geotis, F. D. Marks, Jr., D. D. Churchill and P.
M. Herzegh, 1981a: Comparison of airborne and land-based radar
measurements of precipitation during Winter MONEX. J. Appl. Meteor.,
20, 772-783.

_____, _____, _____, and A. K. West, 1981b: Winter monsoon convection in
the vicinity of North Borneo, Part I: Structure and time variation of the
clouds and precipitation. Mon. Wea. Rev., 109, 1595-1614.

Hubert, L. F., N. C. Grody, A. Timchalk and W. C. Shen, 1981: The effect
of precipitation on microwave soundings in low latitudes. NOAA Tech.
Rep. NESS 82, 34 pp.

Hwang, P. H. (ed.), 1982: Nimbus 7 Temperature Humidity Infrared
Radiometer (THIR) Data User's Guide. NASA Goddard Space Flight
Center, Greenbelt, MD.

Ishimaru, A., and R. L.-T. Cheung, 1980: Multiple-scattering effect on
radiometric determinations of rain attenuation at millimeter wavelengths.
Radio Sci., 15, 507-516.

Jorgensen, D. P., 1984: Mesoscale and convective characteristics of mature
hurricanes. Part I: Recent aircraft observations. J. Atmos. Sci., to
appear.

_____, and P. T. Willis, 1982: A Z-R relationship for hurricanes. J. Appl.
Meteor., 21, 356-366.

Klein, L. A. and C. T. Swift, 1977: An improved model for the dielectric
constant of sea water at microwave frequencies. IEEE J. Oceanic Eng.,
OE-2, 104-111.

Krishnamurti, T. N., and Y. Ramanathan, 1982: Sensitivity of the monsoon onset to differential heating. J. Atmos. Sci., 39, 1290-1306.

_____, _____, P. Ardanuy, R. Pasch and P. Greiman, 1980: Quick Look "Summer MONEX Atlas" Part III Monsoon Depression Phase. FSU Rep. No. 80-8. Dept. of Meteor., Florida State University, Tallahassee, 135 pp.

Lauritson, L., G. J. Nelson and F. W. Porto, 1979: Data extraction and calibration of TIROS-N/NOAA radiometers. NOAA Tech. Mem. NESS 107, 58 pp.

Le Marshall, J. F., W. L. Smith and G. M. Callan, 1984: Hurricane Debby - analysis and numerical forecasts using VAS soundings. Postprints, 15th Conf. on Hurricanes and Tropical Meteor., Jan. 9-13, Miami, FL. Amer. Meteor. Soc., Boston, 140-144.

Liebe, H. J., G. G. Gimmestad and J. D. Hopponen, 1977: Atmospheric oxygen microwave spectrum - experiment versus theory. IEEE Trans. Ant. Prop., AP-25, 327-335.

Lipes, R. (ed.), 1981: SMMR Mini-Workshop IV. Publ. 622-634, Jet Propulsion Laboratory, Pasadena, CA 135 pp.

Luo, H., and M. Yanai, 1983: The large-scale circulation and heat sources over the Tibetan Plateau and surrounding areas during the early summer of 1979. Part I: Precipitation and kinematic analyses. Mon. Wea. Rev., 111, 922-944.

Madrid, C. R. (ed.), 1978: The Nimbus 7 User's Guide. NASA Goddard Space Flight Center, Greenbelt, MD.

Marks, F. D., Jr., 1984: Evolution of the structure of precipitation in Hurricane Allen. Mon. Wea. Rev., submitted.

Murakami, M., 1983: Analysis of the deep convective activity over the Western Pacific and Southeast Asia Part I: Diurnal variation. J. Meteor. Soc. Japan, 61, 60-76.

Nitta, T., and K. Masuda, 1981: Observational study of a monsoon depression developed over the Bay of Bengal during Summer MONEX. J. Meteor. Soc. Japan, 59, 672-682.

Njoku, E. G., and L. Swanson, 1983: Global measurements of sea surface temperature, wind speed and atmospheric water content from satellite microwave radiometry. Mon. Wea. Rev., 111, 1977-1987.

Olsen, R. L., D. V. Rogers and D. B. Hodge, 1978: The aR^b relation in the calculation of rain attenuation. IEEE Trans. Ant. Prop., AP-26, 318-329.

Pike, A. C., 1984: Geopotential thicknesses vs. heights as predictors of Atlantic tropical cyclone motion and intensity. Postprints, 15th Conf. on Hurricanes and Tropical Meteor., Jan. 9-13, Miami, FL. Amer. Meteor. Soc., Boston, 145-150.

Ray, P. S., 1972: Broadband complex refractive indices of ice and water. Appl. Optics, 11, 1836-1844.

Rosenkranz, P. W., 1975: Shape of the 5 mm oxygen band in the atmosphere, IEEE Trans. Ant. Prop., AP-23, 498-506.

Ruprecht, E., and W. M. Gray, 1976: Analysis of satellite-observed tropical cloud clusters II. Thermal, moisture and precipitation. Tellus, 28, 414-425.

Sanders, F., 1984: Quasi-geostrophic diagnosis of the monsoon depression of 5-8 July 1979. J. Atmos. Sci., 41, 538-552.

Scorer, R. S., and H. Wexler, 1963: A Color Guide to Clouds. Pergamon Press, Oxford, 63 pp.

Simpson, J. and V. Wiggert, 1971: 1968 Florida cumulus seeding experiment: numerical model results. Mon. Wea. Rev., 99, 87-118.

Velden, C. S., and W. L. Smith, 1983: Monitoring tropical cyclone evolution with NOAA satellite microwave observations. J. Climate Appl. Meteor., 22, 714-724.

_____ and _____, 1984: Quantitative satellite applications - Tropical cyclone intensity monitoring and track forecasting. Postprints, 15th Conf. on Hurricanes and Tropical Meteor., Jan. 9-13, Miami, FL. Amer. Meteor. Soc., Boston. 159-162.

Warner, C., 1981: Photogrammetry from aircraft side camera movies: Winter MONEX. J. Appl. Meteor., 20, 1516-1526.

_____, 1982: Mesoscale features and cloud organization on 10-12 December 1978 over the South China Sea. J. Atmos. Sci., 39, 1619-1641.

_____, 1984a: Core structure of a Bay of Bengal monsoon depression. Mon. Wea. Rev., 112, 136-152.

_____, 1984b: Stereo-pair photographs of monsoon clouds. Bull. Amer. Meteor. Soc., 65, 344-347.

_____, and R. H. Grumm, 1984: Cloud distributions in a Bay of Bengal monsoon depression. Mon. Wea. Rev., 112, 153-172.

_____, and D. P. McNamara, 1984: Aircraft measurements of convective draft cores in MONEX. J. Atmos. Sci., 41, 430-438.

Waters, J. W., 1976: Absorption and emission by atmospheric gases. In Methods of Experimental Physics, Vol. 12(B), M. L. Meeks (ed.), Academic Press, 142-176.

Weinman, J. A., and R. Davies, 1978: Thermal microwave radiances from horizontally finite clouds of hydrometeors. J. Geophys. Res., 83, 3099-3107.

Wentz, F. J., 1983: A model function for ocean microwave brightness temper-
atures. <u>J. Geophys. Res.</u>, 88, 1892-1908.

Wilheit, T. T., and A. T. C. Chang, 1980: An algorithm for retrieval of
ocean surface and atmospheric parameters from the observations of the
scanning multichannel microwave radiometer. <u>Radio Sci.</u>, 15, 525-544.

TABLE 1.   MSU PARAMETERS

Scan spot	Zenith angle (°)	Area (10⁴ km²)	Limb corrections (K)		
			Channel 1 50.30 GHz	Channel 2 53.73 GHz	Channel 3 54.96 Ghz
1	56.6	18	-21.1	14.9	12.3
2	44.2	9.6	-15.6	8.0	7.5
3	32.7	6.2	-10.0	4.2	4.1
4	21.7	4.7	-5.0	1.8	1.8
5	10.7	4.0	-1.4	0.4	0.5
6	0	3.8	0	0	0
7	10.7	4.0	-1.4	0.3	0.3
8	21.7	4.7	-5.0	1.3	1.4
9	32.7	6.2	-10.0	3.4	3.4
10	44.2	9.6	-15.6	7.1	6.5
11	56.6	18	-21.1	13.6	10.9

TABLE 2. DROPWINDSONDE DATA.

Lat (°N)	Long (°E)	GMT	A/c	P_{max} (hPa)	Sfc wind speed (m/s)	P_{Sfc} (hPa)	T_{Sfc} (K)	Water vapor (mm)	MSU 1 M ~200 (K)	C	M-C	MSU 2 M ~200 (K)	C	M-C	$T_{700 hPa}$ (C)
3 July															
18.96	87.98	0355:35	P	998	9	1000	302.7	65.7	34.0	34.5	-0.5	59.8	59.0	0.8	10.6
16.50	86.49	0428:35	P	996	13	1000	303.1	55.8	34.9	34.0	0.9	60.2	59.1	1.1	9.8
14.95	83.49	0506:45	P	1003	14	1004.3	303.0	53.0	34.0	33.3	0.7	59.2	58.9	0.3	10.8
13.05	90.00	0818:35	P	998	13	1000	301.4	59.7	39.5	34.5	5.0	58.9	58.4	0.5	9.5
12.99	87.51	0751:55	P	999	13	1000	302.6	59.4	38.0	34.7	3.3	58.8	58.8	0	9.9
12.02	83.50	0539:25	P	1002	9	1003.2	302.7	50.8	34.2	30.3	3.9	58.7	58.5	0.2	10.1
5 July															
19.77	88.59	0534:13	E	953	7	1000	302.6	61.8	41.4	32.0	9.4	59.3	58.2	1.1	9.9
17.72	89.65	1028:57	P	998	8	1000	300.2	63.4	43.0	32.5	10.5	58.3	58.3	0	9.4
16.98	92.24	0416:36	P	992	8	1000	300.0	65.0	56.5	33.4	23.1	56.0	58.6	-2.6	11.6
15.03	87.23	0640:15	E	1011	9	1012	302.7	(72.6)	38.0	36.6	1.4	59.0	59.6	-0.6	11.9
14.01	90.01	0948:23	P	995	15	1000	302.5	58.8	39.3	35.4	3.9	58.8	59.5	-0.7	12.3
13.97	92.64	0451:03	P	993	12	1000	303.2	59.0	40.0	34.8	5.2	59.0	59.3	-0.3	11.2
13.33	95.49	0524:30	P	989	13	1000	302.5	56.5	37.5	34.0	3.5	58.8	59.0	-0.2	10.0
13.03	84.05	0828:45	E	995	9	1000	303.4	60.9	35.9	33.2	2.7	58.4	58.9	-0.5	11.4
11.25	90.00	0918:05	P	991	15	1000	302.9	63.7	38.7	36.5	2.2	58.8	59.0	-0.2	11.1
10.46	86.05	0744:05	E	1002	9	1003.6	302.8	61.1	36.5	33.2	3.3	58.3	58.5	-0.2	10.5
6 July															
19.54	92.31	0945:07	P	989	11	1000	301.3	(69.8)	46.0	36.3	9.7	59.8	59.6	0.2	12.8
14.56	87.47	0622:47	P	992	14	1000	302.7	54.2	38.0	34.3	3.7	59.0	59.0	0	11.1
11.97	86.97	0709:47	P	983	13	1000	303.8	63.0	37.5	36.2	1.3	58.4	59.4	-1.0	12.2
7 July															
20.51	90.52	1121:17	P	986	8	1000	302.5	(81.4)	44.5	37.8	6.7	61.2	60.1	1.1	13.7
18.59	89.05	1043:17	P	983	8	1000	301.4	(77.5)	42.7	36.6	6.1	59.6	60.0	-0.4	12.9
17.57	90.44	1023:47	P	992	12	1000	301.8	(74.7)	43.0	38.2	4.8	59.6	59.7	-0.1	11.8
16.38	92.09	0748:18	E	999	8	1000.6	301.3	(69.5)	43.0	34.6	8.4	59.4	59.1	0.3	13.3
15.87	87.09	0545:48	E	997	11	1000	301.7	66.0	38.0	35.3	2.7	59.3	58.5	0.8	10.6
14.09	92.02	0719:18	E	990	14	1000	302.8	54.9	41.9	34.3	7.6	58.4	59.3	-0.9	12.2
8 July															
21.09	89.01	0328:38	E	994	6	1000	302.7	66.8	-	33.7	-	60.7	59.4	1.3	12.6
21.00	88.91	0316:37	P	986	8	1000	302.7	67.6	-	34.7	-	60.7	59.7	1.0	13.2
20.11	89.45	0344:08	E	1003	8	1004.1	301.1	67.8	41.6	34.2	7.4	60.6	59.0	1.6	12.1
19.53	87.97	0859:05	E	982	12	1000	302.8	67.7	41.4	36.7	4.7	60.6	60.3	0.3	13.5
19.27	86.54	0351:37	P	990	10	1000	302.2	(70.7)	-	36.1	-	60.6	59.7	0.9	13.4
18.12	90.34	0754:30	E	1000	16	1001.8	301.8	65.8	40.9	37.5	3.4	60.0	59.5	0.5	12.2
18.10	87.07	0838:43	E	996	8	1000	302.5	(71.3)	40.0	35.6	4.4	60.5	59.5	1.0	13.0
17.97	87.52	0424:28	E	1011	16	1012	302.9	(74.5)	39.7	39.8	-0.1	60.3	60.7	-0.4	14.2
17.49	84.71	0421:07	P	989	8	1000	301.9	(68.6)	-	34.4	-	60.4	59.0	1.4	11.9
17.01	90.48	0739:16	E	1002	13	1003.2	302.8	58.5	39.2	34.8	4.4	59.6	59.3	0.3	11.3
14.97	82.53	0501:07	P	1000	4	1001.3	302.9	62.4	32.6	31.7	0.9	59.5	58.2	1.3	10.2
14.49	90.53	0706:45	E	1011	13	1012	302.5	59.1	37.5	35.0	2.5	58.9	59.8	-0.9	11.3
12.52	90.49	0642:00	E	1002	12	1003.1	302.5	56.3	37.7	34.0	3.7	58.0	58.9	-0.9	11.1
11.75	89.00	0621:09	E	1002	10	1003.7	302.1	54.8	35.5	32.1	3.4	57.9	58.3	-0.4	10.2
11.06	87.61	0602:08	E	995	12	1000	302.7	58.6	35.0	34.6	0.4	58.2	58.9	-0.7	10.3
(1)	(2)	(3)	(4)	(5)	(6)	(7)	(8)	(9)	(10)	(11)	(12)	(13)	(14)	(15)	(16)

TABLE 3. Upper-level sounding
extrapolation for use in calc-
ulation of radiative transfer

p (hPa)	T (K)	T_D (K)
10	235	222
30	219	206
50	209	196
70	201	188
100	193	180
150	208.5	195.5
200	220	207
300	239	226
400	257.2	247.2

TABLE 4. Area coverage by rainfall (%) from SMMR

Interval of rainfall rate R, mm/h (Interval of radar reflectivity Z, dBZ)	≥5.7 (≥35)	5.7>R≥2.4 (35>Z≥30)	2.4>R≥1.0 (30>Z≥25)	R̄ mm/h
3 July, 0552 GMT	0.2	1.0	1.2	0.06
7 July, 0523 GMT	3.1	4.9	7.6	0.47
7 July, 1813 GMT	2.3	2.4	4.1	0.28

TABLE 5. Area coverage by radar echoes. To translate reflectivities (Z, mm^6/m^3) into ice water content (I, g/m^3), rain water content (M, g/m^3) or rainfall rate (R, mm/h), the following equations are used:

$$I = 0.008 \; Z^{0.605} \quad \text{(Herzegh and Hobbs, 1980)}$$
$$M = 0.00078 \; Z^{0.76} \quad \text{(the R-Z relationship + Eq. 18)}$$
$$R = 0.0146 \; Z^{0.741} \quad \text{(Jorgensen and Willis, 1982)}$$

Reflectivity (Z, dB > 1 mm^6/m^3)	52±2	47±2	42±2	37±2	32±2	27±2	22±2	17±2
Ice content (I, g/m^3)				1.39	0.69	0.34	0.17	0.085
Water content (M, g/m^3)	7.0	2.9	1.2	0.50	0.21	0.088	0.037	0.015
Rainfall rate (R, mm/h)	103	44	19	8.0	3.4	1.5	0.62	0.27

Area coverage (%)

Date July	GMT	p (hPa)	T (°C)	Lat (°N)	Long (°E)	52±2	47±2	42±2	37±2	32±2	27±2	22±2	17±2	R̄
5	1001:22	327	-22	15.21	89.98					0.15	0.76	0.87		
7	0920-1016	387	-11						0.009	0.014	0.64	3.0	9.9	3.6
5	0356:33	483	-3	18.77	91.93	0.006	0.017	0.24	3.6	18.4	8.4			
5	0425:38	483	-3	16.19	92.31		0.31	1.5	5.1	9.1	2.7			
7	0635-0821	694	14			0.002	0.011	0.022	0.22	2.0	17.3			R̄ = 0.36 mm/h
7	0316-0607	945	25			0.004	0.026	0.089	0.61	5.5	19.4			R̄ = 0.56 mm/h

TABLE 6. Measurements of vertical air velocity

WP-3D aircraft

Position of peak draft (^{O}E, ^{O}N)	Pressure (hPa)	Time of peak draft (GMT)	Duration (s,m)	Peak draft (m/s)	Mean draft (m/s)	Mass flux (kg/s/m)
91.99, 19.28	504	0350:09	26.2,3990	5.2	2.6	6600
91.92, 18.99	489	0353:49	25.5,3600	5.9	3.5	7800
91.91, 18.96	485	0354:13	4.7,650	2.2	1.7	680
91.91, 18.94	482	0354:30	4.2,610	2.6	1.8	680
91.91, 18.88	483	0355:15	53.7,7980	4.6	2.5	12600
91.94, 18.74	482	0356:50	21.6,3180	4.6	3.2	6200
91.96, 18.67	482	0357:41	9.4,1360	4.5	2.7	2300
91.96, 18.65	483	0357:49	2.6,380	2.7	2.2	520
91.96, 18.65	483	0357:52	6.0,860	-3.3	-1.8	-970
89.94, 15.61	325	1005:47	30.1,5090	6.7	4.1	9400
89.93, 15.67	323	1006:28	88.8,15150	15.7	4.4	29500
89.95, 15.79	325	1007:47	30.0,5500	2.5	1.8	4300

Electra aircraft

Position of peak draft (^{O}E, ^{O}N)	Pressure (hPa)	Time of peak draft (GMT)	Duration (s,m)	Peak draft (m/s)	Mean draft (m/s)	Mass flux (kg/s/m)
88.08, 17.99	504	0558:28	5.2,740	2.9	2.2	1080
88.07, 17.96	504	0558:39	3.5,490	2.6	2.3	750
88.07, 17.98	504	0558:43	2.4,350	2.7	2.5	550
88.07, 17.98	504	0558:52	24.7,3520	3.0	2.0	4500
88.06, 17.94	504	0559:09	14.1,2020	2.3	1.5	2010
88.05, 17.90	504	0559:47	4.0,560	4.7	3.3	1200
88.04, 17.89	503	0559:56	14.6,2060	4.5	3.1	4100
88.03, 17.85	502	0600:23	7.3,1000	4.2	2.6	1700
88.03, 17.84	502	0600:34	9.3,1280	3.6	2.7	2200
88.01, 17.81	501	0601:03	16.4,2360	4.2	2.6	3900

TABLE 7. Types (i) of cloud distribution and resulting anomalies (ΔT, K) in brightness temperatures calculated for MSU Channels 1-3. For i = 3 to 8, calculations are with the single scattering albedo multiplied by 2/3. (Results in parentheses occur without this multiplication.)

Cloud distribution				Q (mm)	ΔT_1	ΔT_2 (K)	ΔT_3	$\dfrac{\Delta T_1}{\Delta T_2}$	$\dfrac{\Delta T_1}{Q}$	$\dfrac{\Delta T_2}{Q}$ (K/mm)	$\dfrac{\Delta T_3}{Q}$
1. Haze and	P_{top}	P_{base}	M/ρ_v								
1a. shallow	850 hPa	990	0.004	0.12	3.6	0.1	.0	36	30	0.8	.0
1b. cumulus	890	930	0.015	0.16	5.0	0.1	.0	50	31	0.6	.0
2. Cumulus		M_{max}	a								
2a. updraft	476 hPa	2 g/m³	0.4	6.77	45.6	-1.7	-0.2	-27	6.7	-0.25	-0.03
2b.	400	1	0.4	4.04	43.6	-1.7	-0.2	-26	11	-0.4	-0.05
2c.	500	1	0.3	3.24	44.2	-0.4	-0.1	-110	14	-0.1	-0.03
2d.	400	0.25	0.3	1.01	25.1	-0.2	.0	-125	25	-0.2	.0
3. Light	0.27 mm/h at 610 hPa			0.22	9.5	-5.3	-0.4	-1.8	43	-24	-1.8
rain	1.5 mm/h at 990 hPa				(-2.0	-8.1	-0.6	0.25	-9	-37	-2.7)
4. Heavy	1.5 mm/h at 610 hPa			0.64	0.9	-13.1	-1.1	-0.07	1.4	-20	-1.7
rain	3.4 mm/h at 990 hPa				(-21.8	-19.4	-1.6	1.1	-34	-30	-2.5)
5. Ice	0.05 g/m³ at 410 hPa			0.19	-0.5	-0.6	-0.1	0.8	-2.6	-3.2	-0.5
5a. anvil (a)	0.117 g/m³ at 530 hPa				(-0.9	-0.8	-0.2	1.1	-4.7	-4.2	-1.1)
Ice	0.05 g/m³ at 410 hPa			0.30	-0.8	-1.1	-0.3	0.7	-2.7	-3.7	-1.0
5b. anvil (b)	0.15 g/m³ at 530 hPa										
6. (5a and 1a)				0.31	3.1	-0.5	-0.1	-6.2	10	-1.6	-0.3
					(0.4	-1.0	-0.2	-0.4	1.3	-3.2	-0.6)
7. (5b and 2d)				1.31	15.9	-4.7	-0.9	-3.4	12	-3.6	-0.7
8. (5a and bright band and 3)	Bright band 550-590 hPa (1.5 mm/h)			0.49	-4.9	-15.6	-2.0	0.3	-10	-32	-4.1
					(-25.5	-23.1	-3.0	1.1	-52	-47	-6.1)

TABLE 8. Parameters of microwave transmission in the relationships $\gamma_e = AR^b$ for rain and $\gamma_e = CI$ for ice, and the ratio γ_a/γ_e. See text for explanation.

Instrument	Frequency (GHz)	Rain A	b	Ice C	γ_a/γ_e
MSU 3	54.96	0.155	0.884	0.040	0.14
MSU 2	53.73	0.149	0.890	0.036	0.15
MSU 1	50.30	0.127	0.906	0.029	0.17
SMMR	37	0.0606	0.985	0.0100	0.35
SMMR	21	0.0154	1.11	0.0030	0.77
SMMR	18	0.0106	1.13	0.0025	0.84
SMMR	10.69	0.003	1.17		
SMMR	6.6	0.00093	1.15		

TABLE 9. Ice particle size spectrum from SMONEX (after John Gamache), and calculated radiative characteristics for microwave channels, accumulating with inclusion of particles of increasing size from left to right.

		1	2	3	4	5	6	7	8	Table 8	Adopted values
Size class		1	2	3	4	5	6	7	8		
Equivalent spherical diameter (mm)		0.29	0.64	1.06	1.49	1.91	2.38	2.76	3.19		
No. per liter in size class		27.54	5.67	1.42	0.282	0.0995	0.0332	0.0168	0.0105		
I (g/m^3)		0.034	0.111	0.200	0.249	0.285	0.309	0.327	0.345		
MSU 3	γ_e/I (km^{-1}/(g/m^3))	.0075	.012	.019	.030	.041	.055	.074	.040	.042	
	γ_a/γ_e	.69	.39	.26	.18	.13	.102	.079	.14	.13	
MSU 2	γ_e/I	.0072	.012	.018	.027	.038	.051	.068	.036	.038	
	γ_a/γ_e	.70	.41	.27	.19	.14	.107	.083	.15	.14	
MSU 1	γ_e/I	.0064	.0097	.014	.021	.030	.040	.053	.029	.030	
	γ_a/γ_e	.72	.45	.31	.22	.16	.125	.097	.17	.16	
37 GHz	γ_e/I	.0043	.0052	.0063	.0081	.0105	.0135	.0176	.0100		
	γ_a/γ_e	.86	.69	.55	.42	.33	.26	.20	.35		
21 GHz	γ_e/I	.0027	.0026	.0026	.0027	.0029	.0031	.0035	.0030		
	γ_a/γ_e	1.	.93	.87	.81	.75	.69	.61	.77		
18 GHz	γ_e/I	.0025	.0023	.0023	.0023	.0024	.0025	.0027	.0025		
	γ_a/γ_e	1.	.98	.93	.88	.84	.79	.73	.84		
10.69 GHz	γ_e/I	.0020	.0017	.0016	.0015	.0015	.0015	.0015			
	γ_a/γ_e	1.	1.	1.	.99	.97	.96	.94			
6.6 GHz	γ_e/I	.0018	.0015	.0013	.0013	.0012	.0012	.0012			
	γ_a/γ_e	1.	1.	1.	1.	1.	1.	1.			

Measurements of brightness temperature anomalies in MSU 1 and 2, and scenarios which explain them in terms of amounts (Q_i) and area coverages (σ_i), of different cloud distributions (i) as in Table 7. (Shown in parentheses, ΔT_{12} is a saturation value, 44 K.)

				$\Delta T_{3i}/Q$																
				.0		−.03		−1.8		−0.3		−0.7		−4.1					
			$(\Delta T_{1i}/Q, \Delta T_{2i}/Q)$	(30,0.8)		((44),−0.25)		(43,−24)		(10,−1.6)		(12,−3.6)		(−10,−32)					
Measurement	ΔT_1 (K)	ΔT_2 (K) ($\Delta T_1/\Delta T_2$)		Q_1 (mm)	σ_1	Q_2 (mm)	σ_2	Q_3 (mm)	σ_3	Q_6 (mm)	σ_6	Q_7 (mm)	σ_7	Q_8 (mm)	σ_8	Q (mm)	ΔT_3 (K)	$\frac{\Delta T_1}{Q}$	$\frac{\Delta T_2}{Q}$ (K/mm)
A	26.9	−3.4 (−7.9)				6.	0.35	1.21	0.05	1.48	0.6					3.0	−0.4	8.8	−1.1
						4.	0.35	1.41	0.05	1.41	0.6					2.3	−0.4	11.6	−1.5
						6.	0.3	1.	0.05	2.04	0.6	1.17	0.05			3.1	−0.6	8.7	−1.1
B	21.8	−3.3 (−6.6)		0.1	0.1	6.	0.2	0.28	0.2	2.05	0.5					2.3	−0.4	9.5	−1.4
				0.2	0.2	6.	0.3	0.99	0.1	0.78	0.4					2.3	−0.3	9.5	−1.4
				0.2	0.2	6.	0.3	0.50	0.2	1.04	0.3					2.3	−0.3	9.5	−1.4
						6.	0.2	0.3	0.05	1.27	0.6	2.63	0.15			2.4	−0.6	9.2	−1.4
						6.	0.2	0.3	0.05	1.52	0.5	1.58	0.25			2.4	−0.6	9.2	−1.4
C	14.5	−1.7 (−8.5)				6.	0.2	0.3	0.05	0.57	0.6	0.92	0.15			1.7	−0.3	8.6	−1.0
						6.	0.2	0.3	0.05	0.68	0.5	0.55	0.25			1.7	−0.3	8.4	−1.0
D	12.8	−2.7 (−4.7)				6.	0.2	0.02	0.2	0.86	0.5			0.5	0.1	1.7	−0.4	13.	−2.0
						6.	0.2	0.05	0.1	0.72	0.6			0.5	0.1	1.7	−0.4	13.	−2.0
E	9.2	−1.4 (−6.6)		1.0	0.1			0.3	0.05	0.78	0.5	0.39	0.35			0.6	−0.2	14.	−2.2
				1.0	0.1			0.3	0.05	0.65	0.6	0.55	0.25			0.6	−0.2	14.	−2.2
F	14.4	.0		0.37	0.9	10.7	0.1									1.4	−.03	10.2	.0
				0.31	0.85	5.5	0.15									1.1	−.02	13.2	.0
				0.23	0.8	3.0	0.2									0.8	−.02	18.5	.0
G	8.0	.0		0.20	0.95	12.4	0.05									0.8	−.02	9.9	.0
				0.13	0.9	3.8	0.1									0.5	−.01	16.	.0
	Measurements					Trial values												Derived quantities	

Fig. 1. 5 July, daytime. Streamlines at the surface (bottom) and at 700 hPa (top). Isotachs are shown as dotted lines. The coast of the Bay of Bengal is shown as a dashed line. Shaded areas in the bottom map represent high clouds seen in the visible image from DMSP in Fig. 2.
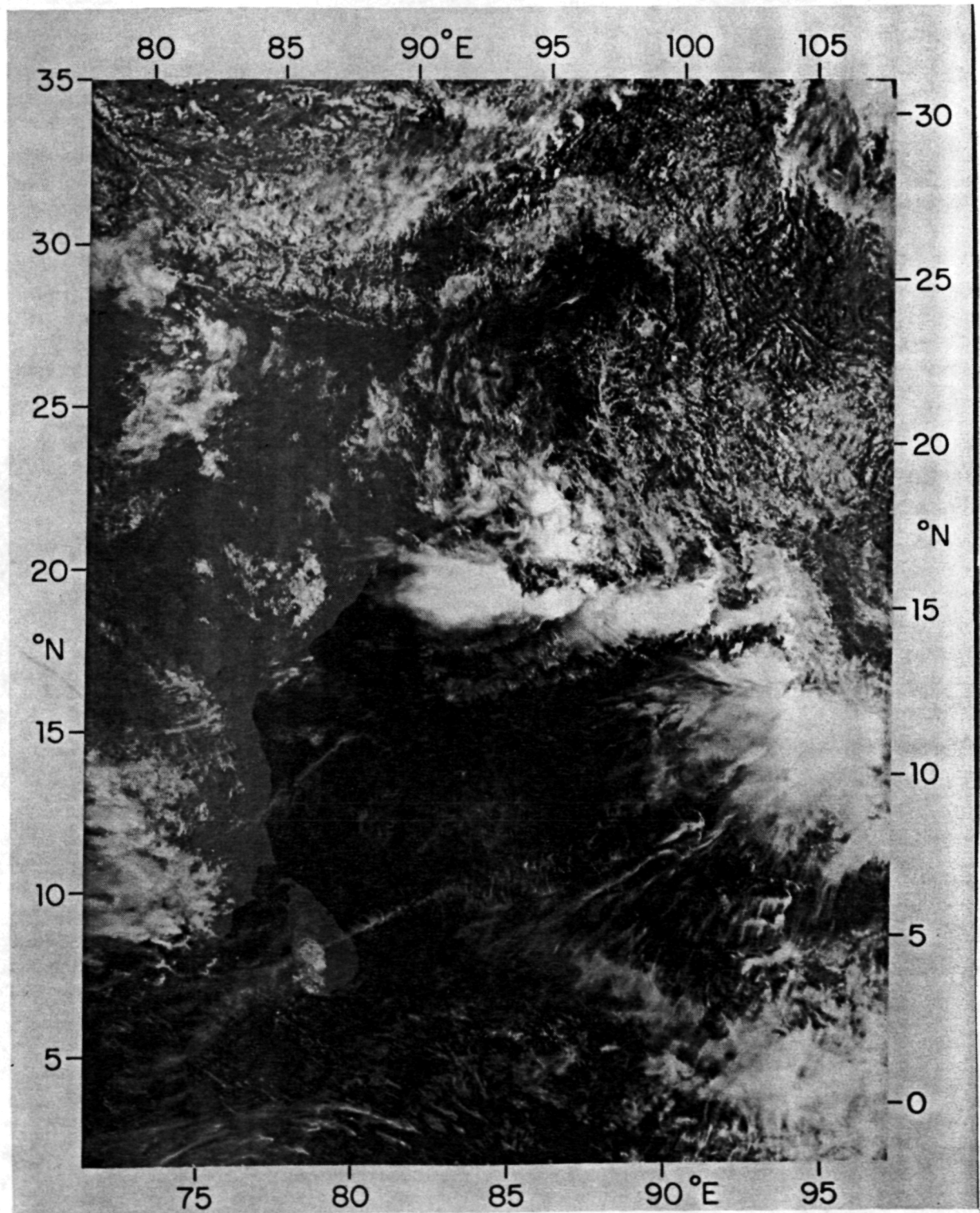
FIG. 2. 5 July, 0422 GMT. Visible image from DMSP satellite F4.
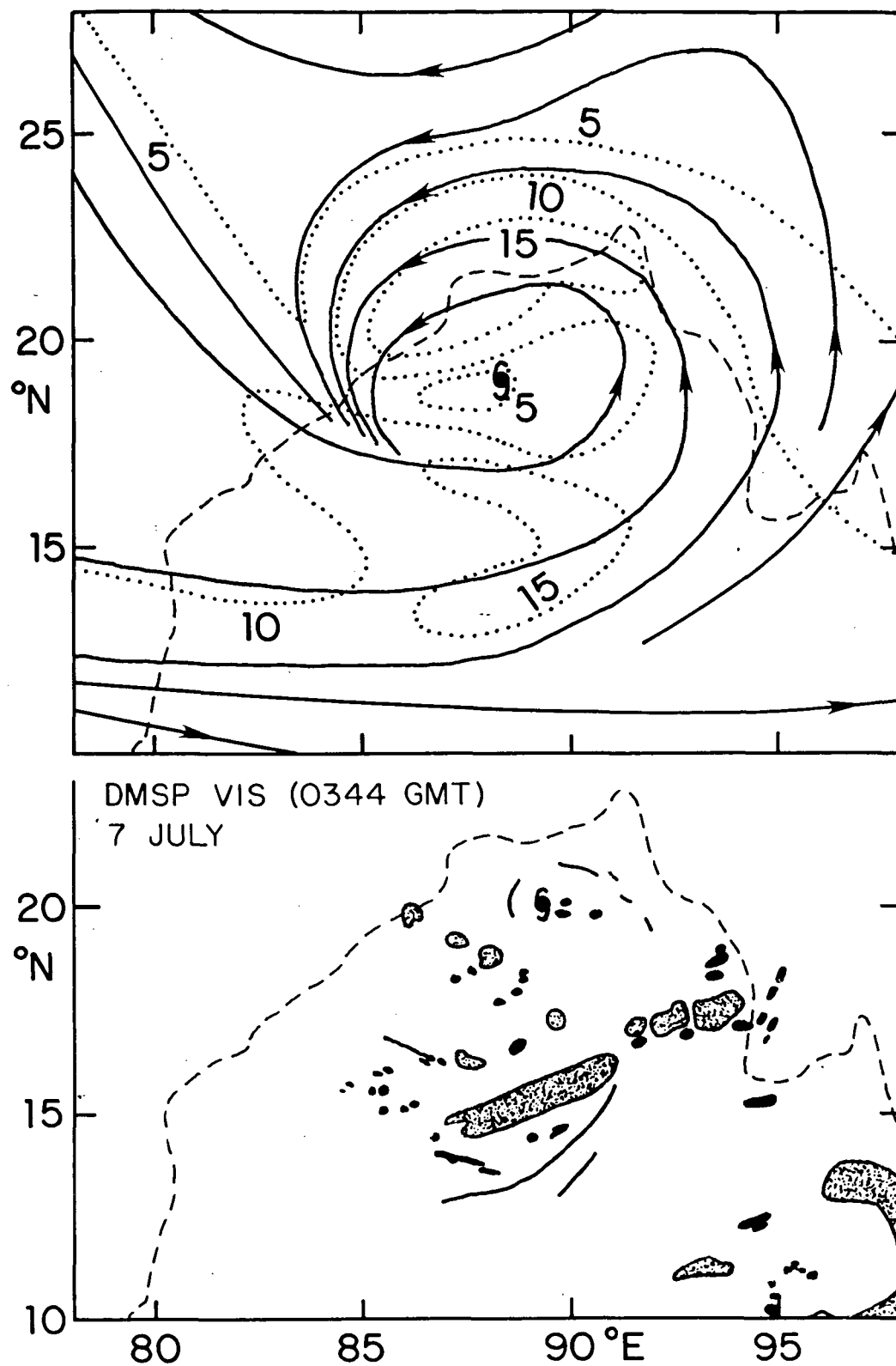
Fig. 3.   7 July, daytime.   High clouds from DMSP (bottom,
as in Fig. 1),   and streamlines and isotachs at 700 hPa
(top).   No streamlines are shown in the bottom map —
only the center of circulation at the surface, using a
cyclone symbol.   Further details, including the DMSP image,
are given in Warner (1984a).
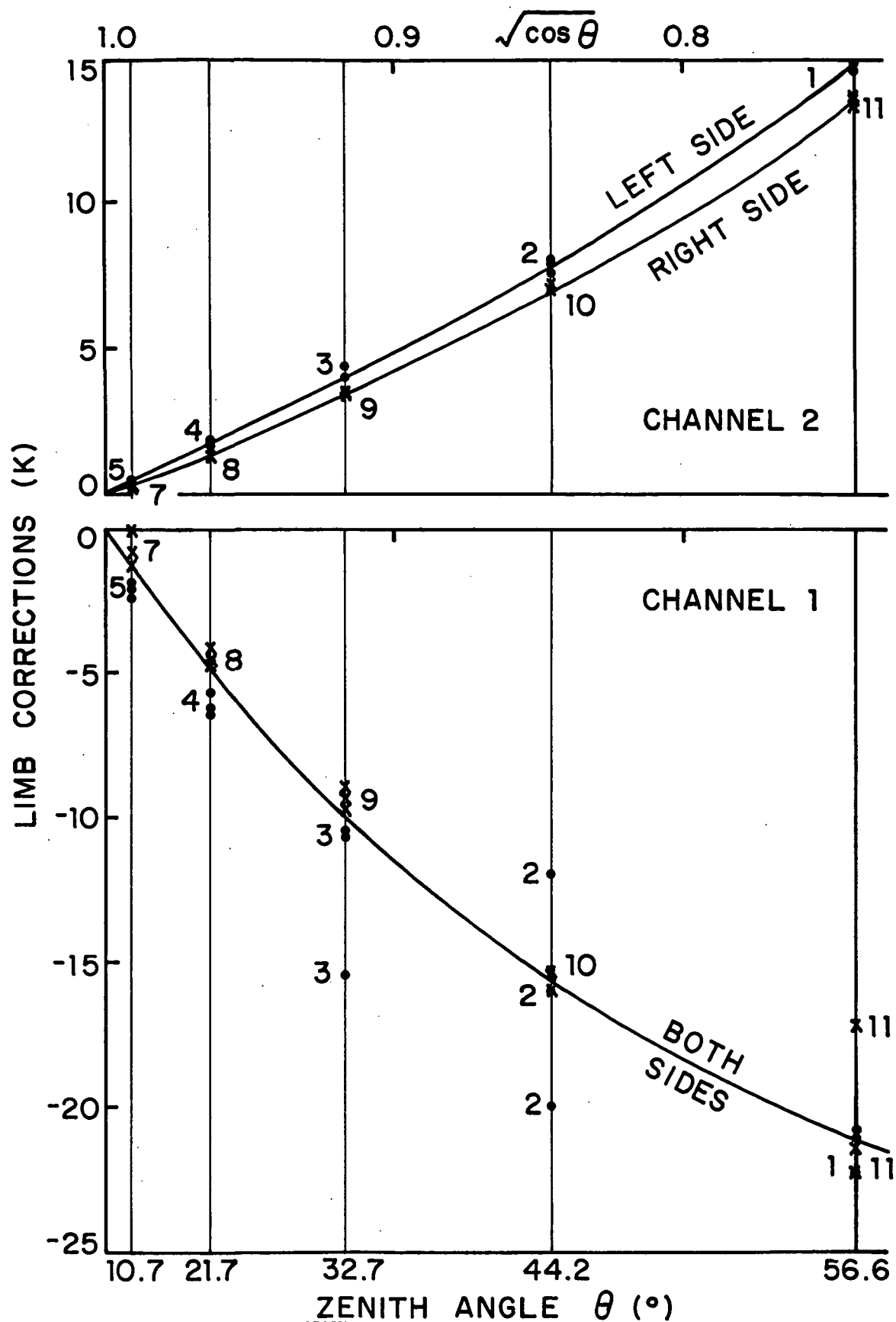
FIG. 4. Limb corrections for MSU Channels 1 and 2 plotted as a function of zenith angle. Scan spots to the left (right) side of the track are shown by dots (crosses).
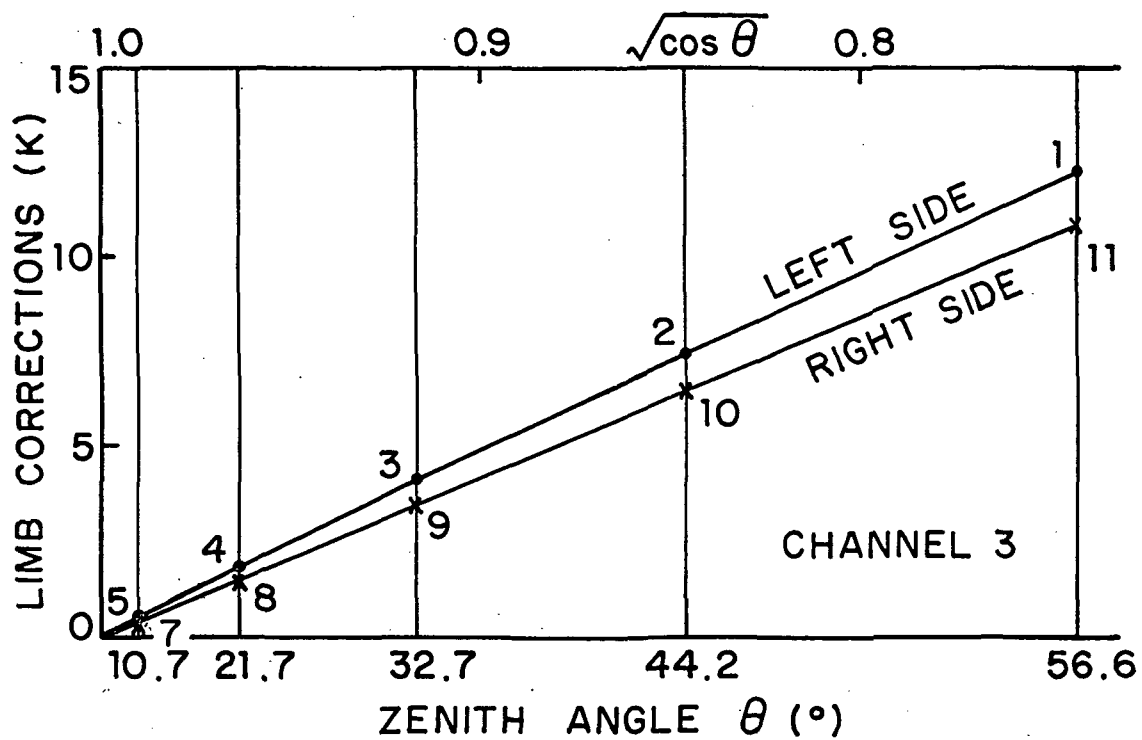
FIG. 5. Limb corrections for MSU Channel 3, as in Fig. 4.
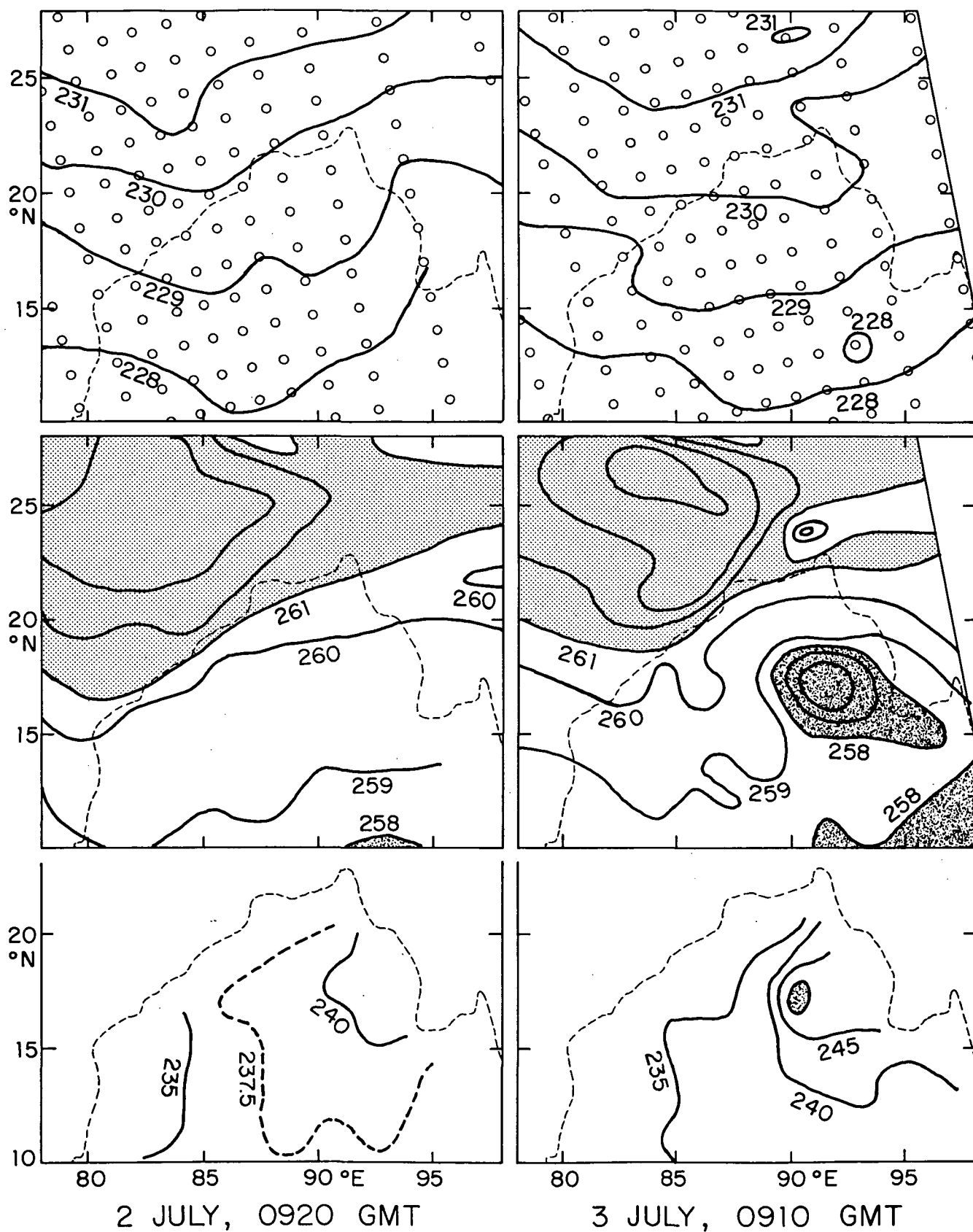
FIG. 6. 2 July and 3 July, daytime. Brightness temperatures (K) in MSU Channel 1 (bottom), 2 (middle) and 3 (top). The coast of the Bay of Bengal is shown by a short-dashed line. Scan spots are shown in the top panels.

4 JULY, 0859 GMT

4 JULY, 2134 GMT
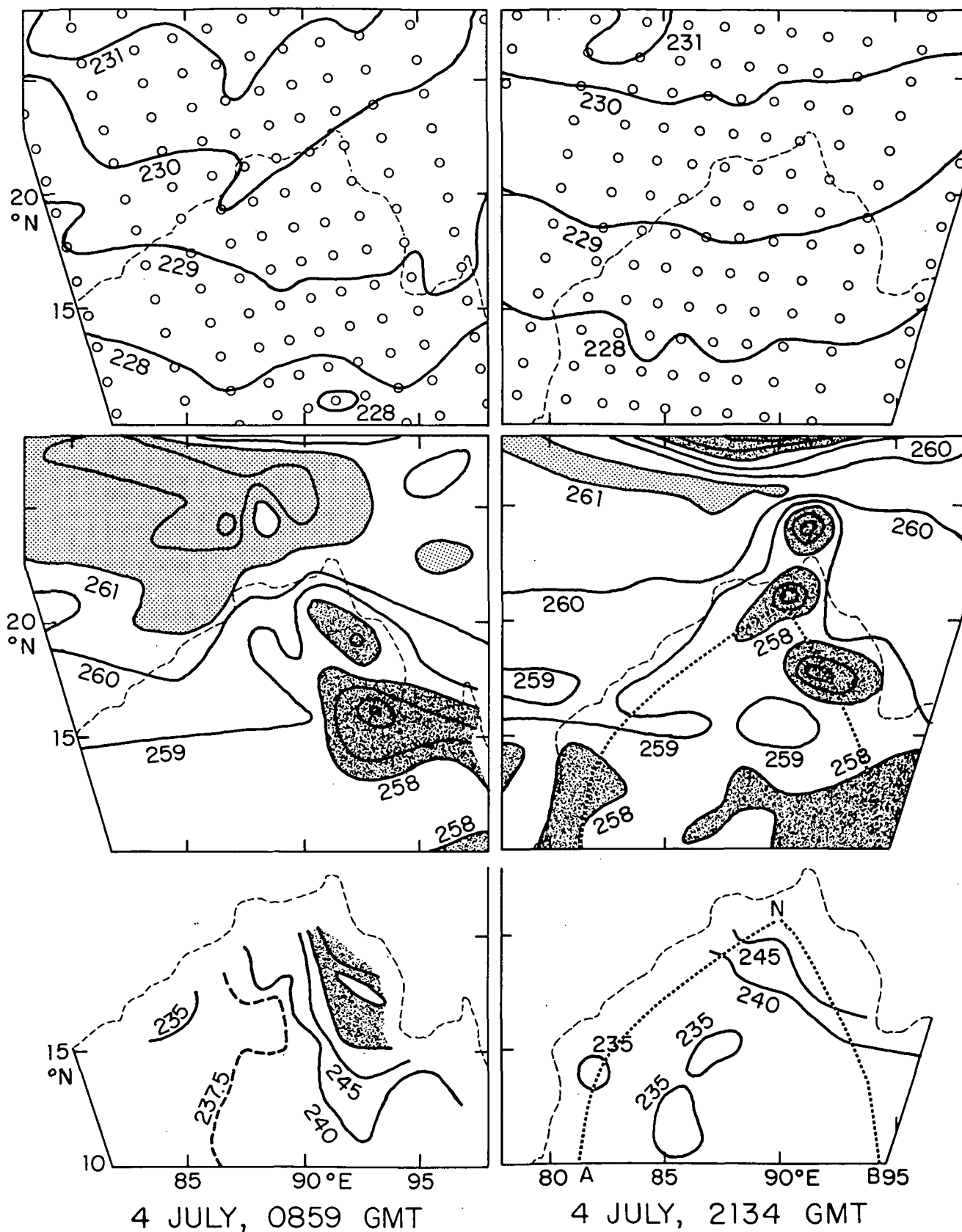
FIG. 7. 4 July, daytime and night-time. Brightness temperatures from MSU as in Fig. 6. At right, a thick-dashed line ANB in the lower two maps indicates a section line along which temperatures are displayed in Fig. 33.

5 JULY, 0849 GMT   5 JULY, 2123 GMT
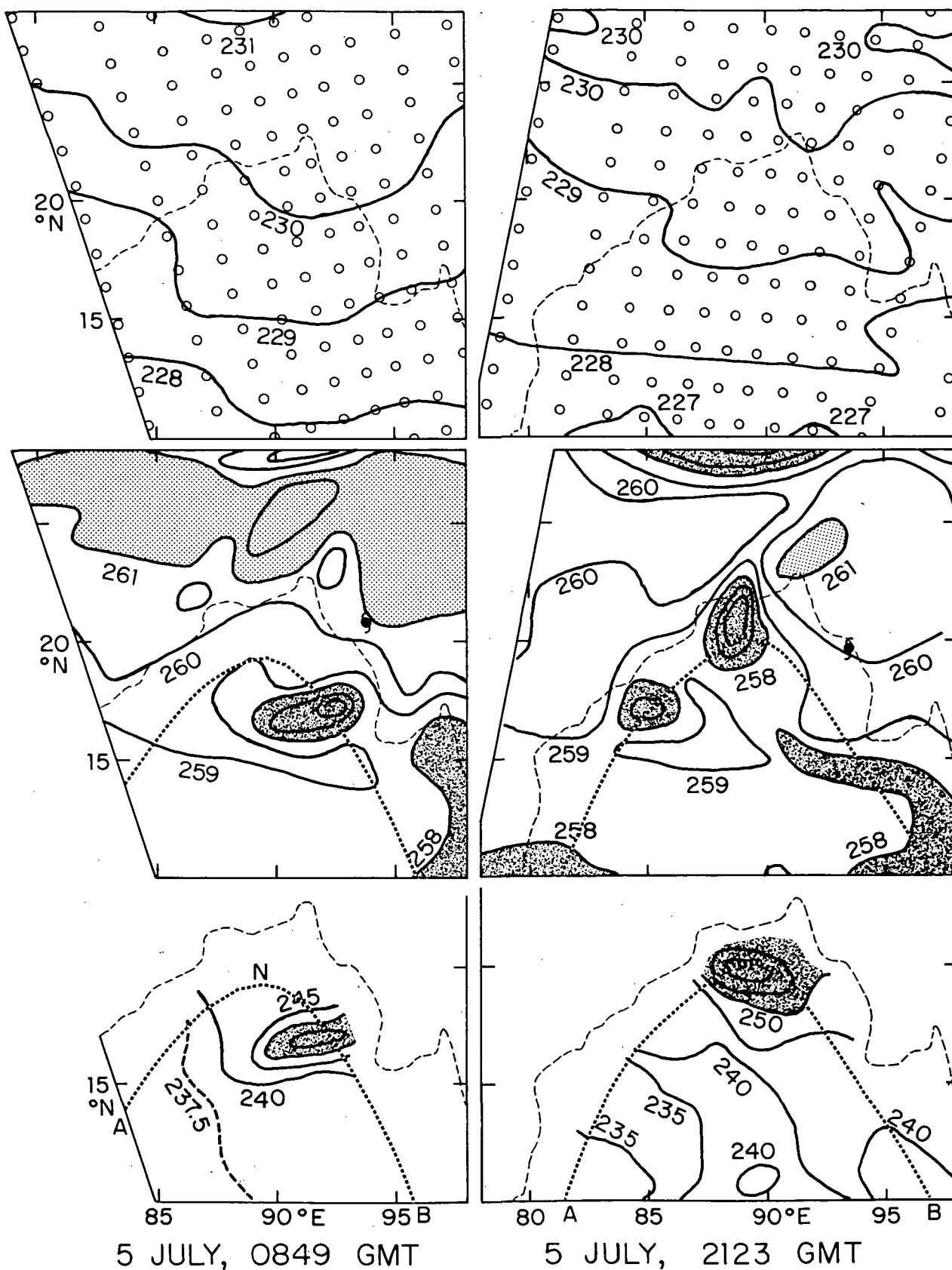
FIG. 8. 5 July, daytime and night-time. Brightness temperatures from MSU as in Fig. 6. Temperatures along thick-dashed lines ANB at left (right) are displayed in Fig. 34 (35). The center of circulation at 700 hPa is shown by a cyclone symbol.
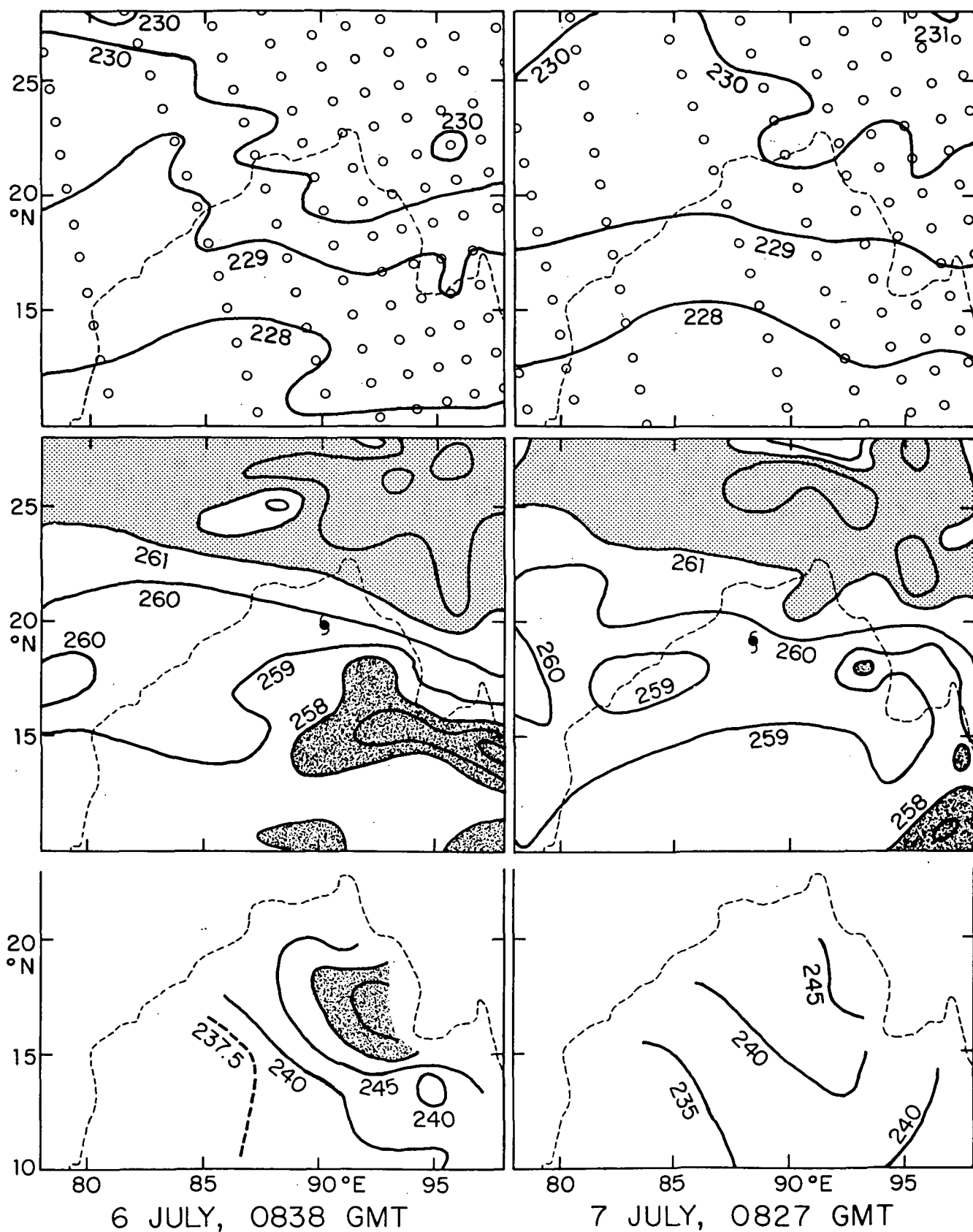
FIG. 9. 6 July and 7 July, daytime. Brightness temperatures
from MSU as in Fig. 6. The center of circulation at 700 hPa
is shown by a cyclone symbol.
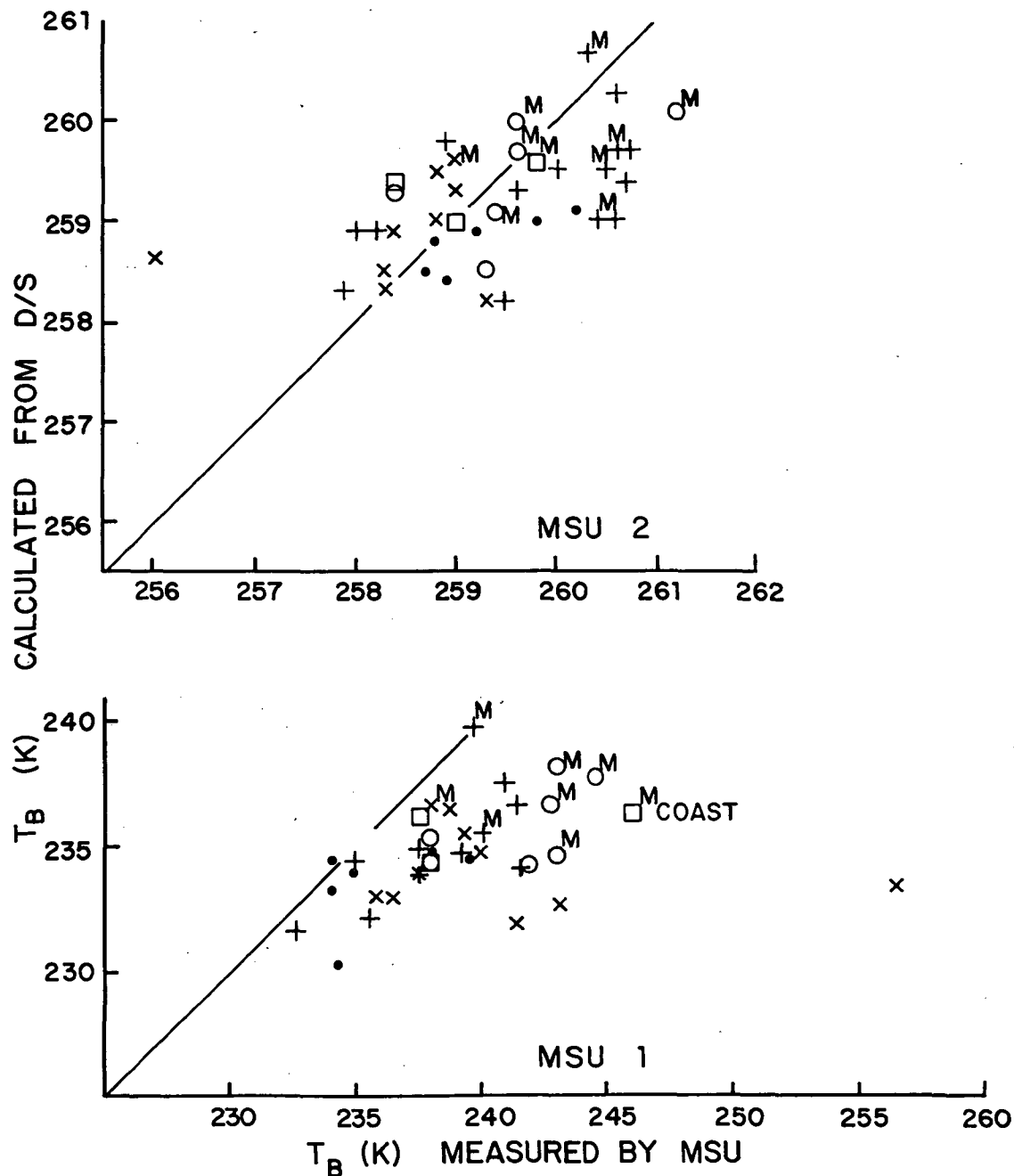
FIG. 10. Brightness temperatures calculated from dropwindsondes plotted against temperatures measured from MSU, in Channel 1 (bottom) and Channel 2 (top). Symbols and corresponding dates are as follows: •, 3 July. X, 5 July. ☐, 6 July. O, 7 July. +, 8 July. The letter M refers to a moist sounding, with water vapor ≥ 68 mm. The word COAST indicates a measurement from MSU 1 that probably was affected by radiation from land. Lines at 45° refer to equality of measurement and calculation.
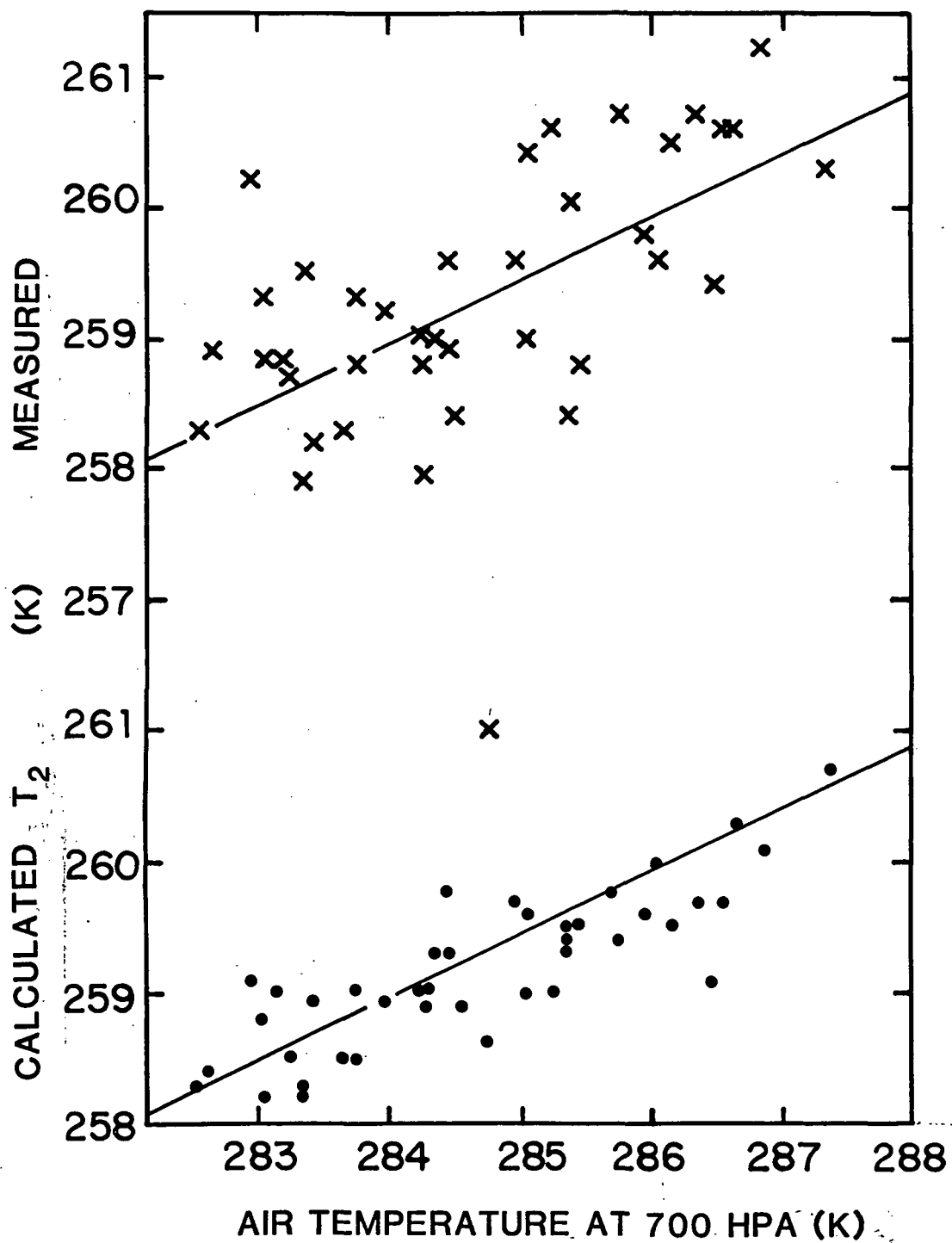
FIG. 11. Temperatures at 700 hPa measured by dropwindsondes
compared with brightness temperatures in MSU 2, both
calculated (bottom, dots) and measured (top, crosses).
The same in both plots, a line is drawn by eye to fit
these results (see Eq. (3)).
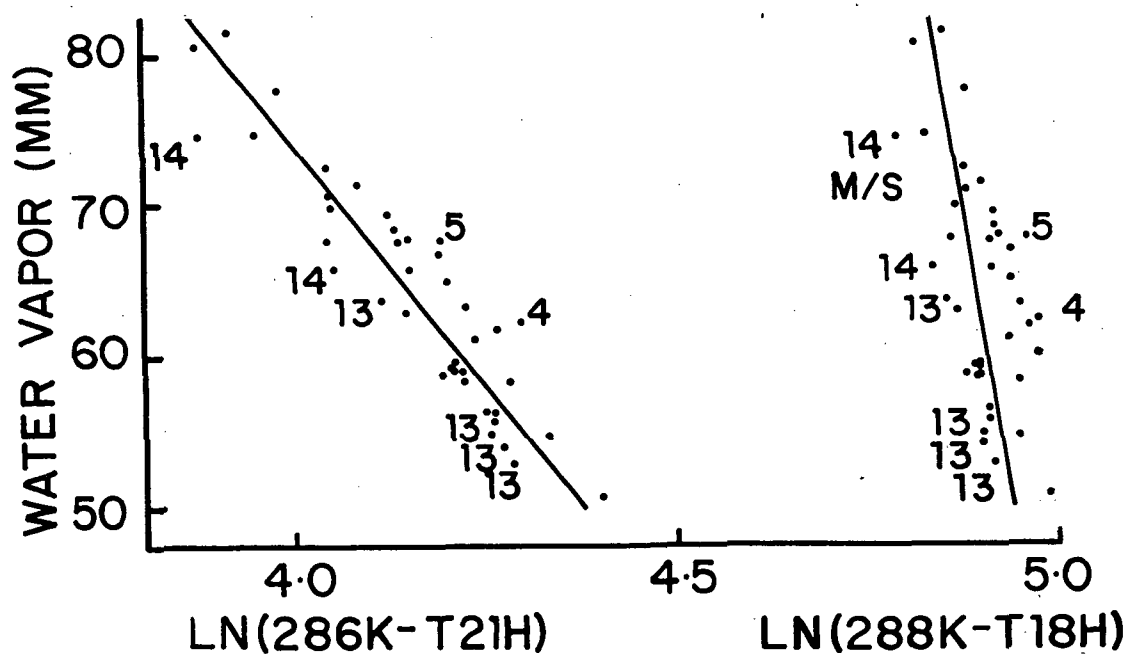
FIG. 12.   Water vapor measured from dropwindsondes
plotted against calculated parameters of SMMR:
$\ln(286\ K - T_{21H})$ and $\ln(288\ K - T_{18H})$.   Integer
labels are surface wind speeds (m/s) estimated
from the dropwindsondes.
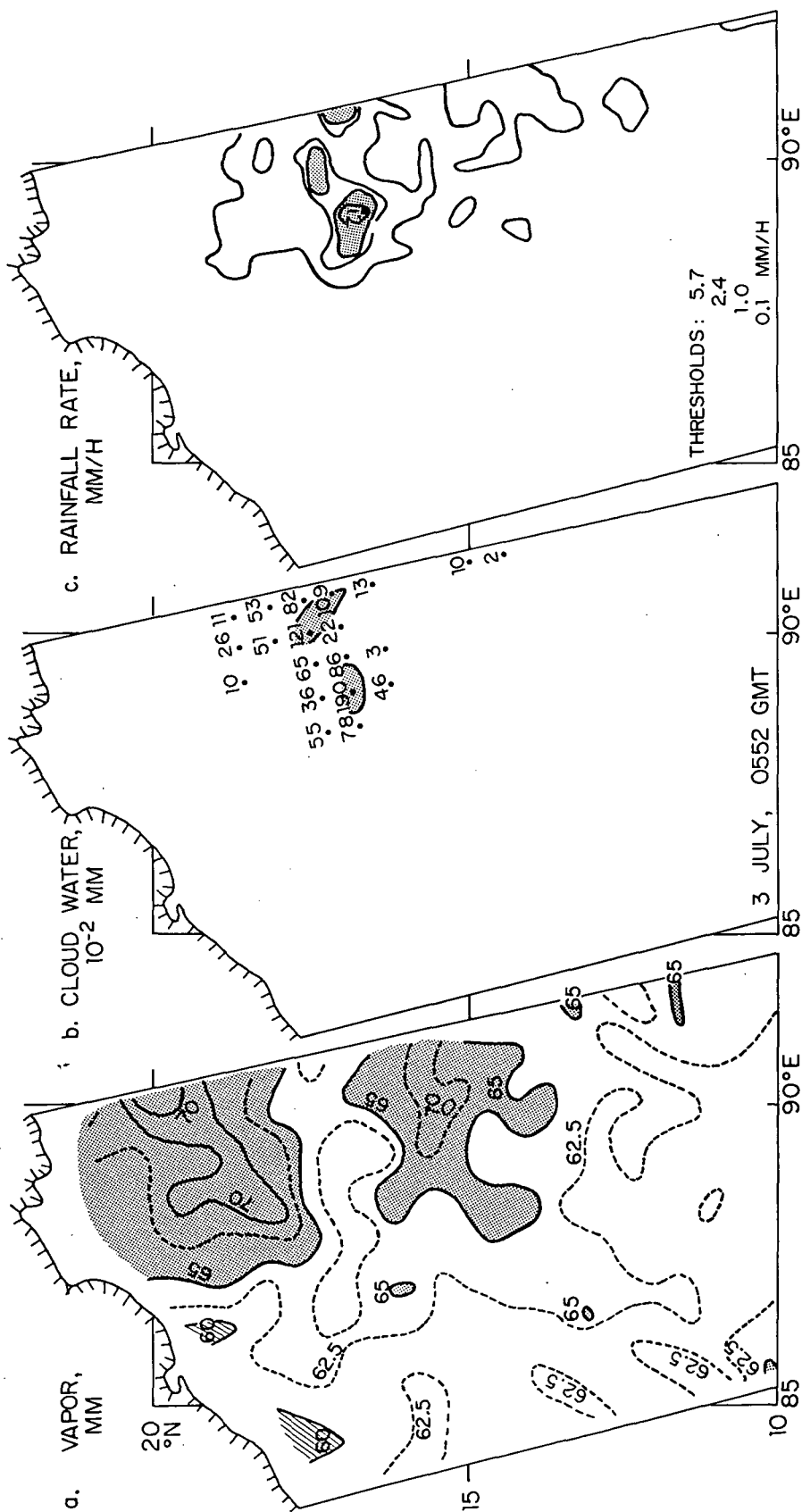
FIG. 13. 3 July, 0552 GMT. SMMR results from Nimbus-7.

a (left): Water vapor (mm), contoured every 2.5 mm from data on a 60 km grid.
b (middle): Cloud water (10⁻² mm).
c (right): Rainfall rate (mm/h), contoured at 5.7, 2.4, 1.2 and 0.1 mm/h from data on a 30 km grid.
Peak values are shown.

In each panel, the coastline and islands are indicated.
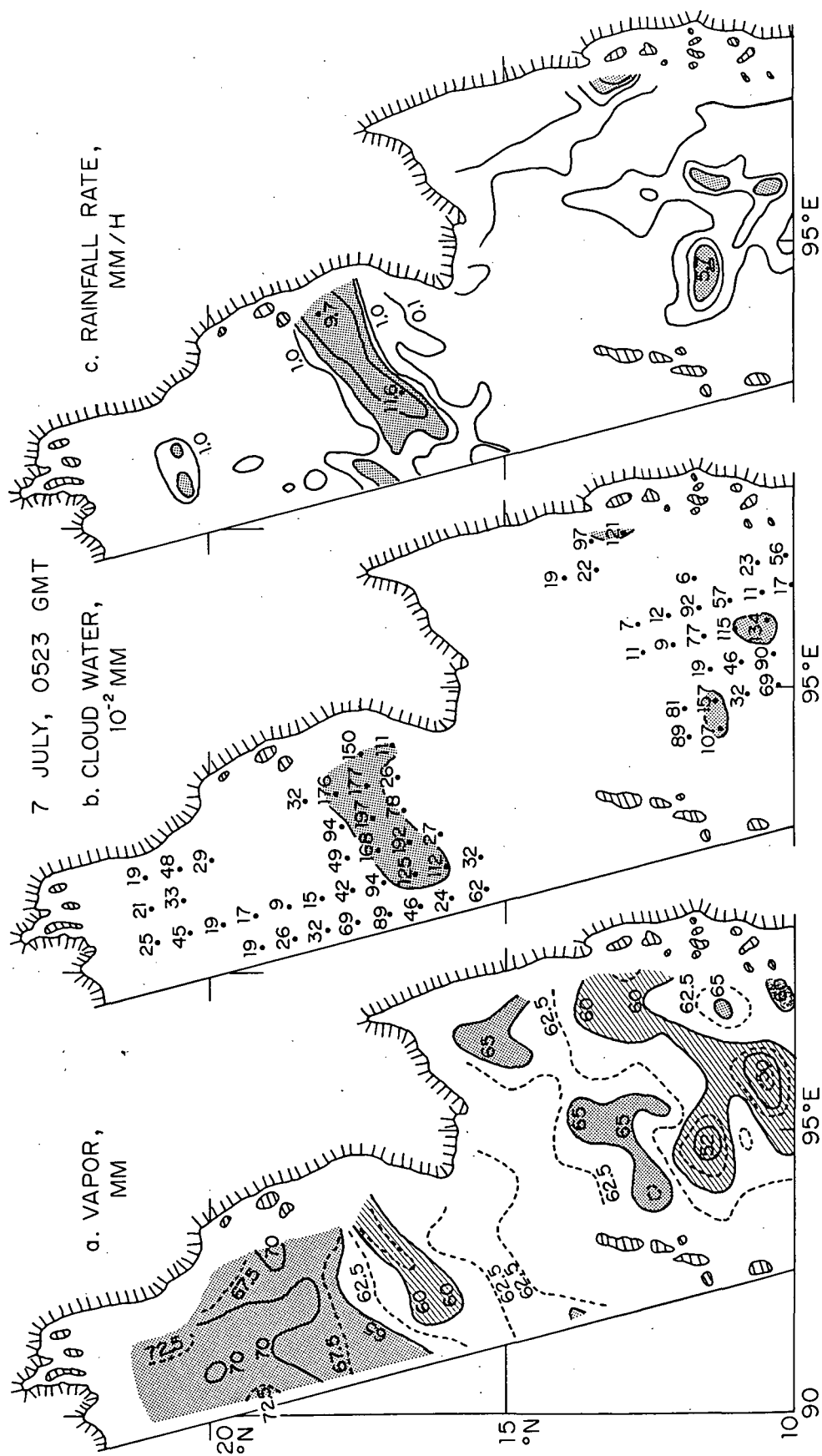
FIG. 14. 7 July, 0523 GMT. SMMR results from Nimbus-7, as in Fig. 13.
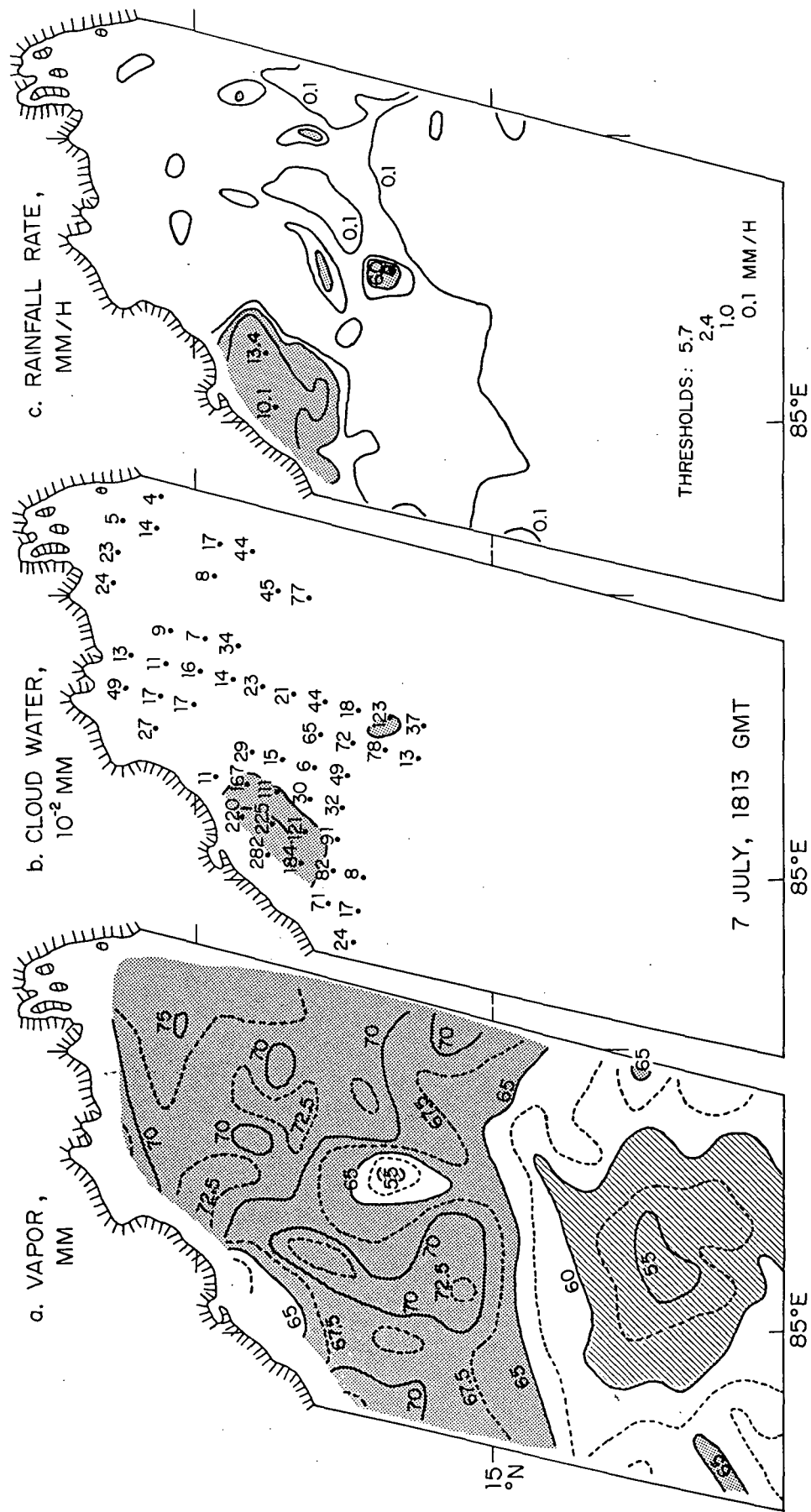
FIG. 15. 7 July, 1813 GMT. SMMR results from Nimbus-7, as in Fig. 13.
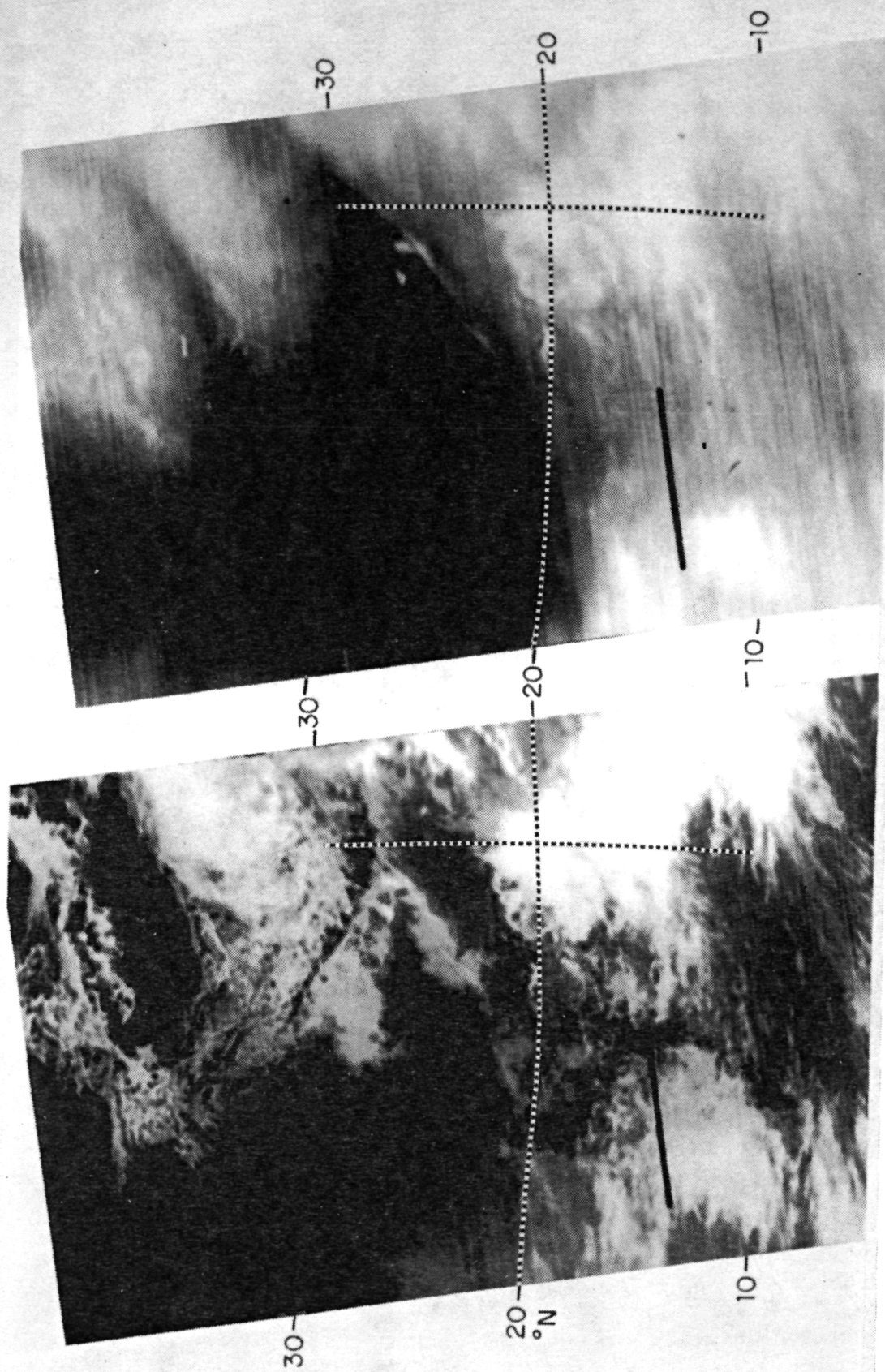
FIG. 16. 4 July, 0613 GMT. THIR data from Nimbus-7 (ascending pass).
Infrared (11.5 μm, left) and water vapor (6.7 μm, right) images.
The 20°N line is shown, and the 90°E meridian between 10 and 30°N.
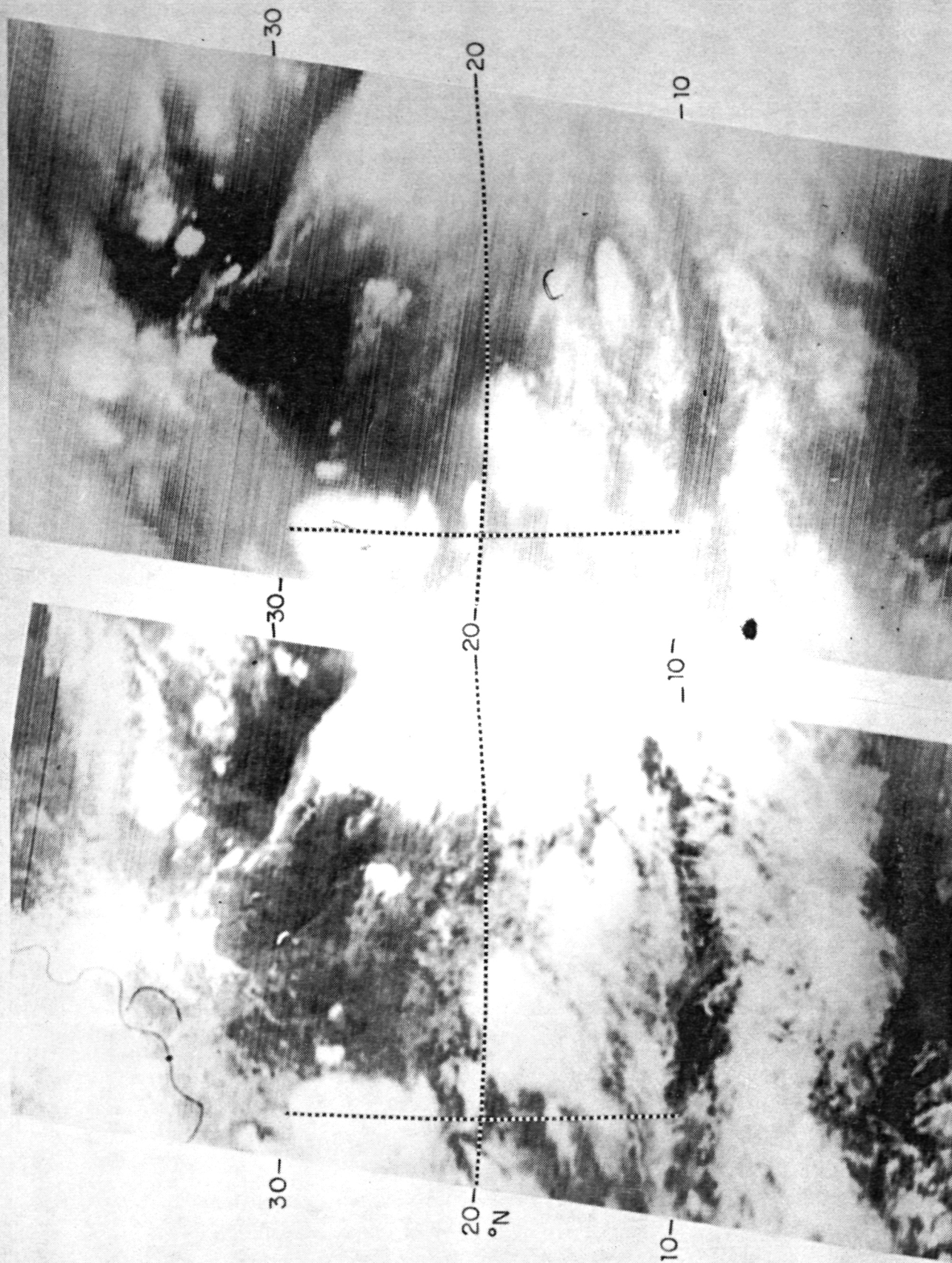
FIG. 17. 4 July, 1719 GMT. THIR data from Nimbus-7 (descending pass). Infrared (left) and water vapor (right) images as in Fig. 16.
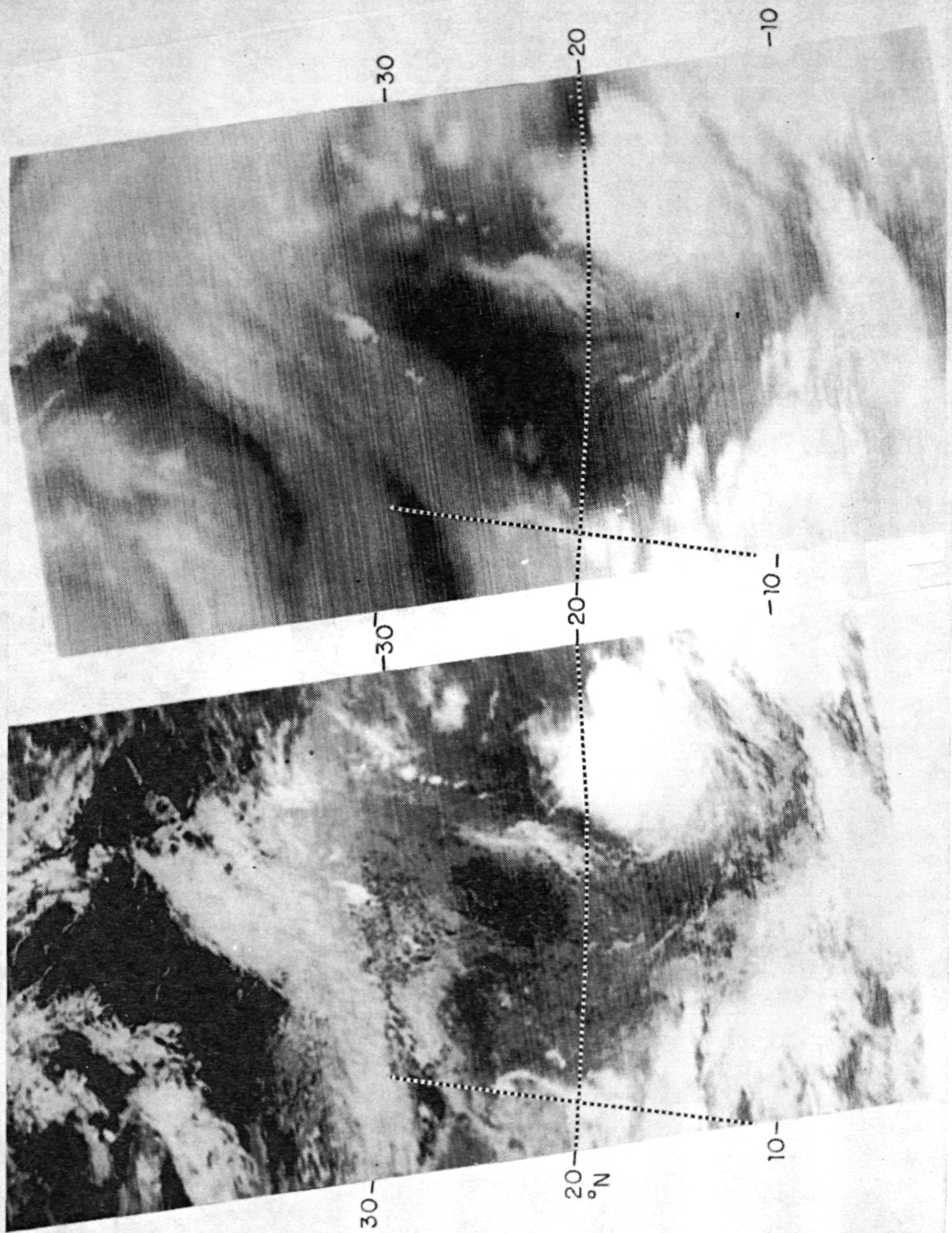
FIG. 18. 5 July, 0447 GMT. THIR data from Nimbus-7 (ascending pass). Infrared (left) and water vapor (right) images as in Fig. 16.
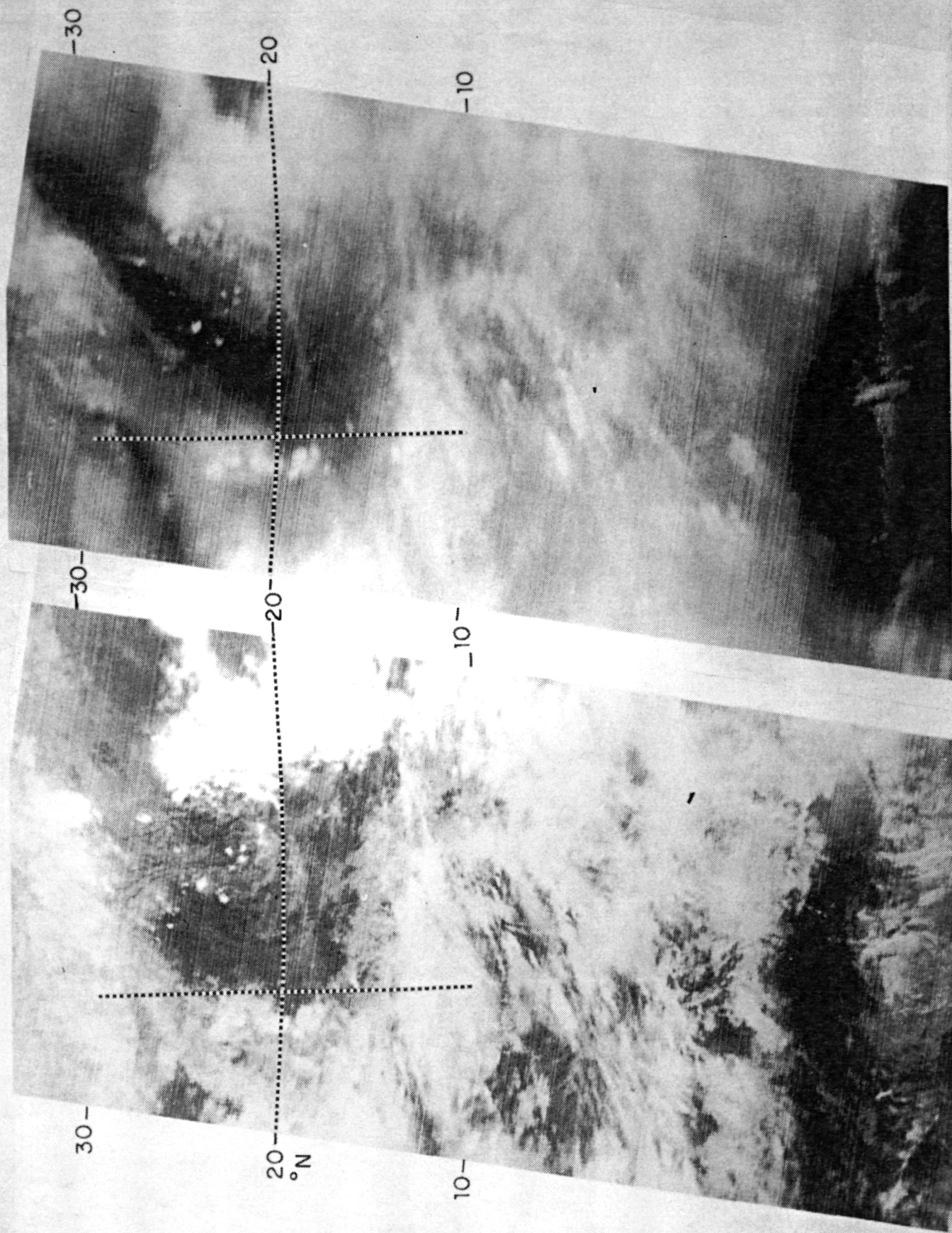
FIG. 19. 5 July, 1737 GMT. THIR data from Nimbus-7 (descending pass). Infrared (left) and water vapor (right) images as in Fig. 16.
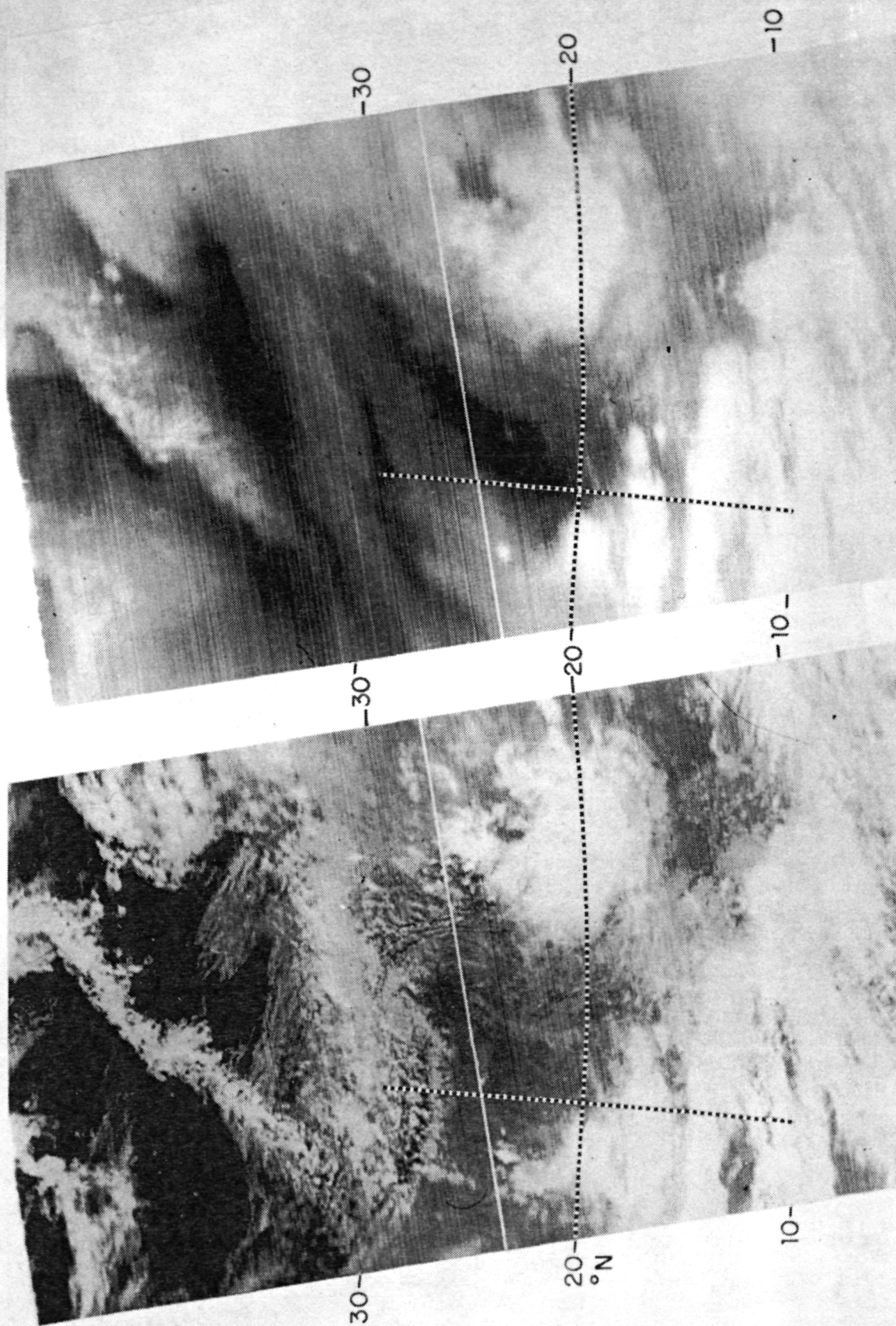
FIG. 20. 6 July, 0506 GMT. THIR data from Nimbus-7 (ascending pass). Infrared (left) and water vapor (right) images as in Fig. 16.
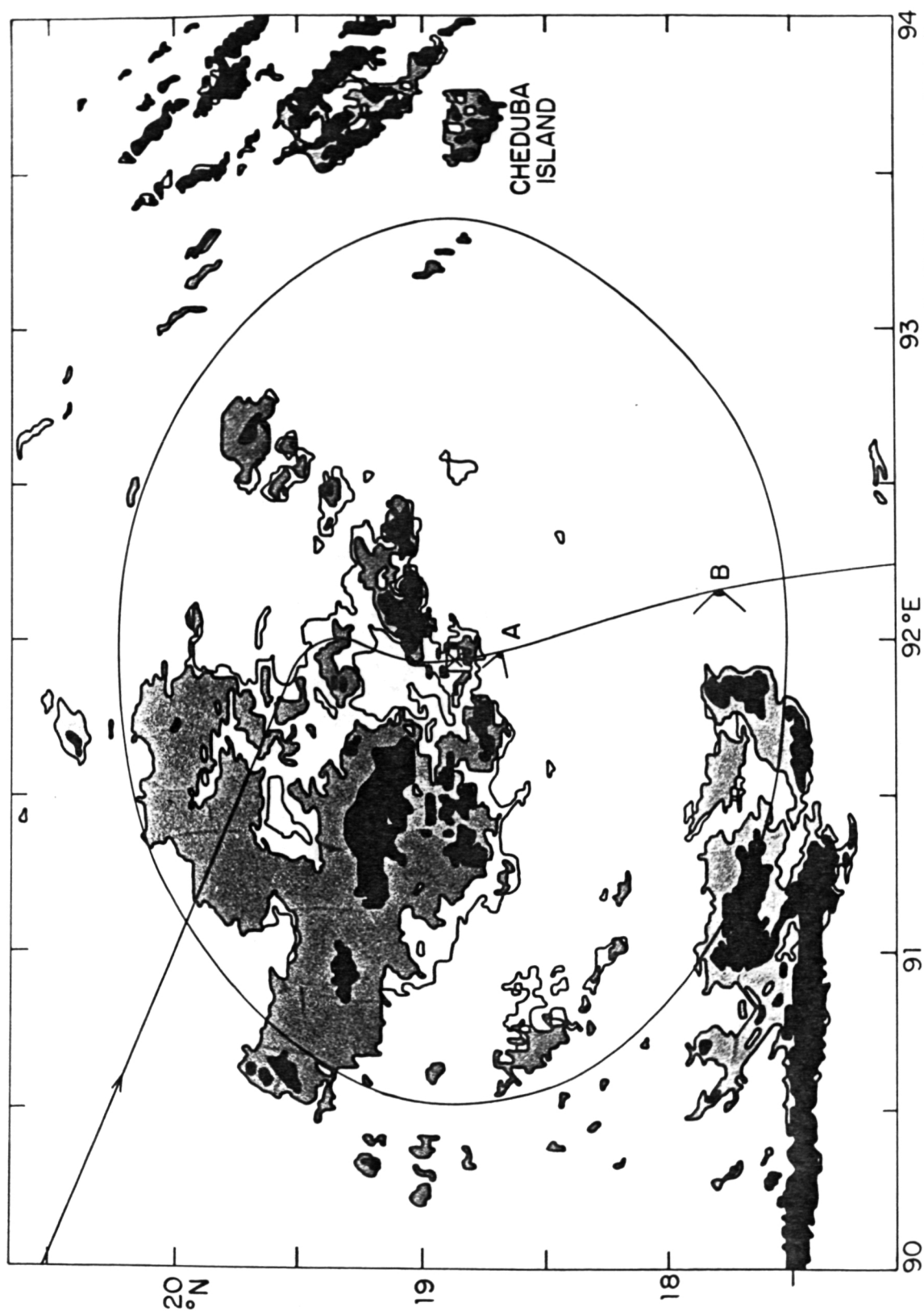
FIG. 21. Map of radar echoes recorded aboard the WP-3D at 91.93°E, 18.77°N, 483 hPa, 0356:24 to :41 GMT. Intensity thresholds are at 25, 30 and 35 dBZ. Along the track of the aircraft, 'A' refers to the photograph in Fig. 22, and 'B' to that in Fig. 23. A cross marks the position of the aircraft at map time, and a ring at range 150 km is added.

FIG. 22. Photograph taken at 91.98°E, 18.58°N, 483 hPa, 0358:40 GMT looking west-northwestward from location A in Fig. 21.
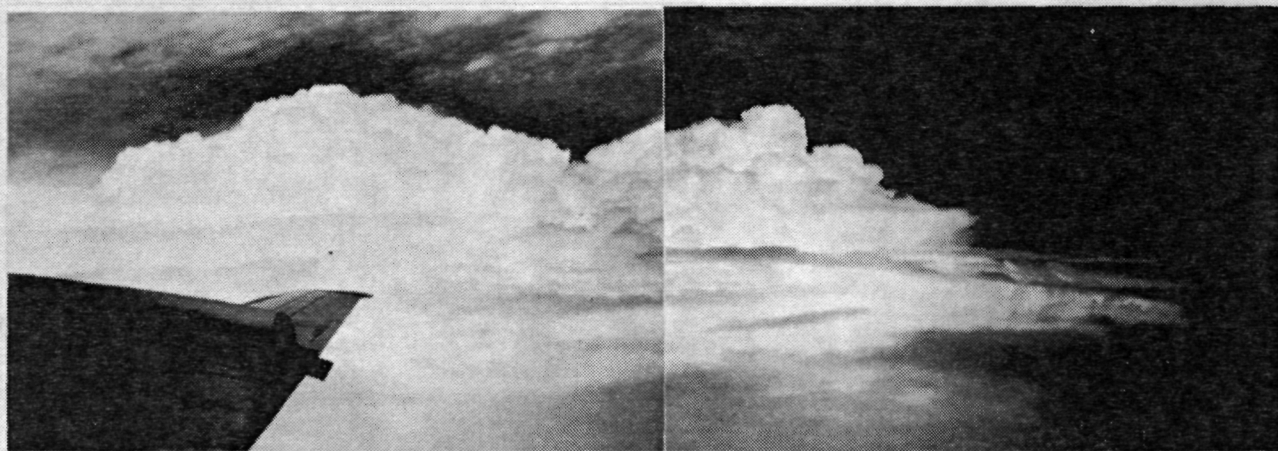
FIG. 23. Panorama of photographs taken at 92.19°E, 17.68°N, 483 hPa, 0409:20 GMT looking westward from location B in Fig. 21.
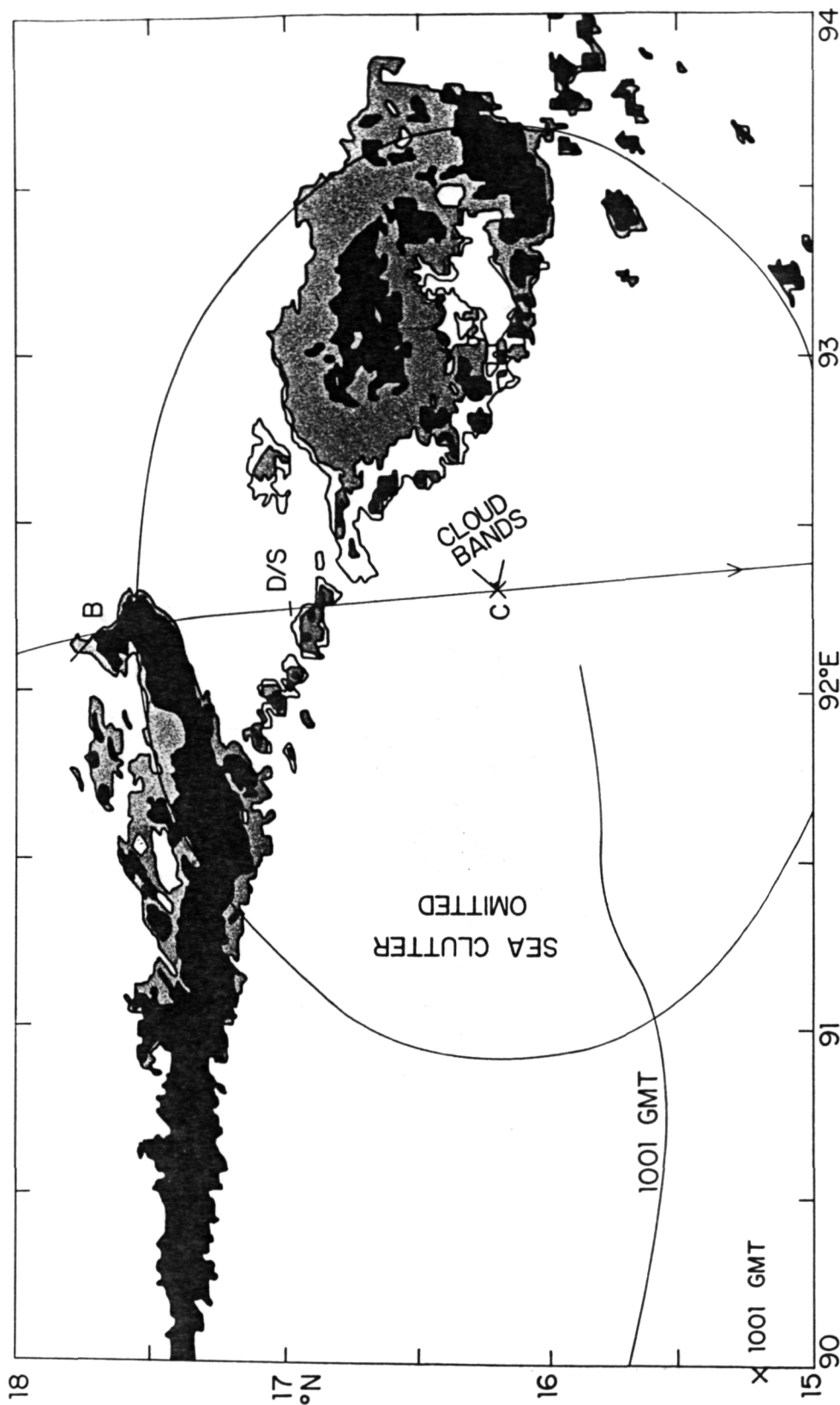
FIG. 24. Map of radar echoes recorded aboard the WP-3D at 92.31°E, 16.19°N, 483 hPa, 0425:30 to :46 GMT. Intensity thresholds are at 25, 30 and 35 dBz. Along the track of the aircraft, 'B' refers to the photograph in Fig. 23, 'D/S' to the dropwindsonde measurements shown in Fig. 25, and 'C' to the photograph in Fig. 26. Crosses show the locations of the aircraft at map time, and at 1001 GMT (Fig. 28). Also shown is the position of the echo line at 1001 GMT, abstracted from Fig. 28. The ring is at range 150 km from the aircraft. A crescent of echoes extending westward from the aircraft beyond range 80 km, attributed to sea clutter, has been omitted.
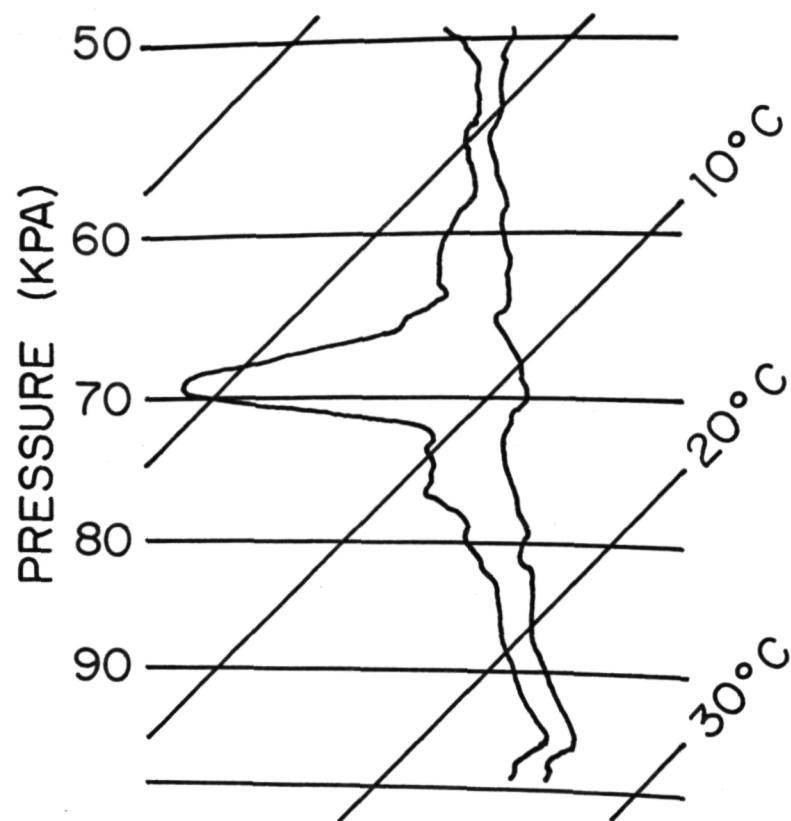
FIG. 25. Tephigram from dropwindsonde released at
92.24°E, 16.98°N, 483 hPa, 0416:36 GMT, at "D/S"
in Fig. 24.

FIG. 26. Photograph taken at 92.30°E, 16.20°N,
483 hPa, 0425:35 GMT looking east-northeastward
from location C in Fig. 24.
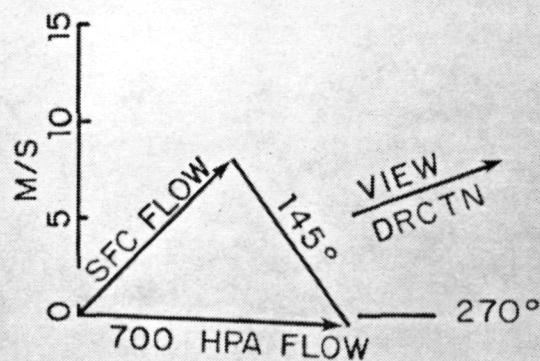
FIG. 27. Hodograph from Fig. 1 showing flows
at the surface and at 700 hPa, the shear between
these levels, and the direction of view of the
photograph in Fig. 26.
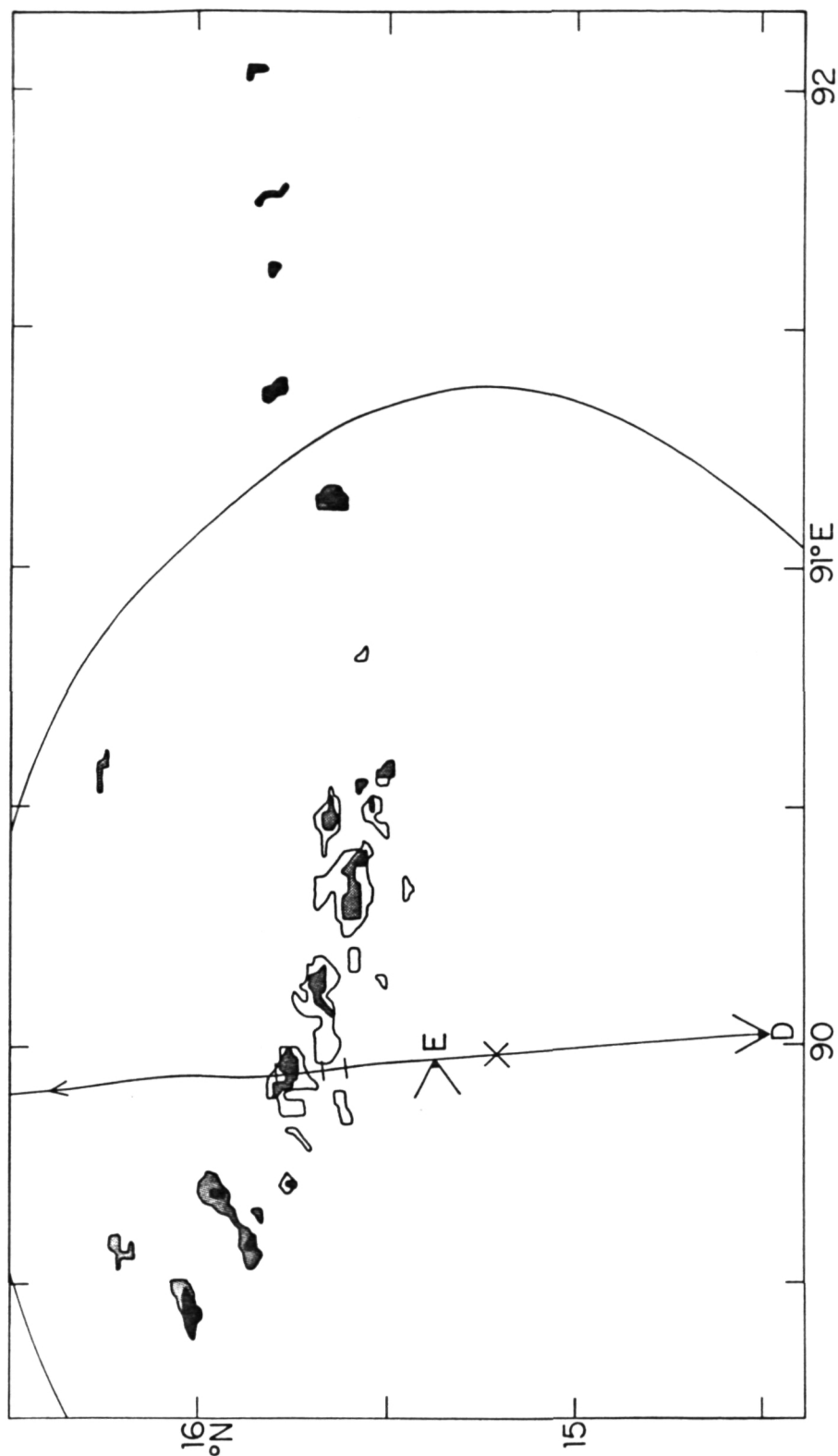
FIG. 28. Map of radar echoes recorded aboard the WP-3D at 89.98°E, 15.21°N, 327 hPa, 1001:14 to 30 GMT. Intensity thresholds are at 25, 30 and 35 dBZ. Along the track of the aircraft, 'D' refers to the photograph in Fig. 29, and 'E' to that in Fig. 30. Three short lines drawn across the aircraft track locate intense convective updraft cores detailed in Table 6; the middle one reached 15.7 m/s. The aircraft position is shown by a cross. Arcs are at range 150 km.
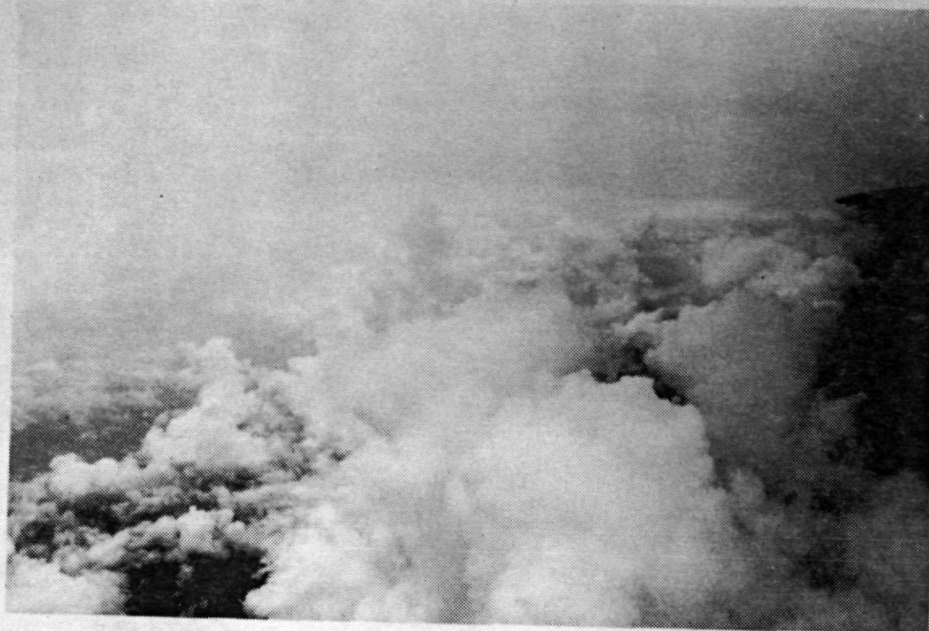
FIG. 30. Photograph taken at 89.96°E, 15.37°N,
327 hPa, 1003:10 GMT looking westward from
location E in Fig. 28.
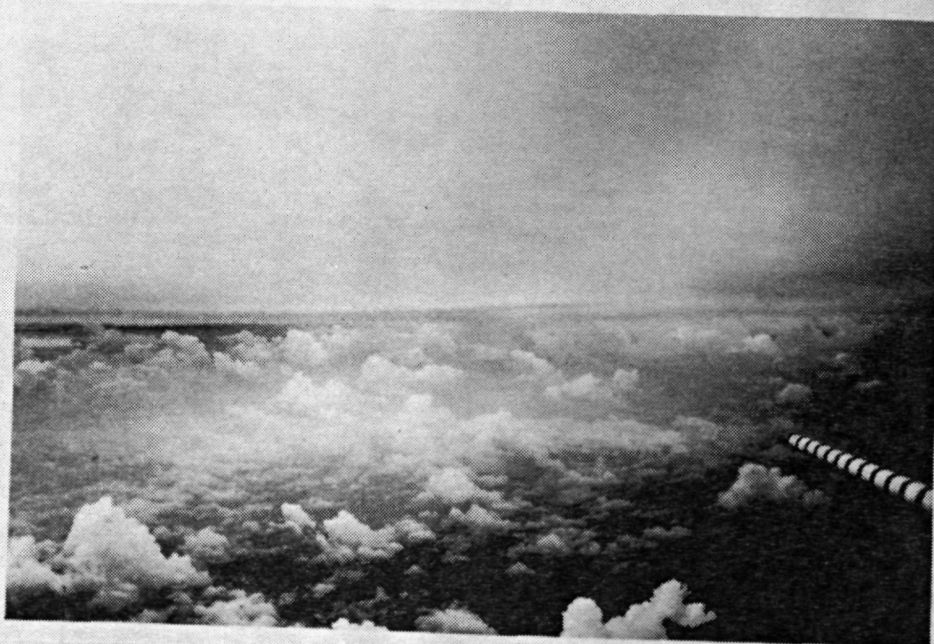
FIG. 29. Photograph taken at 90.02°E, 14.48°N,
329 hPa, 0953:22 GMT looking northward from
location D in Fig. 28.
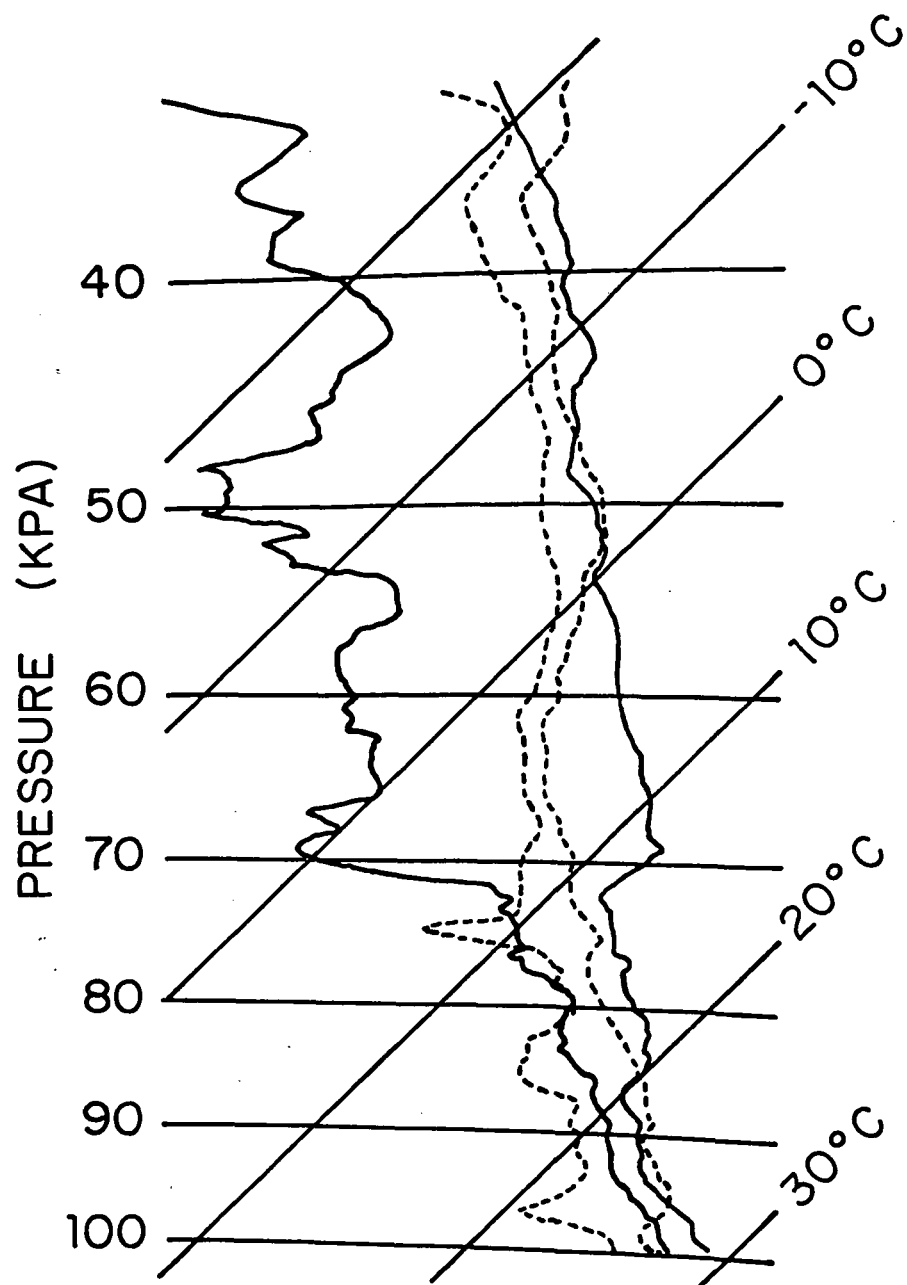
FIG. 31. Tephigrams from dropwindsondes released at 90.01°E, 14.01°N, 327 hPa, 0948:23 GMT (solid) and 89.65°E, 17.72°N, 326 hPa, 1028:57 GMT (dashed lines for temperature and dew point).
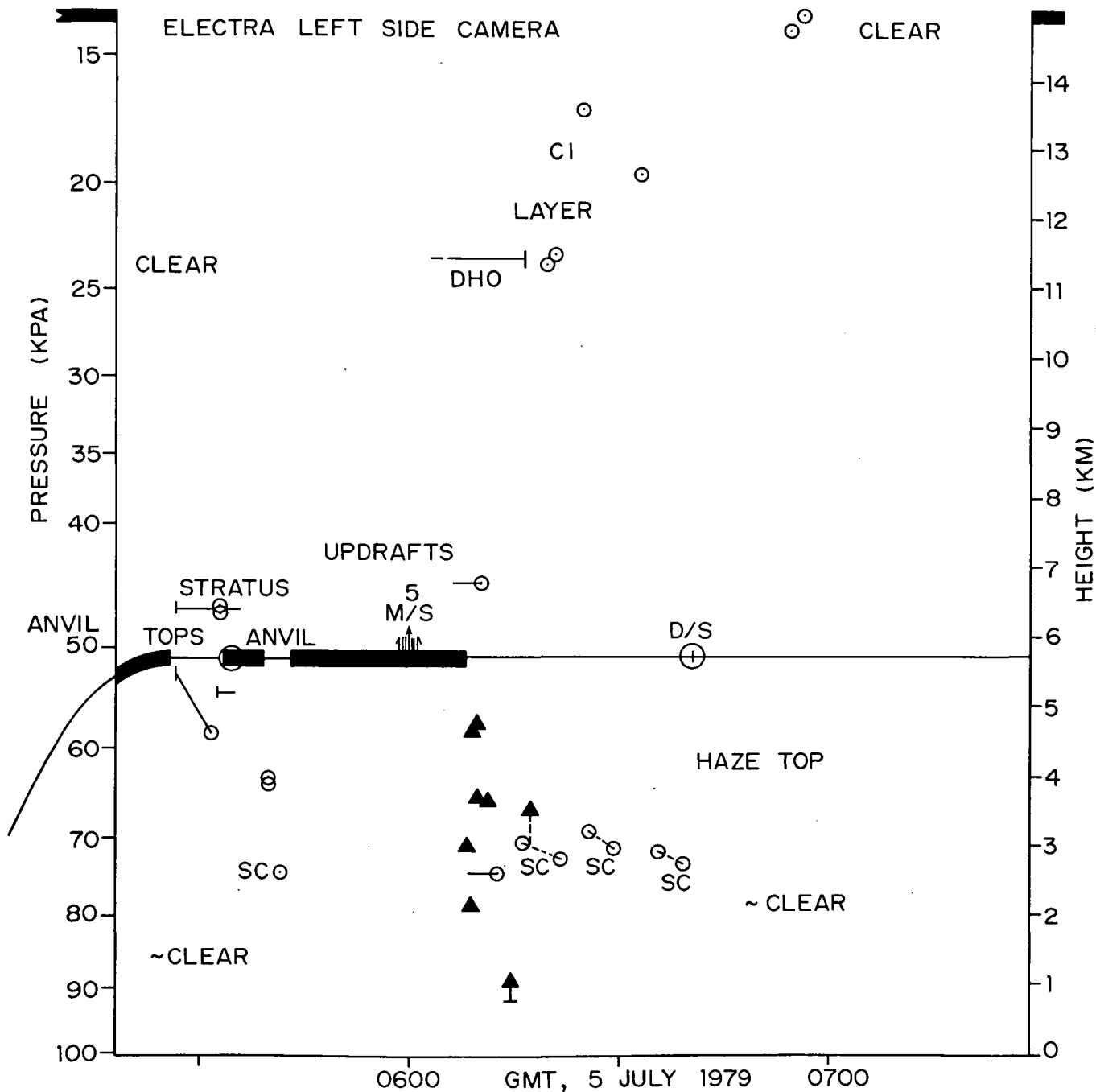
FIG. 32. Height-time section of measurements of clouds using
the left side camera of the Electra aircraft, between
     88.95°E, 20.96°N, 0518:02 GMT
and 86.26°E, 11.46°N, 0728:33 GMT. The line shows the trajectory
of the aircraft. Solid shading indicates passage in cloud.
Triangles indicate cumulus tops. Circles indicate measurements
on stratus. "SC" means stratocumulus. "DHO" means dense high
overcast. Lines either horizontal or inclined indicate stratus
layers. Circles along the track indicate locations of release
of dropwindsondes. The location is marked of a concentration
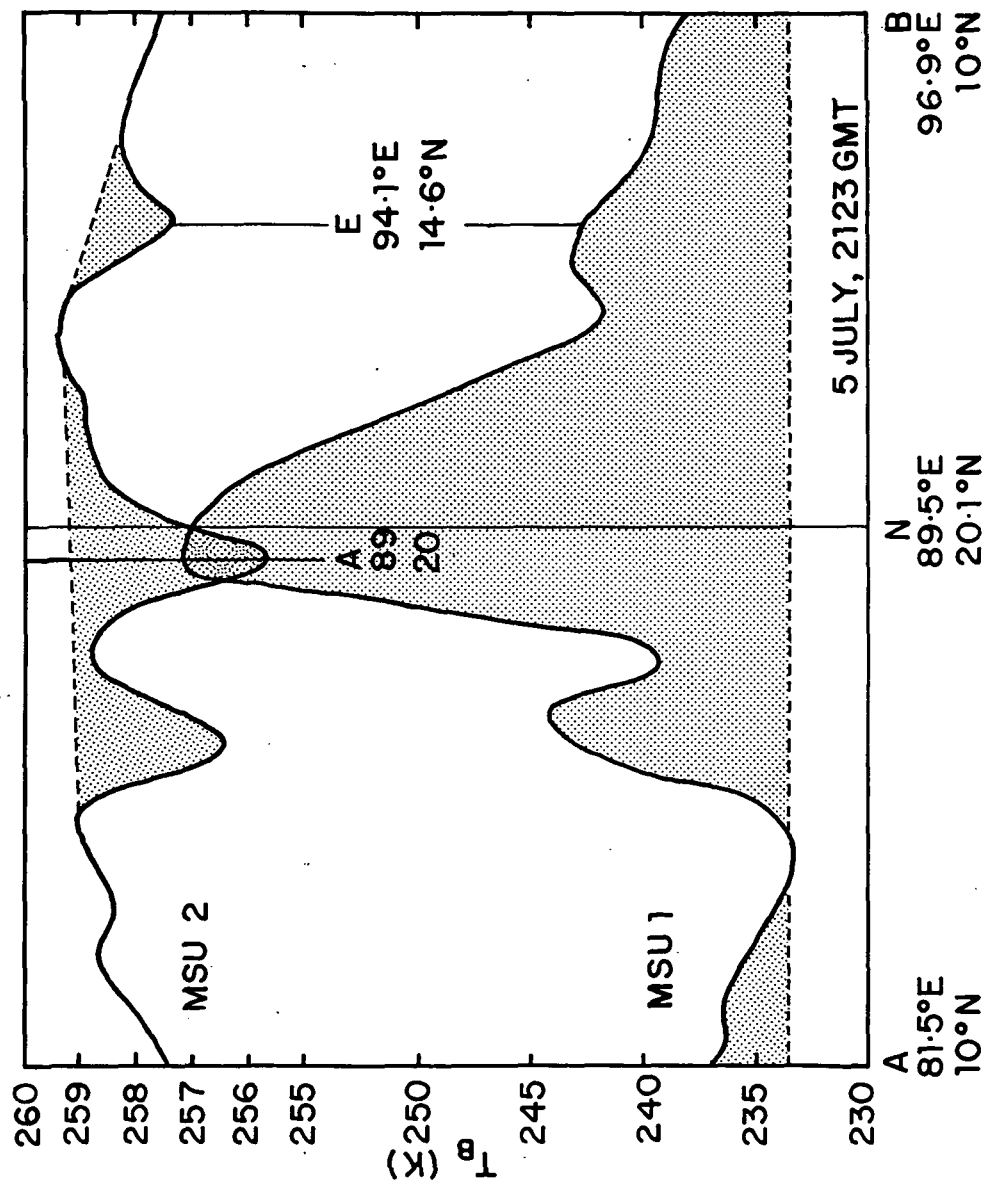of updraft cores (Table 6) reaching 5 m/s.
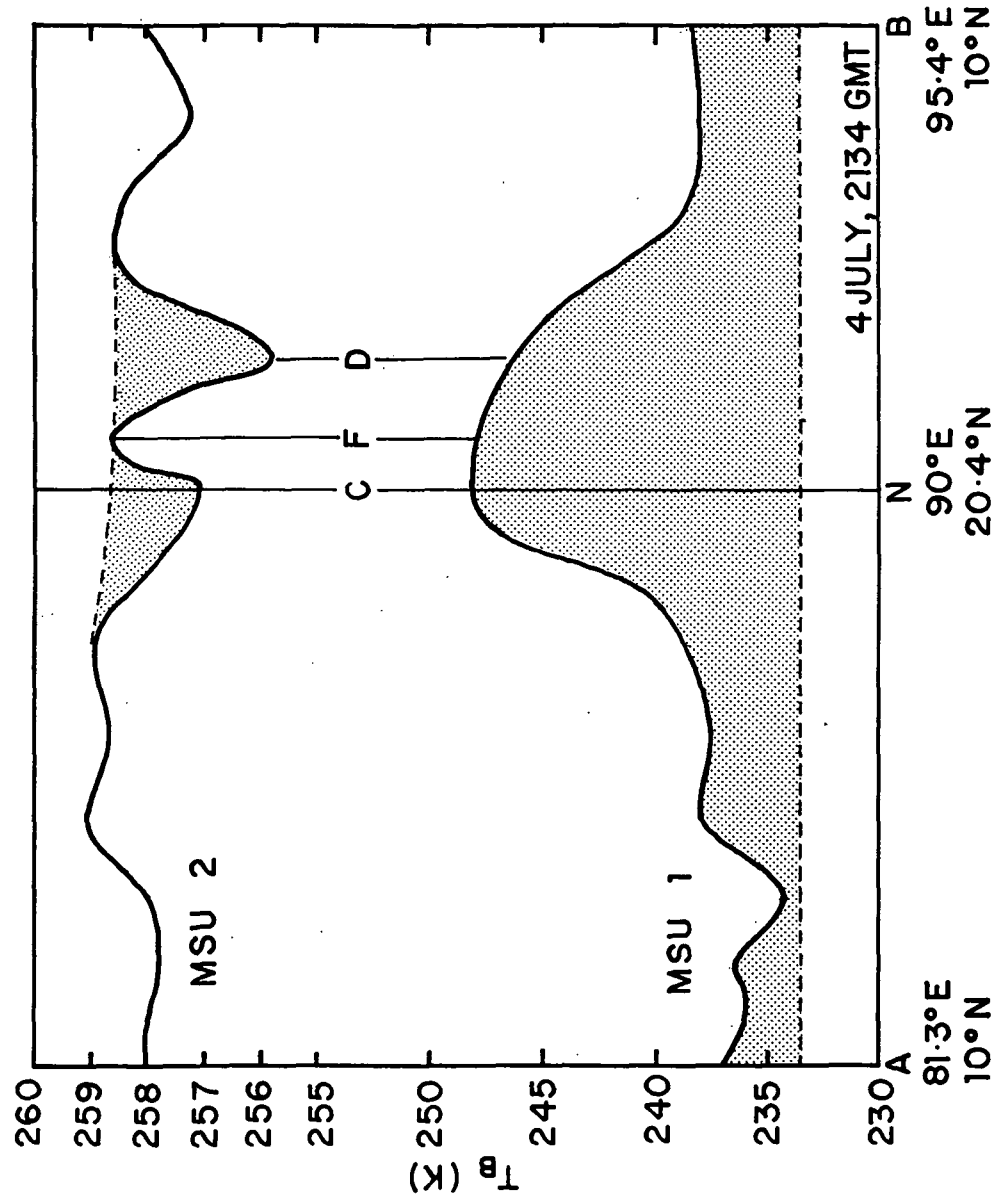
FIG. 33. 4 July, 2134 GMT. Brightness temperatures from MSU 1 (bottom) and MSU 2 (top) along thick-dashed line ANB drawn in Fig. 7 (right). Positions of points A, N and B are indicated. Dashed lines represent brightness temperatures which would probably pertain in the absence of hydrometeors. Anomalies at points C, F and D are examined in Table 10.
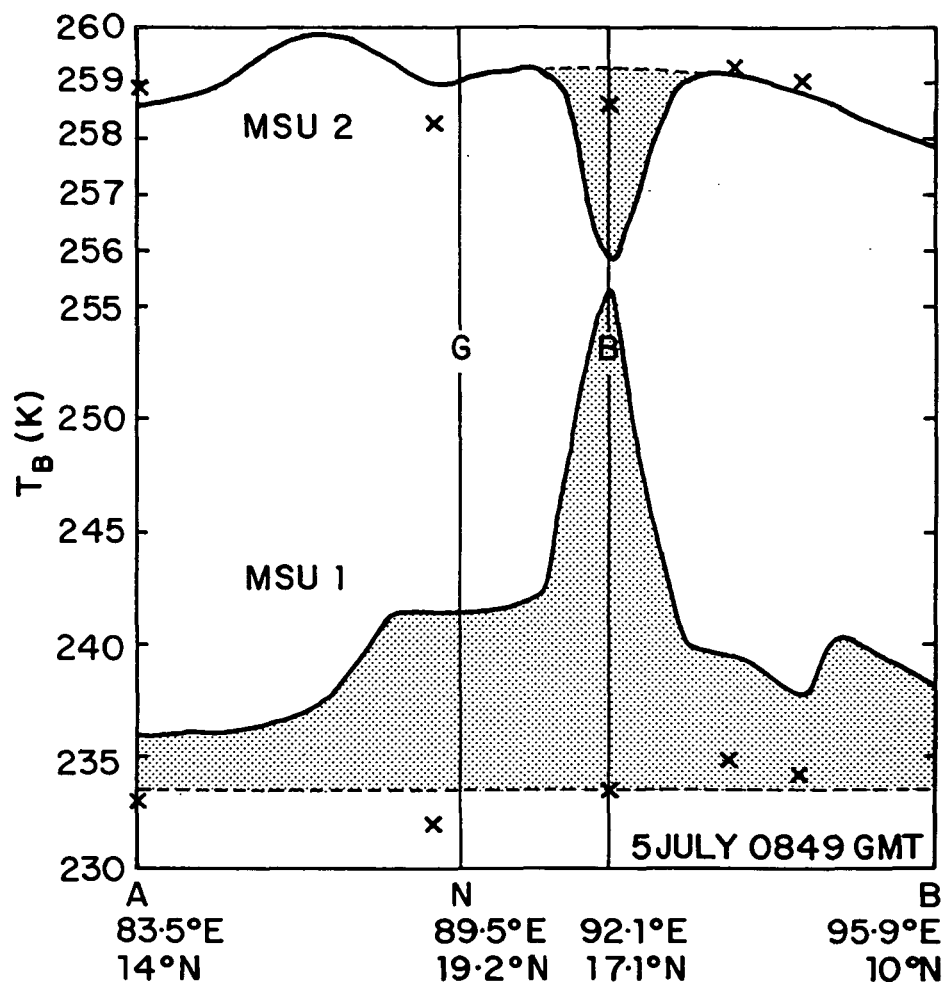
FIG. 34. 5 July, 0849 GMT. Brightness temperatures (T_B) from MSU 1 (bottom) and MSU 2 (top) along thick-dashed line ANB drawn in Fig. 8 (left). Positions of points are indicated. Crosses show calculated values of T_B in the absence of hydrometeors, from dropwindsondes near line ANB. Based on these, dashed lines represent brightness temperatures which would probably pertain in the absence of hydrometeors: Shading represents anomalies attributed to hydrometeors. Anomalies at points G and B are examined in Table 10.

FIG. 35. 5 July, 2123 GMT. Brightness temperatures from
MSU 1 (bottom) and MSU 2 (top) along thick-dashed line ANB
drawn in Fig. 8 (right). As in Figs. 33 and 34.
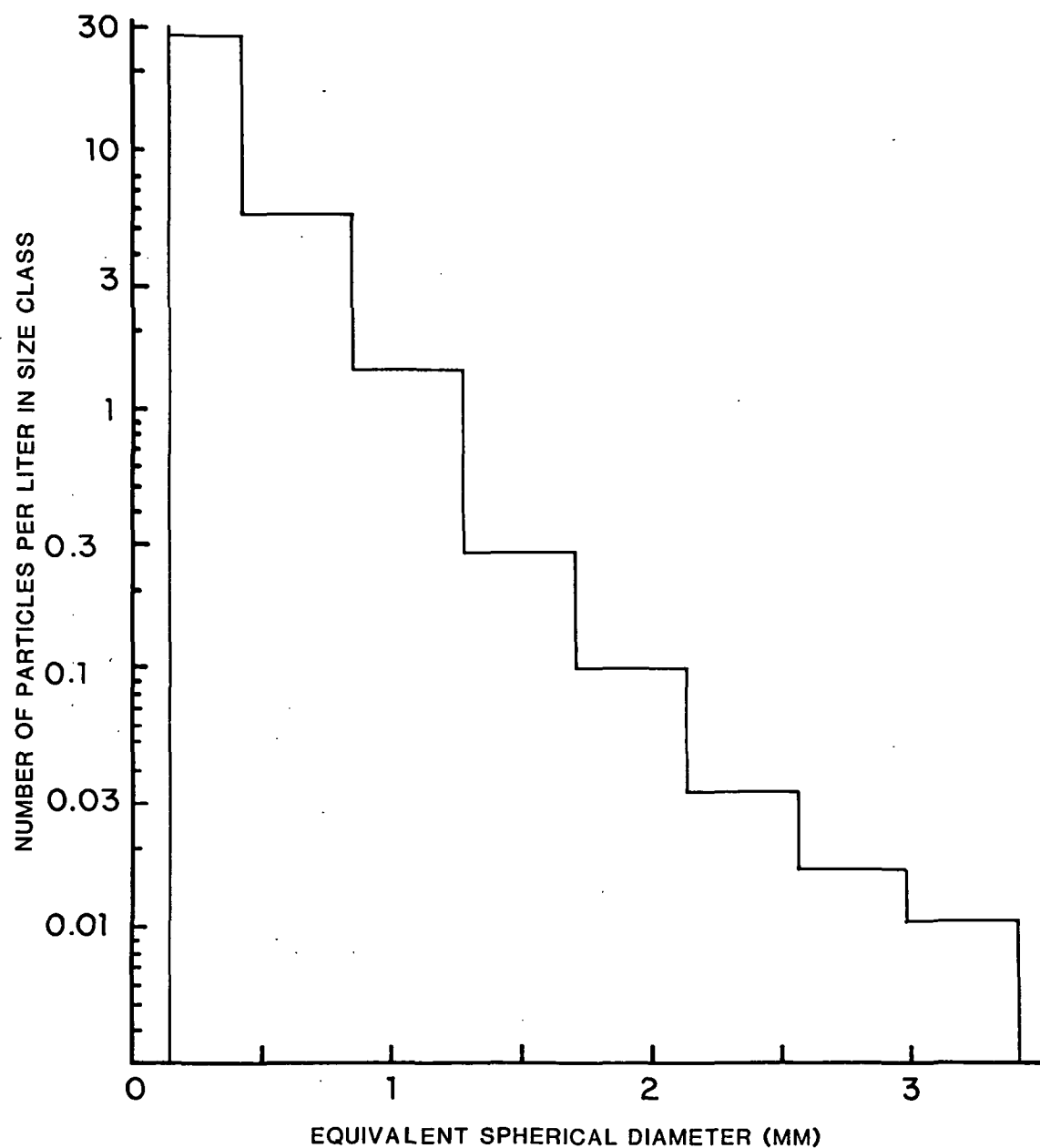
FIG. 36. Spectrum of sizes of ice particles measured from aircraft during SMONEX, communicated by John Gamache.
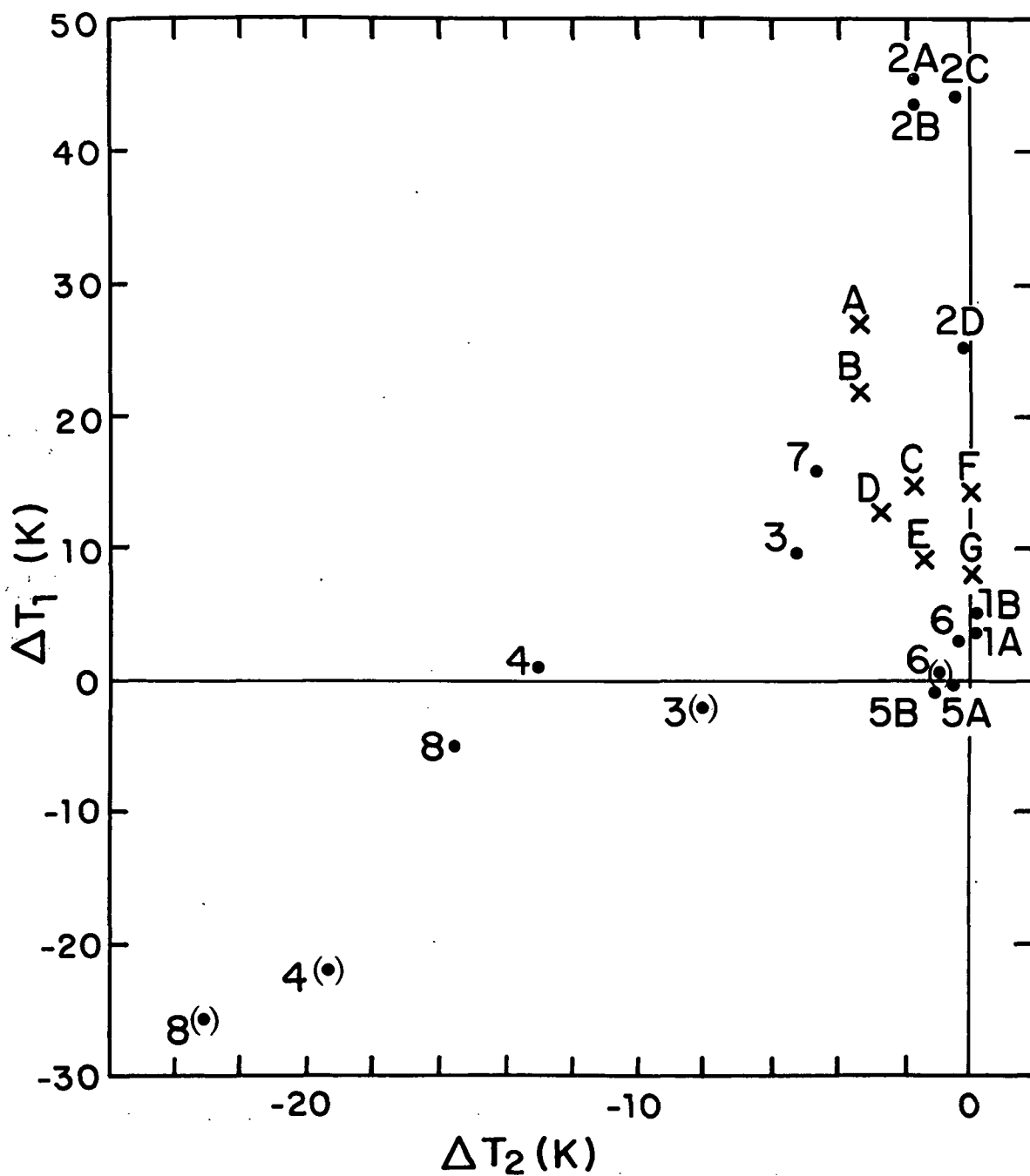
FIG. 37. Combinations of anomalies ΔT in MSU 1 and MSU 2 both measured (crosses, points A to G in Figs. 33-35), and calculated (dots, labeled with hydrometeor distribution type from Table 7).
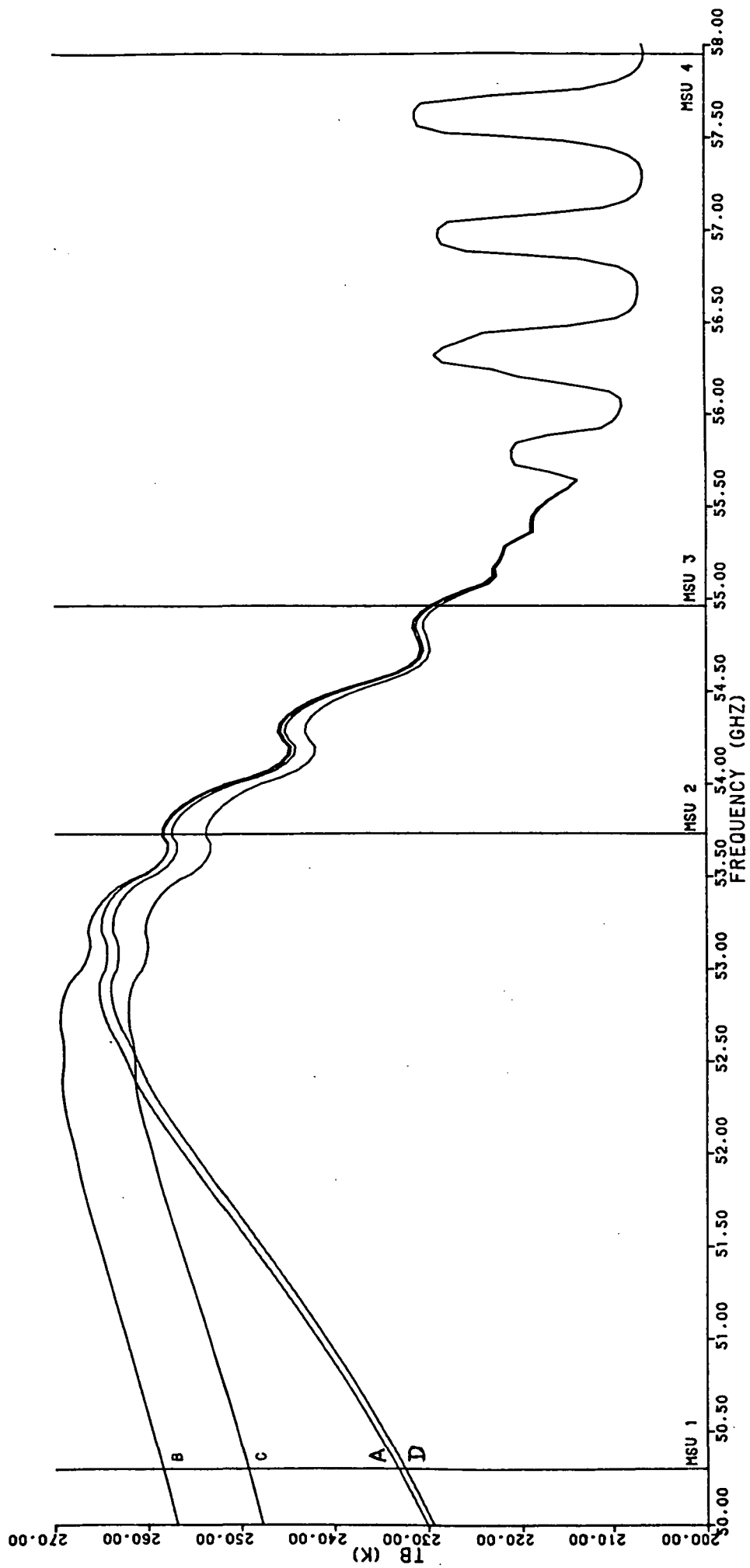
FIG. 38. Brightness temperature plotted against frequency in the range of MSU, for four different atmospheres:

A, 5 July, 0416 GMT, the background sounding for Table 7, without hydrometeors.

B, A + cumulus type 2d in Table 7.

C, A + 2d + anvil type 5b.

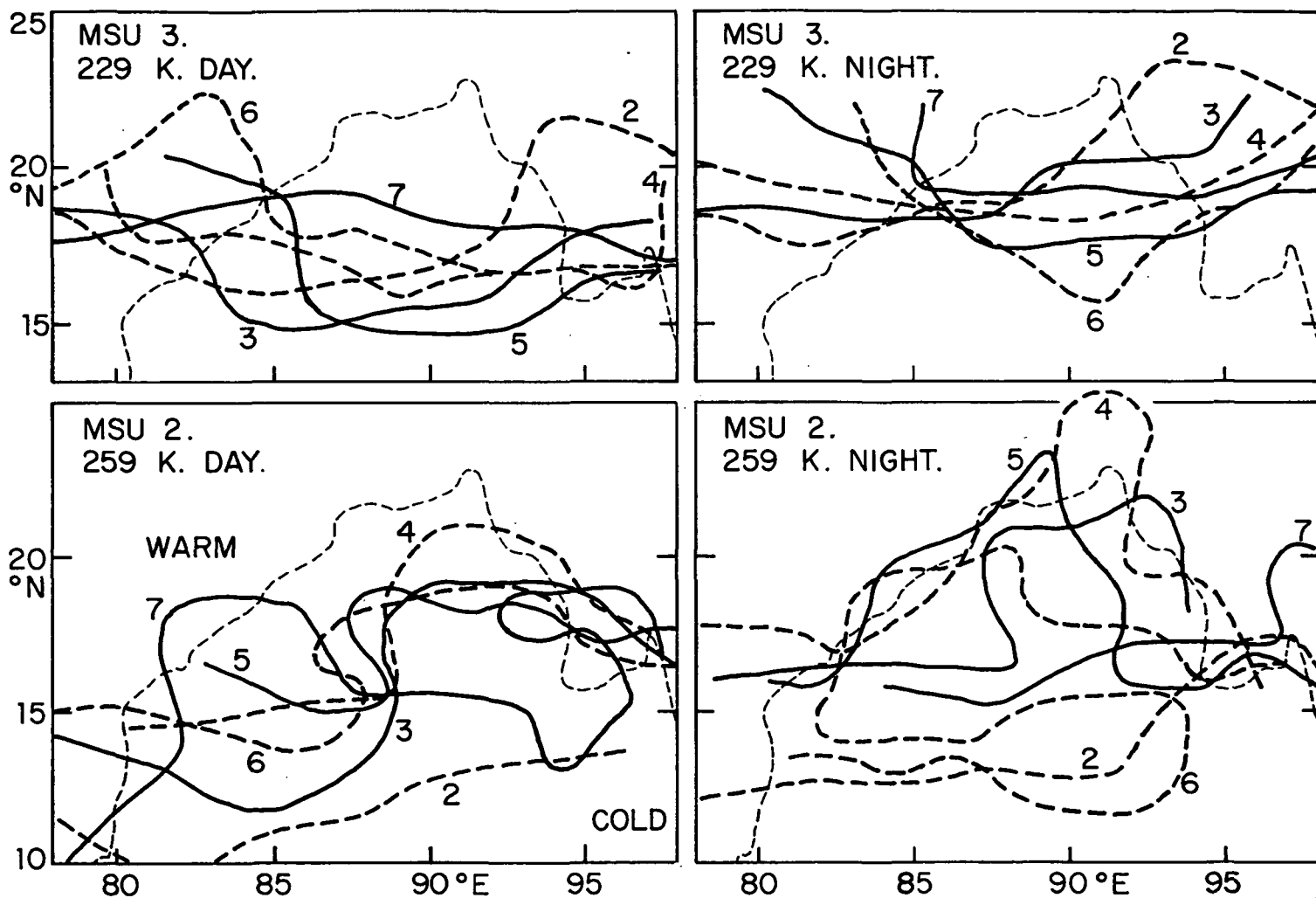D, A + 5b.

FIG. 39. Brightness temperature contours superimposed.
   2-7 July.   Top: MSU 1, 229 K.
                Bottom: MSU 2, 259 K
Left: From daytime orbits, at about 0900 GMT.
Right: From night-time orbits, at about 2130 GMT.
Alternate days are shown by solid and long-dashed lines.
The coast of the Bay is shown by a short-dashed line.
Use of crayons (a different color for each day)
                           brings out the patterns.
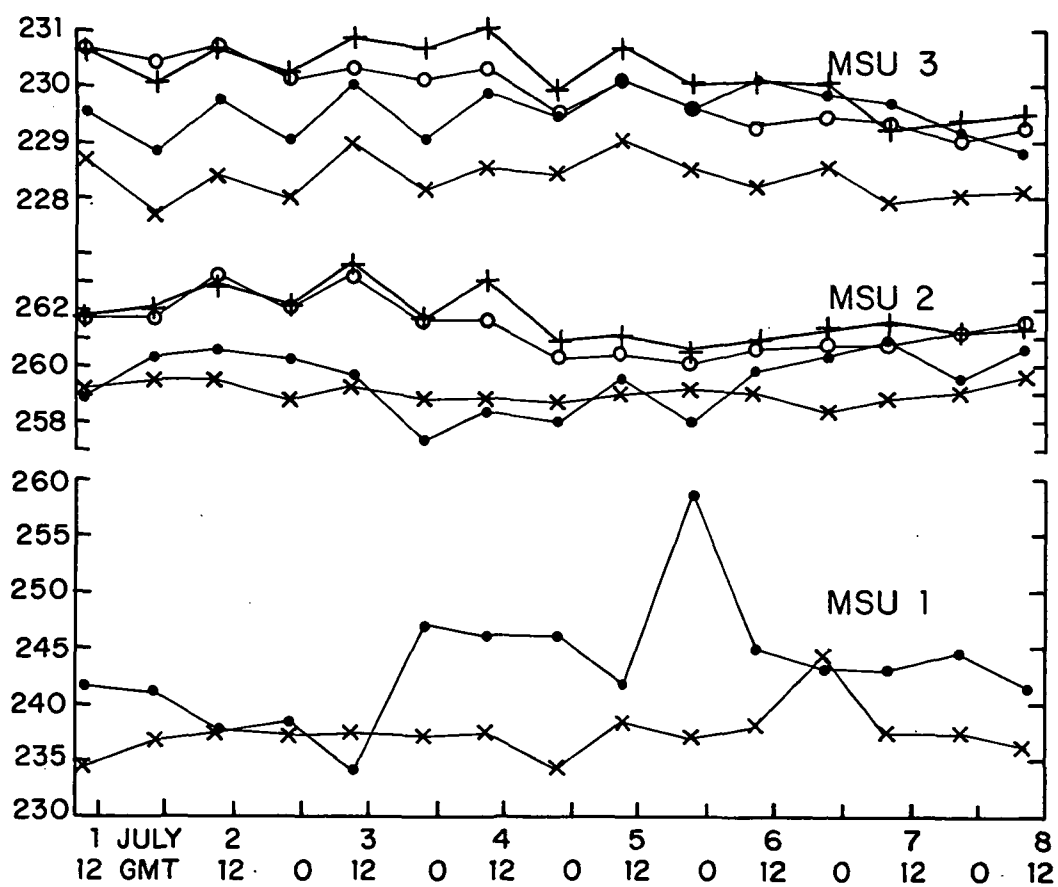
FIG. 40. Time series of brightness temperatures
from MSU 3, 2 and 1 as indicated,
  at 87°E, 24°N   (India)   +
       85°E, 22.5°N (India)   o
       90°E,   20°N (Head Bay)   .
and 87.5°E, 15°N (central Bay)   X